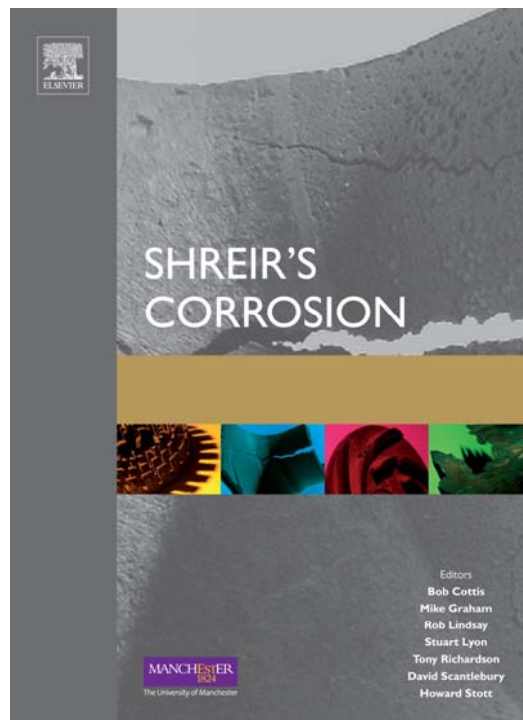


Provided for non-commercial research and educational use.
Not for reproduction, distribution or commercial use.

This article was originally published in *Shreir's Corrosion*, published by Elsevier. The attached copy is provided by Elsevier for the author's benefit and for the benefit of the author's institution. It may be used for non-commercial research and educational use, including (without limitation) use in instruction at your institution, distribution to specific colleagues who you know, and providing a copy to your institution's administrator.



All other uses, reproduction and distribution, including (without limitation) commercial reprints, selling or licensing of copies or access, or posting on open internet sites, personal or institution websites or repositories, are prohibited. For exception, permission may be sought for such use through Elsevier's permissions site at:

<http://www.elsevier.com/locate/permissionusematerial>

Anderko A 2010 Modeling of Aqueous Corrosion. In: Richardson J A et al. (eds.) *Shreir's Corrosion*, volume 2, pp. 1585-1629 Amsterdam: Elsevier.

2.38 Modeling of Aqueous Corrosion

A. Anderko

OLI Systems Inc., 108 American Road, Morris Plains, NJ 07950, USA

© 2010 Elsevier B.V. All rights reserved.

2.38.1	Introduction	1586
2.38.2	Thermodynamic Modeling of Aqueous Corrosion	1587
2.38.2.1	Computation of Standard-State Chemical Potentials	1588
2.38.2.2	Computation of Activity Coefficients	1588
2.38.2.3	Electrochemical Stability Diagrams	1591
2.38.2.3.1	Diagrams at elevated temperatures	1594
2.38.2.3.2	Effect of multiple active species	1594
2.38.2.3.3	Diagrams for nonideal solutions	1595
2.38.2.3.4	Diagrams for alloys	1596
2.38.2.3.5	Potential–concentration diagrams	1597
2.38.2.4	Chemical Equilibrium Computations	1597
2.38.2.5	Problems of Metastability	1599
2.38.3	Modeling the Kinetics of Aqueous Corrosion	1600
2.38.3.1	Kinetics of Charge-Transfer Reactions	1601
2.38.3.2	Modeling Adsorption Phenomena	1604
2.38.3.3	Partial Electrochemical Reactions	1605
2.38.3.3.1	Anodic reactions	1605
2.38.3.3.2	Cathodic reactions	1607
2.38.3.3.3	Temperature dependence	1609
2.38.3.4	Modeling Mass Transport Using Mass Transfer Coefficients	1609
2.38.3.4.1	Example of electrochemical modeling of general corrosion	1611
2.38.3.5	Detailed Modeling of Mass Transport	1611
2.38.3.5.1	Effect of the presence of porous media	1614
2.38.3.6	Active–Passive Transition and Dissolution in the Passive State	1614
2.38.3.7	Scaling Effects	1618
2.38.3.8	Modeling Threshold Conditions for Localized Corrosion	1620
2.38.3.8.1	Breakdown of passivity	1621
2.38.3.8.2	Repassivation potential and its use to predict localized corrosion	1622
2.38.3.9	Selected Practical Applications of Aqueous Corrosion Modeling	1624
2.38.4	Concluding Remarks	1626
References		1626

Abbreviations

CCT Critical crevice temperature
CR Corrosion rate
HKF Helgeson–Kirkham–Flowers equation of state
Me Metal
MSA Mean spherical approximation
NRTL Nonrandom two-liquid (equation)
Ox Oxidized form
Re Reduced form
SHE Standard hydrogen electrode

UNIFAC Universal functional activity coefficient (equation)

UNIQUAC Universal quasi-chemical (equation)

Symbols

a_i Activity of species i
A Surface area
 A_{ij} Surface interaction coefficient for species i and j
b Tafel coefficient using decimal logarithms

$c_{i,b}$ Bulk molar concentration of species i
 $c_{i,s}$ Surface molar concentration of species i
 C_p Heat capacity at constant pressure
 d Characteristic dimension
 D_i Diffusion coefficient of species i
 D_t Turbulent diffusion coefficient
 e^- Electron
 E Potential
 E_b Passivity breakdown potential
 E_{corr} Corrosion potential
 E_{crit} Critical potential for localized corrosion
 E_{rp} Repassivation potential
 E_0 Equilibrium potential
 f Friction factor
 f_i Fugacity of species i
 F Faraday constant
 G^{ex} Excess Gibbs energy
 i Current density
 i_a Anodic current density
 $i_{a,\text{ct}}$ Charge-transfer contribution to the anodic current density
 $i_{a,L}$ Limiting anodic current density
 i_c Cathodic current density
 $i_{c,\text{ct}}$ Charge-transfer contribution to the cathodic current density
 $i_{c,L}$ Limiting cathodic current density
 i_{corr} Corrosion current density
 i_p Passive current density
 i_{rp} Current density limit for measuring repassivation potential
 i_0 Exchange current density
 i^* Concentration-independent coefficient in expressions for exchange current density
 J_i Flux of species i
 k_{ads} Adsorption rate constant
 k_{des} Desorption rate constant
 k_i Reaction rate constant for reaction i
 $k_{m,i}$ Mass transfer coefficient for species i
 K Equilibrium constant
 K_{ads} Adsorption equilibrium constant
 K_{sp} Solubility product
 l_i Reaction rate for i th reaction
 m_i Molality of species i
 m_0 Standard molality of species i
 n_i Number of moles of species or electrons
 Nu Nusselt number
 Pr Prandtl number
 R Gas constant
 R_k Rate of production or depletion of species k
 Re Reynolds number
 S Supersaturation
 Sc Schmidt number

Sh Sherwood number
 t Time
 T Temperature
 u_i Mobility of species i
 v_i Rate of reaction i
 V Linear velocity
 z Direction perpendicular to the surface
 z_i Charge of species i
 α Thermal diffusivity
 α_i Electrochemical transfer coefficient for species i
 β Tafel coefficient using natural logarithms
 γ_i Activity coefficient of species i
 δ_i Nernst layer thickness for species i
 $\Delta G_{\text{ads},i}$ Gibbs energy of adsorption for species i
 ΔH^\ddagger Enthalpy of activation
 $\Delta\Phi$ Potential drop
 ϵ Dielectric permittivity
 η Dynamic viscosity
 θ_i Coverage fraction of species i
 θ_p Coverage fraction of passive layer
 λ Thermal conductivity
 μ_i Chemical potential of species i
 μ_i^0 Standard chemical potential
 $\bar{\mu}_i$ Electrochemical potential of species i
 ν Kinematic viscosity
 ν_i Stoichiometric coefficient of species i
 ρ Density
 Φ Electrical potential
 ξ_i Electrochemical transfer coefficient for reaction i
 ω Rotation rate
 ∇ Vector differential operator
 $\equiv X$ Surface species X

2.38.1 Introduction

Aqueous corrosion is an extremely complex physical phenomenon that depends on a multitude of factors including the metallurgy of the corroding metal, the chemistry of the corrosion-inducing aqueous phase, the presence of other – solid, gaseous, or nonaqueous liquid – phases, environmental constraints such as temperature and pressure, fluid flow characteristics, methods of fabrication, geometrical factors, and construction features. This inherent complexity makes the development of realistic physical models very challenging and, at the same time, provides a strong incentive for the development of practical models to understand the corrosion phenomena, and to assist in their mitigation. The need for tools for simulating aqueous corrosion has been recognized in various industries including oil and gas production and

transmission, oil refining, nuclear and fossil power generation, chemical processing, infrastructure maintenance, hazardous waste management, and so on. The past three decades have witnessed the development of increasingly sophisticated modeling tools, which has been made possible by the synergistic combination of improved understanding of corrosion mechanisms and rapid evolution of computational tools.

Corrosion modeling is an interdisciplinary undertaking that requires input from electrolyte thermodynamics, surface electrochemistry, fluid flow and mass transport modeling, and metallurgy. In this chapter, we put particular emphasis on corrosion chemistry by focusing on modeling both the bulk environment and the reactions at the corroding interface. The models that are reviewed in this chapter are intended to answer the following questions:

1. What are the aqueous and solid species that give rise to corrosion in a particular system? What are their thermophysical properties, and what phase behavior can be expected in the system? These questions can be answered by thermodynamic models.
2. What are the reactions that are responsible for corrosion at the interface? How are they influenced by the bulk solution chemistry and by flow conditions? How can passivity and formation of solid corrosion products be related to environmental conditions? How can the interfacial phenomena be related to observable corrosion rates? These questions belong to the realm of electrochemical kinetics and mass transport models.
3. What conditions need to be satisfied for the initiation and long-term occurrence of localized corrosion? This question can be answered by electrochemical models of localized corrosion.

These models can be further used as a foundation for larger-scale models for the spatial and temporal evolution of systems and engineering structures subject to localized and general corrosion. Also, they can be combined with probabilistic and expert system-type models of corrosion. Models of such kinds are, however, outside the scope of this review, and will be discussed in companion chapters.

2.38.2 Thermodynamic Modeling of Aqueous Corrosion

Historically, the first comprehensive approach to modeling aqueous corrosion was introduced by Pourbaix in the 1950s and 1960s on the basis of purely thermodynamic considerations.¹ Pourbaix¹ developed the E -pH stability diagrams, which indicate

which phases are stable on a two-dimensional plane as a function of the potential and pH. The potential and pH were originally selected because they play a key role as independent variables in electrochemical corrosion. Just as importantly, they made it possible to construct the stability diagrams in a semianalytical way, which was crucial before the advent of computer calculations. Over the past four decades, great progress has been achieved in the thermodynamics of electrolyte systems, in particular for concentrated, mixed-solvent, and high temperature systems. These advances made it possible to improve the accuracy of the stability diagrams and, at the same time, increased the flexibility of thermodynamic analysis so that it can go well beyond the E -pH plane.

The basic objective of the thermodynamics of corrosion is to predict the conditions at which a given metal may react with a given environment, leading to the formation of dissolved ions or solid reaction products. Thermodynamics can predict the properties of the system in equilibrium or, if equilibrium is not achieved, it can predict the direction in which the system will move towards an equilibrium state. Thermodynamics does not provide any information on how rapidly the system will approach equilibrium, and, therefore, it cannot give the rate of corrosion.

The general condition of thermodynamic equilibrium is the equality of the electrochemical potential, $\bar{\mu}_i$ in coexisting phases,² that is,

$$\bar{\mu}_i = \mu_i + z_i F \phi = \mu_i^0 + RT \ln a_i + z_i F \phi \quad [1]$$

where μ_i is the chemical potential of species i ; μ_i^0 , its standard chemical potential; a_i , the activity of the species; z_i , its charge; F , the Faraday constant; and ϕ is the electrical potential. The standard chemical potential is a function of the temperature and, secondarily, pressure. The activity depends on the temperature and solution composition and, to a lesser extent, on pressure. The activity is typically defined in terms of solution molality m_i ,

$$a_i = (m_i/m^0)\gamma_i \quad [2]$$

where m^0 is the standard molality unit (1 mol kg⁻¹ H₂O), and γ_i is the activity coefficient. It should be noted that the molality basis for species activity becomes inconvenient for concentrated solutions because molality diverges to infinity as the concentration increases to the pure solute limit. Therefore, the mole fraction basis is more generally applicable for calculating activities.³ Nevertheless, molality remains the most common concentration unit for aqueous systems and is used here for illustrative purposes.

Computation of μ_i^0 and γ_i is the central subject in electrolyte thermodynamics. Numerous methods, with various ranges of applicability, have been developed over the past several decades for their computation. Several comprehensive reviews of the available models are available (Zemaitis *et al.*,⁴ Renon,⁵ Pitzer,⁶ Rafal *et al.*,⁷ Loehe and Donohue,⁸ Anderko *et al.*³). In the next section, the current status of modeling μ_i^0 and γ_i is outlined as it applies to the thermodynamics of corrosion.

2.38.2.1 Computation of Standard-State Chemical Potentials

The computation of the standard chemical potential μ_i^0 requires the knowledge of thermochemical data including

1. Gibbs energy of formation of species i at reference conditions (298.15 K and 1 bar).
2. Entropy or, alternatively, enthalpy of formation at reference conditions.
3. Heat capacity and volume as a function of temperature and pressure.

For numerous species, these values are available in various compilations (Chase *et al.*,⁹ Barin and Platzki,¹⁰ Cox *et al.*,¹¹ Glushko *et al.*,¹² Gurvich *et al.*,¹³ Kelly,¹⁴ Robie *et al.*,¹⁵ Shock and Helgeson,¹⁶ Shock *et al.*,^{17,18} Stull *et al.*,¹⁹ Wagman *et al.*,²⁰ and others). In general, thermochemical data are most abundant at near-ambient conditions, and their availability becomes more limited at elevated temperatures.

In the case of individual solid species, the chemical potential can be computed directly from tabulated thermochemical properties according to the standard thermodynamics.² In the case of ions and aqueous neutral species, the thermochemical properties listed above are standard partial molar properties rather than the properties of pure components. The standard partial molar properties are defined at infinite dilution in water. The temperature and pressure dependence of the partial molar heat capacity and the volume of ions and neutral aqueous species are quite complex because they are manifestations of the solvation of species, which is influenced by electrostatic and structural factors. Therefore, the computation of these quantities requires a realistic physical model.

An early approach to calculating the chemical potential of aqueous species as a function of temperature is the entropy correspondence principle of Criss and Cobble.²¹ In this approach, heat capacities of various types of ions were correlated with the reference-state entropies of ions, thus making it

possible to predict the temperature dependence of the standard chemical potential.

A comprehensive methodology for calculating the standard chemical potential was developed by Helgeson *et al.* (Helgeson *et al.*,²² Tanger and Helgeson²³). This methodology is based on a semi-empirical treatment of ion solvation, and results in an equation of state for the temperature and pressure dependence of the standard molal heat capacities and volumes. Subsequently, the heat capacities and volumes are used to arrive at a comprehensive equation of state for standard molal Gibbs energy and, hence, the standard chemical potential. The method is referred to as the HKF (Helgeson–Kirkham–Flowers) equation of state. An important advantage of the HKF equation is the availability of its parameters for a large number of ionic and neutral species (Shock and Helgeson,¹⁶ Shock *et al.*,¹⁸ Sverjensky *et al.*²⁴). Also, correlations exist for the estimation of the parameters for species for which little experimental information is available. The HKF equation of state has been implemented both in publicly available codes (Johnson *et al.*²⁵) and in commercial programs. A different equation of state for standard-state properties has been developed on the basis of fluctuation solution theory (Sedlbauer *et al.*,²⁶ Sedlbauer and Majer²⁷). This equation offers improvement over HKF for nonionic solutes and in the near-critical region. However, the HKF remains as the most widely accepted model for ionic solutes.

2.38.2.2 Computation of Activity Coefficients

In real solutions, the activity coefficients of species deviate from unity because of a variety of ionic interaction phenomena, including long-range Coulombic interactions, specific ion–ion interactions, solvation phenomena, and short-range interactions between uncharged and charged species. Therefore, a practically-oriented activity coefficient model must represent a certain compromise between physical reality and computational expediency.

The treatment of solution chemistry is a particularly important feature of an electrolyte model. Here, the term ‘solution chemistry’ encompasses ionic dissociation, ion pair formation, hydrolysis of metal ions, formation of metal–ligand complexes, acid–base reactions, and so on. The available electrolyte models can be grouped in three classes:

1. models that treat electrolytes on an undissociated basis,
2. models that assume complete dissociation of all electrolytes into constituent ions, and

- speciation-based models, which explicitly treat the solution chemistry.

The models that treat electrolytes as undissociated components are analogous to nonelectrolyte mixture models. They are particularly suitable for supercritical and high temperature systems, in which ion pairs predominate. Although this approach may also be used for phase equilibrium computations at moderate conditions (e.g., Kolker *et al.*²⁸), it is not suitable for corrosion modeling because it ignores the existence of ions. The models that assume complete dissociation are the largest class of models for electrolytes at typical conditions. Compared with the models that treat electrolytes as undissociated or completely dissociated, the speciation-based models are more computationally demanding because of the need to solve multiple reactions and phase equilibria. Another fundamental difficulty associated with the use of speciation models lies in the need to define and characterize the species that are likely to exist in the system. In many cases, individual species can be clearly defined and experimentally verified in relatively dilute solutions. At high concentrations, the chemical identity of individual species (e.g., ion pairs or complexes) becomes ambiguous because a given ion has multiple neighbors of opposite sign, and, thus, many species lose their distinct chemical character. Therefore, the application of speciation models to concentrated solutions requires a careful analysis to separate the chemical effects from physical nonideality effects.

It should be noted that, as long as only phase equilibrium computations are of interest, comparable results could be obtained with models that belong to various classes. For example, the overall activity coefficients and vapor–liquid equilibria of many transition metal halide solutions, which show appreciable complexation, can be reasonably reproduced using Pitzer's²⁹ ion-interaction approach without taking speciation into account. However, it is important to include speciation effects for modeling the thermodynamics of aqueous corrosion. This is due to the fact that the presence of individual hydrolyzed forms, aqueous complexes, and so on is often crucial for the dissolution of metals and metal oxides. It should be noted that activity coefficients of individual species are different in fully speciated models than in models that treat speciation in a simplified way. Therefore, it is important to use activity coefficients that have been determined in a fully consistent way, that is, by assuming the appropriate chemical species in the solution.

The theory of liquid-phase nonideality is well-established for dilute solutions. A limiting law for activity

coefficients was developed by Debye and Hückel³⁰ by considering the long-range electrostatic interactions of ions in a dielectric continuum. The Debye–Hückel theory predicts the activity coefficients as a function of the ionic charge and dielectric constant and density of the solvent. It reflects only electrostatic effects and, therefore, excludes all specific ionic interactions. Therefore, its range of applicability is limited to ~ 0.01 M for typical systems. Several modifications of the Debye–Hückel theory have been proposed over the past several decades. The most successful modification was developed by Pitzer²⁹ who considered hard-core effects on electrostatic interactions. A more comprehensive treatment of the long-range electrostatic interactions can be obtained from the mean-spherical approximation (MSA) theory,^{31,32} which provides a semianalytical solution for ions of different sizes in a dielectric continuum. The MSA theory results in a better prediction of the long-range contribution to activity coefficients at somewhat higher electrolyte concentrations.

The long-range electrostatic term provides a baseline for constructing models that are valid for electrolytes at concentrations that are important in practice. In most practically-oriented electrolyte models, the solution nonideality is defined by the excess Gibbs energy G^{ex} . The excess Gibbs energy is calculated as a sum of the long-range term and one or more terms that represent ion–ion, ion–molecule, and molecule–molecule interactions:

$$G^{\text{ex}} = G_{\text{long-range}}^{\text{ex}} + G_{\text{specific}}^{\text{ex}} + \dots \quad [3]$$

where the long-range contribution is usually calculated either from the Debye–Hückel or the MSA theory, and the specific interaction term(s) represent(s) all other interactions in an electrolyte solution. Subsequently, the activity coefficients are calculated according to standard thermodynamics² as

$$\ln \gamma_i = \frac{1}{RT} \left(\frac{\partial G^{\text{ex}}}{\partial n_i} \right)_{T,P,n_j \neq i} \quad [4]$$

Table 1 lists a number of activity coefficient models that have been proposed in the literature, and shows the nature of the specific interaction terms that have been adopted. In general, these models can be subdivided into two classes:

- models for aqueous systems; in special cases, such models can also be used for other solvents as long as the system contains a single solvent;
- mixed-solvent electrolyte models, which allow multiple solvents as well as multiple solutes.

The aqueous electrolyte models incorporate various ion interaction terms, which are usually defined

Table 1 Summary of representative models for calculating activity coefficients in electrolyte systems

Reference	Terms	Features
<i>Aqueous (or single-solvent) electrolyte models</i>		
Debye and Hückel ³⁰	Long-range	Limiting law valid for very dilute solutions
Guggenheim ^{33,34}	Long-range + ion interaction	Simple ion interaction term to extend the Debye–Hückel limiting law; applicable to fairly dilute solutions
Helgeson ³⁵	Long-range + ion interaction	Ion interaction term to extend the limiting law; applicable to fairly dilute solutions
Pitzer ²⁹	Long-range + ion interaction	Ionic strength-dependent virial coefficient-type ion interaction term; revised Debye–Hückel limiting law; applicable to moderately concentrated solutions (~6 m)
Bromley ³⁶	Long range + ion interaction	Ionic strength dependent ion interaction term; applicable to moderately concentrated solutions (~6 m)
Zemaitis ³⁷	Long-range + ion interaction	Modification of the model of Bromley ³⁶ to increase applicability range with respect to ionic strength
Meissner ³⁸	One-parameter correlation as a function of ionic strength	Generalized correlation to calculate activities based on a limited amount of experimental information
Pitzer and Simonson, ³⁹ Clegg and Pitzer ⁴⁰	Long-range + ion interaction	Mole fraction-based expansion used for the ion interaction term; applicable to concentrated systems up to the fused salt limit
<i>Mixed-solvent electrolyte models</i>		
Chen <i>et al.</i> ⁴¹	Long-range + short-range	Local-composition (NRTL) short-range term
Liu and Watanasiri ⁴²	Long-range + short-range + electrostatic solvation (Born) + ion interaction	Modification of the model of Chen <i>et al.</i> ⁴¹ using a Guggenheim-type ion interaction term for systems with two liquid phases
Abovsky <i>et al.</i> ⁴³	Long-range + short-range	Modification of the model of Chen <i>et al.</i> ⁴¹ using concentration-dependent NRTL parameters to extend applicability range with respect to electrolyte concentration
Chen <i>et al.</i> ⁴⁴	Long-range + short-range + ion hydration	Modification of the model of Chen <i>et al.</i> ⁴¹ using an analytical ion hydration term to extend applicability with respect to electrolyte concentration
Chen and Song ⁴⁵	Long-range + short-range + electrostatic solvation (Born)	Modification of the model of Chen <i>et al.</i> ⁴¹ by introducing segment interactions for organic molecules
Sander <i>et al.</i> ⁴⁶	Long-range + short-range	Local composition model (UNIQUAC) with concentration-dependent parameters used for short-range term
Macedo <i>et al.</i> ⁴⁷	Long-range + short-range	Local composition model (UNIQUAC) with concentration-dependent parameters used for short-range term
Kikic <i>et al.</i> ⁴⁸	Long-range + short range	Local composition group contribution model (UNIFAC) used for short-range term
Dahl and Macedo ⁴⁹	Short-range	Undissociated basis; no long-range contribution; group contribution model (UNIFAC) used for short-range term
Iliuta <i>et al.</i> ⁵⁰	Long-range + short-range	Local composition (UNIQUAC) model used for short-range term
Wu and Lee ³¹	Extended long-range (MSA)	Mean-spherical approximation (MSA) theory used for the long-range term
Li <i>et al.</i> ⁵¹	Long range + ion interaction + short range	Virial-type form used for the ion interaction term; local composition used for short-range term
Yan <i>et al.</i> ⁵²	Long-range + ion interaction + short range	Group contribution models used for both the ion interaction term and short-range term (UNIFAC)
Zerres and Prausnitz ⁵³	Long-range + short range + ion solvation	Van Laar model used for short-range term; stepwise ion solvation model
Kolker <i>et al.</i> ²⁸	Short-range	Undissociated basis; no long-range contribution
Wang <i>et al.</i> ^{54,55}	Long range + ion interaction + short range	Ionic strength-dependent virial expansion-type ion interaction term; local composition (UNIQUAC) short-range term; detailed treatment of solution chemistry
Papaiconomou <i>et al.</i> ³²	Extended long-range (MSA) + short-range	MSA theory used for the long-range term; local composition model (NRTL) used for the short-range term

in the form of virial-type expansions in terms of molality or mole fractions (see **Table 1**). Among these models, the Pitzer²⁹ molality-based model has found wide acceptance. Parameters of the Pitzer²⁹ model are available in the open literature for a large number of systems.⁶

The mixed-solvent electrolyte models are designed to handle a wider variety of chemistries. They invariably use the mole fraction and concentration scales. A common approach in the construction of mixed-solvent models is to use local-composition models for representing short-range interactions. The well-known local-composition models include NRTL, UNIQUAC, and its group-contribution version, UNIFAC (see Prausnitz *et al.*⁵⁶ and Malanowski and Anderko⁵⁷ for a review of these models). The local composition models are commonly used for nonelectrolyte mixtures and, therefore, it is natural to use them for short-range interactions in electrolyte systems. The combination of the long-range and local-composition terms is typically sufficient for representing the properties of moderately concentrated electrolytes in any combination of solvents. For systems that may reach very high concentrations with respect to electrolyte components (e.g., up to the fused salt limit), more complex approaches have been developed. One viable approach is to explicitly account for hydration and solvation equilibria in addition to using the long-range and short-range local composition terms (Zerres and Prausnitz,⁵³ Chen *et al.*⁴⁴). A particularly effective approach is based on combining virial-type ion interaction terms with local composition models (Li *et al.*,⁵¹ Yan *et al.*,⁵² Wang *et al.*^{54,55}). In such combined models, the local-composition term reflects the nonelectrolyte-like short-range interactions, whereas the virial-type ion interaction term represents primarily the specific ion-ion interactions that are not accounted for by the long-range contribution. These and other approaches are summarized in **Table 1**. Among the models summarized in **Table 1**, the models of Pitzer,²⁹ Zemaitis,³⁷ Chen *et al.*⁴¹ (including their later modifications),^{44,45} and Wang *et al.*^{54,55} have been implemented in publicly available or commercial simulation programs.

2.38.2.3 Electrochemical Stability Diagrams

The E -pH diagrams, commonly referred to as the Pourbaix¹ diagrams, are historically the first, and remain the most important class of electrochemical stability diagrams. They were originally constructed for ideal solutions (i.e., on the assumption that $\gamma_i = 1$),

which was the only viable approach at the time when they were introduced.¹ The essence of the procedure for generating the Pourbaix diagrams is analyzing all possible reactions between all – aqueous or solid – species that may exist in the system. The simultaneous analysis of the reactions makes it possible to determine the ranges of potential and pH at which a given species is stable. The reactions can be conveniently subdivided into two classes, that is, chemical and electrochemical reactions. The chemical reactions can be written without electrons, that is

$$\sum v_i M_i = 0 \quad [5]$$

Then, the equilibrium condition for the reaction is given in terms of the chemical potentials of individual species by

$$\sum v_i \mu_i = 0 \quad [6]$$

According to eqn [1], eqn [6] can be further rewritten in terms of species activities as

$$\sum v_i \ln a_i = -\frac{\sum v_i \mu_i^0}{RT} = \ln K \quad [7]$$

where the right-hand side of eqn [7] is defined as the equilibrium constant because it does not depend on species concentrations.

In contrast to the chemical reactions, the electrochemical reactions involve electrons, e^- , as well as chemical substances M_b that is

$$\sum v_i M_i + n e^- = 0 \quad [8]$$

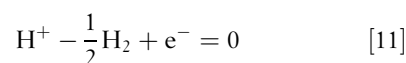
The equilibrium state of an electrochemical reaction is associated with a certain equilibrium potential. Since electrode potential cannot be measured on an absolute basis, it is necessary to choose an arbitrary scale against which the potentials can be calculated. If a reference electrode is selected, the equilibrium state of the reaction that takes place on the reference electrode is given by an equation analogous to eqn [8], that is

$$\sum v_{i,\text{ref}} M_{i,\text{ref}} + n e^- = 0 \quad [9]$$

Then, the equilibrium potential E_0 of eqn [8] is given with respect to the reference electrode as

$$E_0 - E_{0,\text{ref}} = \frac{\sum v_i \mu_i - \sum v_{i,\text{ref}} \mu_{i,\text{ref}}}{nF} \quad [10]$$

According to a generally used convention, the standard hydrogen electrode (SHE) (i.e., $H^+(a_{H^+} = 1)/H_2(f_{H_2} = 1)$) is used as a reference. The corresponding reaction that takes place on the SHE is given by



Then, eqn [10] becomes

$$E_0 - E_{0,\text{ref}} = \frac{\sum v_i \mu_i - n \left(\mu_{\text{H}^+}^0 - \frac{1}{2} \mu_{\text{H}_2}^0 \right)}{nF} \quad [12]$$

In eqn [12], the standard chemical potentials $\mu_{\text{H}^+}^0$ and $\mu_{\text{H}_2}^0$ as well as the reference potential $E_{0,\text{ref}}$ are equal to zero at $T=298.15$ K. For practical calculations at temperatures other than 298.15 K, two conventions can be used for the reference electrode. According to a universal convention established by the International Union of Pure and Applied Chemistry (the 'Stockholm convention'), the potential of SHE is arbitrarily defined as zero at all temperatures (i.e., $E_{0,\text{ref}} = 0$). When this convention is employed, eqn [12] is used as a working equation with $E_{0,\text{ref}} = 0$. In an alternate convention, the SHE reference potential is equal to zero only at room temperature, and its value at other temperatures depends on the actual, temperature-dependent values of $\mu_{\text{H}^+}^0$ and $\mu_{\text{H}_2}^0$. In this case, it is straightforward to show (see Chen and Aral,⁵⁸ Chen *et al.*,⁵⁹) that eqn [12] becomes

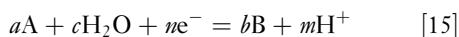
$$E_0 = \frac{\sum v_i \mu_i}{nF} \quad [13]$$

at all temperatures. Equation [13] can be further rewritten in terms of activities as

$$E_0 = \frac{\sum v_i \mu_i^0}{nF} + \frac{RT}{nF} \sum v_i \ln a_i = E_0^0 + \frac{RT}{nF} \sum v_i \ln a_i \quad [14]$$

where E_0^0 is the standard equilibrium potential, which is calculated from the values of the standard chemical potentials μ_i^0 .

For a brief outline of the essence of the Pourbaix diagrams, let us consider a generic reaction in which two species, A and B, undergo a transformation. The only other species that participate in the reaction are hydrogen ions and water, that is:



If eqn [15] is a chemical reaction (i.e., if $n=0$), then its equilibrium condition (eqn [7]) can be rewritten as

$$m\text{pH} = \log \left(\frac{a_B^a}{a_A^a} \right) - \log K - \log a_{\text{H}_2\text{O}}^c \quad [16]$$

where $\text{pH} = -\log a_{\text{H}^+}$, and decimal rather than natural logarithms is used. For dilute solutions, it is appropriate to assume that $a_{\text{H}_2\text{O}} = 1$, and the last term on the right-hand side of eqn [16] vanishes. If we assume that the components A and B are aqueous dissolved species and their activities are equal, eqn [16] defines the boundary between the predominance areas of species A and B. If one of the species (A or B) is a pure

solid and the other is an aqueous species, the activity of the solid is equal to one and the activity of the aqueous species can be set equal to a certain predetermined, typically small, value (e.g., 10^{-6}). Then, eqn [16] represents the boundary between a solid and an aqueous species at a fixed value of the dissolved species activity. Similarly, for a boundary between two pure solid phases, the activities of the species A and B are equal to one. Such a boundary is represented by a vertical line in a potential–pH space, and its location depends on the equilibrium constant according to eqn [16].

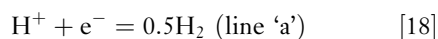
If eqn [15] represents an electrochemical reaction (i.e., $n \neq 0$), the equilibrium condition (eqn [14]) becomes

$$E_0 = E_0^0 + \frac{RT}{nF} \ln \frac{a_A^a}{a_B^b} + \frac{RT}{nF} \ln a_{\text{H}_2\text{O}} + \frac{RT \ln 10}{F} \frac{m}{n} \text{pH} \quad [17]$$

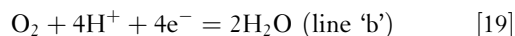
As with the chemical reactions, the term that involves the activity of water vanishes for dilute solutions, and the ratio of the activities of species A and B can be fixed to represent the boundary between the predominance areas of two species. Under such assumptions, the plot of E versus pH is a straight line with a slope determined by the stoichiometric coefficients m and n .

Thus, for each species, boundaries can be established using eqns [16] and [17]. As long as the simplifying assumptions described above are met, the boundaries can be calculated analytically. By considering all possible boundaries, stability regions can be determined using an algorithm described by Pourbaix.¹ Sample E –pH diagrams are shown for iron in Figure 1.

One of the main reasons for the usefulness of stability diagrams is the fact that they can illustrate the interplay of various partial processes of oxidation and reduction. The classical E –pH diagrams contain two dashed lines, labeled as 'a' and 'b,' which are superimposed on the diagram of a given metal (see Figure 1). The dashed line 'a' represents the conditions of equilibrium between water (or hydrogen ions) and elemental hydrogen at unit hydrogen fugacity, that is



The 'b' line describes the equilibrium between water and oxygen, also at unit fugacity,



Accordingly, water will be reduced to form hydrogen at potentials below line 'a,' and will be oxidized to form oxygen at potentials above line 'b.' The location

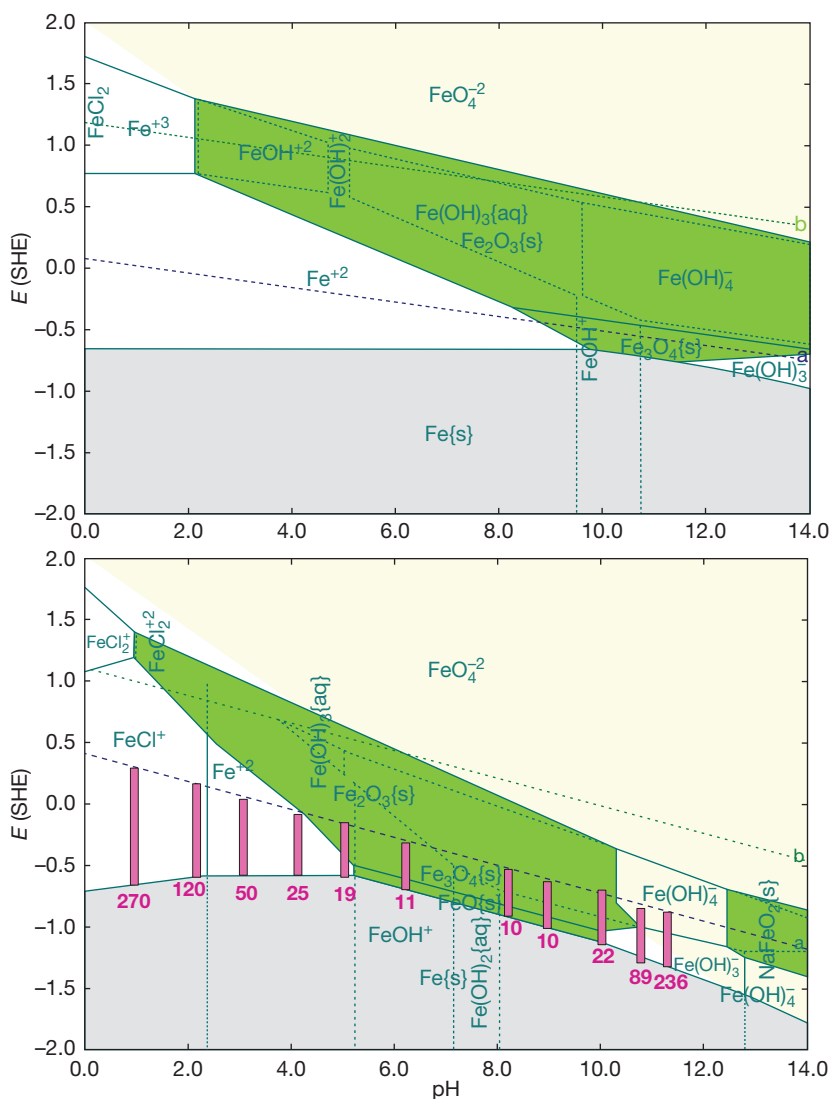


Figure 1 E -pH (Pourbaix) diagrams for iron at 25 °C (upper diagram) and 300 °C (lower diagram). At 300 °C, the conditions of the experiments of Partridge and Hall⁶⁰ are superimposed on the diagram. The vertical bars show the range between the equilibrium potentials for the reduction of H^+ and oxidation of Fe, thus bracketing the mixed potential in the experiments. The numbers under the bars denote the experimentally determined relative attack. The diagrams have been generated using the Corrosion Analyzer software⁶¹ using the algorithm of Anderko *et al.*⁶²

of the 'a' and 'b' lines on the diagram indicates whether a given redox couple is thermodynamically possible. For example, in the region between the line 'a' and the upper edge of the stability region of $Fe(s)$ in **Figure 1**, the anodic reaction of iron oxidation can be coupled with the cathodic reaction of water or hydrogen ion reduction. In such a case, the measurable open-circuit potential of the corrosion process will establish itself between the line 'a' and the equilibrium potential for the oxidation of iron (i.e., the upper edge of the $Fe(s)$ region). If the potential lies above

line 'a,' then water reduction is no longer a viable cathodic process, and the oxidation of iron must be coupled with another reduction process. In the presence of oxygen, reaction eqn [19] can provide such a reaction process. In such a case, the open-circuit (corrosion) potential will establish itself at a higher value for which the upper limit will be defined by line 'b.'

Pourbaix¹ subdivided various regions of the E -pH diagrams into three categories, that is, immunity, corrosion, and passivation. The immunity region

encompasses the stability field of elemental metals. The corrosion region corresponds to the stability of dissolved, either ionic or neutral species. Finally, passivation denotes the region in which solid oxides or hydroxides are stable. In **Figure 1**, the immunity and passivation regions are shaded, whereas the corrosion region is not. It should be noted that this classification does not necessarily reflect the actual corrosion behavior of a metal. Only immunity has a strict significance in terms of thermodynamics because in this region the metal cannot corrode regardless of the time of exposure. The stability of dissolved species in the 'corrosion' region does not necessarily mean that the metal rapidly corrodes in this area. In reality, the rate of corrosion in this region may vary markedly because of kinetic reasons. Passivation is also an intrinsically kinetic phenomenon because the protectiveness of a solid layer on the surface of a metal is determined not by its low solubility alone. The presence of a sparingly soluble solid is typically a necessary, but not sufficient condition for passivity.

Although the E -pH diagrams indicate only the thermodynamic tendency for the stability of various metals, ions, and solid compounds, they may still provide useful qualitative clues as to the expected trends in corrosion rates. This is illustrated in the lower diagram of **Figure 1**. In this diagram, the vertical bars denote the difference between the equilibrium potentials for the reduction of water and oxidation of iron. Thus, the bars indicate the tendency of the metal to corrode in deaerated aqueous solutions with varying pH. They bracket the location of the corrosion potential and, thus, indicate whether the corrosion potential will establish itself in the 'corrosion' or 'passivation' regions. The numbers associated with the bars represent the experimentally determined relative attack. It is clear that the observed relative attack is substantially greater in the regions where a solid phase is predicted to be stable than in the regions where no solid phase is predicted. Thus, subject to the limitations discussed above, the stability diagrams can be used for the qualitative assessment of the tendency of metals to corrode, and for estimating the range of the corrosion potential.

Following the pioneering work of Pourbaix and his coworkers, further refinements of stability diagrams were made to extend their range of applicability. These refinements were made possible by the progress of the thermodynamics of electrolyte solutions and alloys. Specifically, further developments focused on

1. generation of diagrams at elevated temperatures,
2. taking into account the active solution species other than protons and water molecules,
3. introduction of solution nonideality, which influences the stability of species through realistically modeled activity coefficients,
4. introduction of alloying effects by accounting for the formation of mixed oxides and the nonideality of alloy components in the solid phase, and
5. flexible selection of independent variables, other than E and pH, for the generation of diagrams.

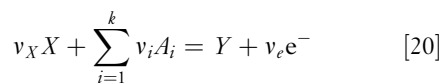
2.38.2.3.1 Diagrams at elevated temperatures

The key to the construction of stability diagrams at elevated temperatures is the calculation of the standard chemical potentials μ_i^0 of all individual species as a function of temperature. In earlier studies, the entropy correspondence principle of Criss and Cobble²¹ was used for this purpose. Macdonald and Cragnolino⁶³ reviewed the development of E -pH diagrams at elevated temperatures until the late 1980s.

The HKF equation of state^{22,23} formed a comprehensive basis for the development of E -pH diagrams at temperatures up to 300 °C for iron, zinc, chromium, nickel, copper, and other metals (Beveriskog and Puigdomenech,⁶⁴⁻⁶⁹ Anderko *et al.*⁶²) An example of a high temperature E -pH diagram is shown for Fe at 300 °C in the lower diagram of **Figure 1**. Comparison of the Fe diagrams at room temperature and 300 °C shows a shift in the predominance domains of cations to lower pH values and an expansion of the domains of metal oxyanions at higher pH values. Such effects are relatively common for metal-water systems.

2.38.2.3.2 Effect of multiple active species

The concept of stability diagrams can be easily extended to solutions that contain multiple chemically active species other than H^+ and H_2O . In such a general case, the simple reaction **eqn [15]** needs to be extended as



where the species X and Y contain at least one common element and A_i ($i = 1, \dots, k$) are the basis species that are necessary to define equilibrium equations between all species containing a given element. Reaction **eqn [20]** is normalized so that the stoichiometric coefficient for the right-hand side species (Y) is equal to 1. Such an extension results in generalized

expressions for the boundaries between predominance regions (eqns [16] and [17]). The equilibrium expression for the chemical reactions (eqn [20] with $v_e = 0$) then becomes

$$\begin{aligned} \ln K &= \left(\ln a_Y - v_X \ln a_X - \sum_{i=1}^k v_i \ln a_{A_i} \right) \\ &= \frac{1}{RT} \left(\mu_Y^0 - \mu_X^0 - \sum_{i=1}^k v_i \mu_{A_i}^0 \right) \end{aligned} \quad [21]$$

and the expression for an electrochemical reaction (eqn [20] with $v_e \neq 0$) takes the form:

$$E_0 = E_0^0 + \frac{RT}{Fv_e} \left(\ln a_Y - v_X \ln a_X - \sum_{i=1}^k v_i \ln a_{A_i} \right) \quad [22]$$

Thus, the expression for the boundary lines become more complicated but the algorithm for generating the diagrams remains the same, that is, the predominance areas can still be determined semianalytically.

The strongest effect of solution species on the stability diagrams of metals is observed in the case of complex-forming ligands and species that form stable, sparingly soluble solid phases other than oxides or hydroxides (e.g., sulfides or carbonates). Several authors focused on stability diagrams for metals such as iron, nickel, or copper in systems containing sulfur species (Biernat and Robbins,⁷⁰ Froning *et al.*,⁷¹ Macdonald and Syrett,⁷² Macdonald *et al.*,^{73,74} Chen and Aral,⁵⁸ Chen *et al.*,⁵⁹ Anderko and Shuler⁷⁵). This is due to the importance of iron sulfide phases, which have a strong tendency to form in aqueous environments even at very low concentrations of dissolved hydrogen sulfide. The stability domains of various iron sulfides can be clearly rationalized using E -pH diagrams. Diagrams have also been developed for metals in brines (Pourbaix,⁷⁶ Macdonald and Syrett,⁷² Macdonald *et al.*,^{73,74} Kesavan *et al.*,⁷⁷ Muñoz-Portero *et al.*⁷⁸). The presence of halide ions manifests itself in the stability of various metal-halide complexes. Typically, the effect of halides on the thermodynamic stability is less pronounced than the effect of sulfides. However, concentrated brines can substantially shrink the stability regions of metal oxides and promote the active behavior of metals. An example of such effects is provided by the diagrams for copper in concentrated bromide brines (Muñoz-Portero *et al.*⁷⁸) Effects of formation of various carbonate and sulfate phases have also been reported (Bianchi and Longhi,⁷⁹ Pourbaix⁷⁶).

The formation of complexes of metal ions with organic ligands (e.g., chelants) frequently leads to a

significant decrease in the stability of metal oxides, which may, under some conditions, indicate an increased dissolution tendency in the passive state (Silverman,^{80,81} Kubal and Panacek,⁸² Silverman and Silverman⁸³). An important example of the importance of complexation is provided by the behavior of copper and other metals in ammoniated environments. **Figure 2** (upper diagram) illustrates an E -pH diagram for copper in a 0.2 m NH_3 solution. As shown in the figure, the copper oxide stability field is bisected by the stability area of an aqueous complex. The formation of a stable dissolved complex indicates that the passivity of copper and copper-base alloys may be adversely affected in weakly alkaline NH_3 -containing environments. In reality, ammonia attack on copper-base alloys is observed in steam cycle environments.⁶³ Stability diagrams are a useful tool for the qualitative evaluation of the tendency of metals to corrode in such environments.

2.38.2.3.3 Diagrams for nonideal solutions

As long as the solution is assumed to be ideal (i.e., $\gamma_i = 1$ in eqn [2]), the chemical and electrochemical equilibrium expressions can be written in an analytical form, and the E -pH diagrams can be generated semianalytically. For nonideal solutions, the analytical character of the equilibrium lines can be preserved if fixed activity coefficients are assumed for each species (see Bianchi and Longhi⁷⁹). However, such an approach does not have a general character because the activities of species change as a function of pH. This is due to the fact that, in real systems, pH changes result from varying concentrations of acids and bases, which influence the activity coefficients of all solution species. In a nonideal solution, the activities of all species are inextricably linked to each other because they all are obtained by differentiating the solution's excess Gibbs energy with respect to the number of moles of the individual species.² Therefore, in a general case, the equilibrium expressions (eqns [21] and [22]) can no longer be expressed by analytical expressions. This necessitates a modification of the algorithm for generating stability diagrams. A general methodology for constructing stability diagrams of nonideal solutions has been developed by Anderko *et al.*⁶²

In general, the nonideality of aqueous solutions may shift the location of the equilibrium lines because the activity coefficients may vary by one or even two orders of magnitude. Such effects become pronounced in concentrated electrolyte solutions and in mixed-solvent solutions, in which water is not necessarily the predominant solvent.

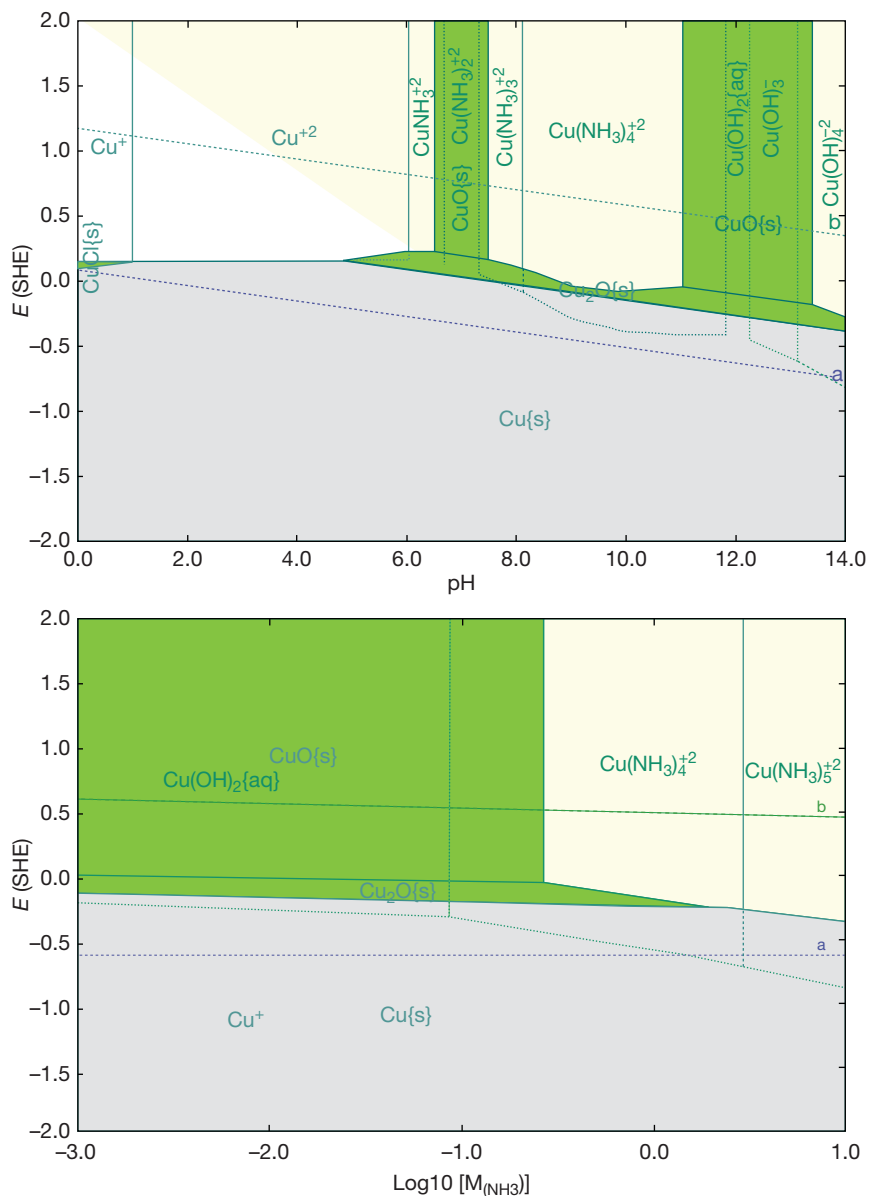


Figure 2 Use of thermodynamic stability diagrams to analyze the effect of ammonia on the corrosion of copper. The upper plot is an E - pH diagram for Cu in a 0.2 m NH_3 solution. The lower plot is a potential-ammonia molality diagram.

2.38.2.3.4 Diagrams for alloys

The vast majority of the published stability diagrams have been developed for pure metals. However, several studies have been devoted to generating stability diagrams for alloys, particularly those from the Fe-Ni-Cr-Mo family (Cubicciotti,^{84,85} Beverskog and Puigdomenech,⁶⁹ Yang *et al.*,⁸⁶ Anderko *et al.*⁸⁷). In general, a stability diagram for an alloy is a superposition of partial diagrams for the individual components of the alloy.⁶⁹ However, the partial diagrams

are not independent because the alloy components form a solid solution and, therefore, their properties are linked. The superposition of partial diagrams makes it possible to analyze the tendency of alloy components for preferential dissolution. This may be the case when a diagram indicates that one alloy component has a tendency to form a passivating oxide, whereas another component has a tendency to form ions. Also, stability diagrams indicate in a simple way which alloy component is more anodic.

There are two key effects of alloying on thermodynamic equilibrium, that is, the formation of mixed solid corrosion products and the nonideality of alloy components in the solid phase. The formation of mixed solid corrosion products may be particularly significant for passive systems. Fe–Ni–Cr alloys may form mixed oxides, including NiFe_2O_4 , FeCr_2O_4 , and NiCr_2O_4 . Such oxides may be more stable than the single oxides of chromium, nickel, and iron, which appear in stability diagrams for pure metals. E –pH diagrams that include mixed oxide phases have been reported by Cubicciotti,^{84,85} Beverskog and Puigdomenech,⁶⁹ and Yang *et al.*⁸⁶ for Fe–Ni–Cr alloys in ideal aqueous solutions.

Another fundamental effect of alloying on the thermodynamic behavior results from the nonideality of the solid solution phase. In contrast to pure metals, the activity of a metal in an alloy is no longer equal to 1. This affects the value of the equilibrium potential for metal dissolution, which determines the upper boundary of the stability field of an alloy component on an E –pH diagram. As with the liquid phase, the activity of solid solution components can be obtained from a comprehensive excess Gibbs energy model of the solid phase. Thermodynamic modeling of alloys is a very wide area of research, which is beyond the scope of this chapter (see Lupis⁸⁸ and Saunders and Miodownik⁸⁹ for reviews). Detailed models have been developed for the thermodynamic behavior of alloys on the basis of high temperature data that are relevant to metallurgical processes. These models can be, in principle, extrapolated to lower temperatures that are of interest in aqueous corrosion. Despite the inherent uncertainties associated with extrapolation, estimates of activities of alloy components can be obtained in this way and incorporated into the calculation of stability diagrams. Such an approach was used by Anderko *et al.*⁸⁷ in a study in which solid solution models were coupled with an algorithm for generating stability diagrams for Fe–Ni–Cr–Mo–C and Cu–Ni alloys. In that work, the solid solution models of Hertzman,⁹⁰ Hertzman and Jarl,⁹¹ and Anderson and Lange⁹² were implemented to estimate the activities of alloy components.

It should be noted that the effect of varying activities of alloy components on E –pH diagrams is relatively limited. This is due to the fact that alloy phase nonideality, while crucial for modeling alloy metallurgy, is only a secondary contribution to the energetics of reactions between metals and aqueous species. The effect of alloy solution nonideality manifests itself in a limited shift of the upper boundary of

the metal stability area in E –pH diagrams. The effect of mixed oxide phases is usually much more pronounced on stability diagrams.

2.38.2.3.5 Potential–concentration diagrams

Once the thermodynamic treatment of solution chemistry is extended to allow for the effect of species other than H^+ and H_2O (see eqns [21] and [22]), other independent variables become possible in addition to E and pH. The chemical and electrochemical boundaries can then be calculated as a function of concentration variables other than pH. In particular, the stability diagrams can be generated as a function of the concentration of active solution species that may react with metals through precipitation, complexation, or other reactions. Thus, an extension of E –pH diagrams to E –species concentration diagrams is relatively straightforward. The algorithm developed by Anderko *et al.*⁶² for nonideal solutions is equally applicable to E –pH and E –concentration diagrams. An example of such a diagram is provided in the lower plot of Figure 2. This plot is an E – NH_3 molality diagram and illustrates the thermodynamic behavior of copper when increasing amounts of ammonia are added to an aqueous environment. In this simulation, pH varies with ammonia concentration. However, pH is less important in this case than the concentration of NH_3 because the stability of copper oxide is controlled by the formation of copper–ammonia complexes. The diagram indicates at which concentration of ammonia the copper oxide film becomes thermodynamically unstable, thus increasing the tendency for metal dissolution.

2.38.2.4 Chemical Equilibrium Computations

While the E –concentration diagrams are merely an extension of Pourbaix's original concept of stability diagrams, a completely different kind of thermodynamic analysis can also be performed using electrolyte thermodynamics. This kind of analysis relies on solving the chemical equilibrium expressions without using the potential as an independent variable. Assuming that temperature, pressure, and starting amounts of components (both metals and solution species) are known, the equilibrium state of the system of interest can be found by simultaneously solving the following set of equations:

1. chemical equilibrium equations (eqn [6]) for a linearly independent set of reactions that link all the species that exist in the system; this set of

- equations also includes solid–liquid equilibrium reactions (or precipitation equilibria);
2. if applicable, vapor–liquid and, possibly, liquid–liquid equilibrium equations (i.e., the equality of chemical potentials of species in coexisting phases),
 3. material balance equations for each element in the system, and
 4. electroneutrality balance condition.

Once the solution is found, the potential can be calculated using the Nernst equation for any redox pair in the equilibrated system. It should be noted that procedures for solving these equations are very involved and require sophisticated numerical techniques. Methods for solving such electrolyte equilibrium problems were reviewed by Zemaitis *et al.*⁴ and Rafal *et al.*⁷ and will not be discussed here.

The solution of the chemical equilibrium conditions provides detailed information about the thermodynamically stable form(s) of the metal in a particular system. This is in contrast with the information presented on the E – pH diagrams, which essentially indicate whether a given oxidation reaction (e.g., dissolution of a metal) can occur simultaneously with a given reduction reaction (e.g., reduction of water). In the chemical equilibrium algorithm outlined above, all possible reduction and oxidation equilibria are solved simultaneously. This provides very detailed information about the chemical identity of all species and their concentrations. On the other hand, this kind of information is less

conductive to gaining qualitative insight into the key anodic and cathodic reactions that occur in the system.

To visualize the information obtained from detailed chemical equilibrium computations, stability diagrams can be constructed by selecting key independent variables. Such diagrams can be referred to as ‘chemical’ as opposed to ‘electrochemical’ because they do not involve the potential as an independent variable. An example of such a diagram is shown in **Figure 3**, which shows the stability areas of solid corrosion products of iron as a function of the amount of dissolved iron and hydrogen sulfide in 1 kg of water. Diagrams of this type can be generated by repeatedly solving the chemical equilibrium expressions outlined above and tracing the stability boundaries of various species (Lencka *et al.*,⁹⁴ Sridhar *et al.*⁹³). Such diagrams are useful for illustrating the transition between various corrosion products (e.g., iron sulfide and magnetite in **Figure 3**) as a function of environmental conditions. Diagrams of this kind have been generated by Sridhar *et al.*⁹⁵ to identify the conditions under which $FeCO_3$, Fe_3O_4 , and Fe_2O_3 coexist as corrosion products of carbon steel. This approach was used to elucidate conditions that are conducive to intergranular stress corrosion cracking in weakly alkaline carbonate systems, which has been associated with the transition between iron carbonate, iron (II), and iron (III) corrosion products.

It should be noted that simplified ‘chemical’ diagrams can be generated using activities rather than

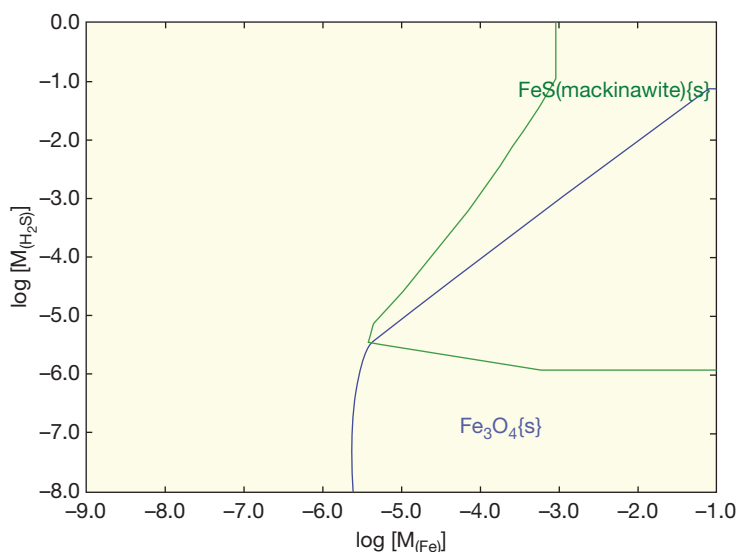


Figure 3 Stability diagram for solid iron corrosion products as a function of the molality of dissolved Fe and the total number of moles of H_2S per 1 kg of H_2O . The diagram has been constructed by computing the equilibrium states of solid–liquid–vapor reactions.⁹³

concentrations of species as independent variables. Such an approach makes it possible to obtain the 'chemical' diagrams in a semianalytical way, as with the classical Pourbaix diagrams. An example of such diagrams is provided by Mohr and McNeil⁹⁶ for the Cu–H–O–Cl system. However, such simplified 'chemical' diagrams suffer from the fundamental disadvantage that species activities are not directly measurable and are, therefore, much less suitable as independent variables than concentrations. Comprehensive 'chemical' diagrams can be obtained only by simultaneously solving the chemical and phase equilibrium expressions for each set of conditions, preferably with the help of a realistic model for liquid-phase activity coefficients.

2.38.2.5 Problems of Metastability

The main strength of the stability diagrams lies in their purely thermodynamic nature. Accordingly, they can be generated using equilibrium thermochemical properties that are obtained from a variety of classical experimental sources (e.g., solubility, vapor pressure, calorimetric or electromotive force measurements for bulk systems) without recourse

to any electrochemical kinetic studies of surfaces. At the same time, the purely thermodynamic nature of the diagrams is also their main weakness. An important limitation of the stability diagrams is the fact that they predict the equilibrium phases, whereas the actual corrosion behavior may be controlled by metastable phases. The same limitation applies to the detailed thermodynamic computations outlined earlier.

To illustrate the problems of metastability, it is instructive to examine how E –pH diagrams can be used to rationalize the Faraday paradox of iron corrosion in nitric acid, which historically played a great role in establishing the concept of passivity (Macdonald⁹⁷). Faraday's key observation was that iron easily corroded in dilute nitric acid with the evolution of hydrogen. However, it did not corrode with an appreciable rate in concentrated HNO_3 solutions despite their greater acidity. When scratched in the solution, an iron sample would corrode for a short time and, then, rapidly passivate. A stability diagram for this system is shown in Figure 4. This figure presents a superposition of an E –pH diagram for iron species and another one for nitrogen species. Dilute nitric acid is a weak oxidizing agent and, therefore, the main cathodic reaction in this case is

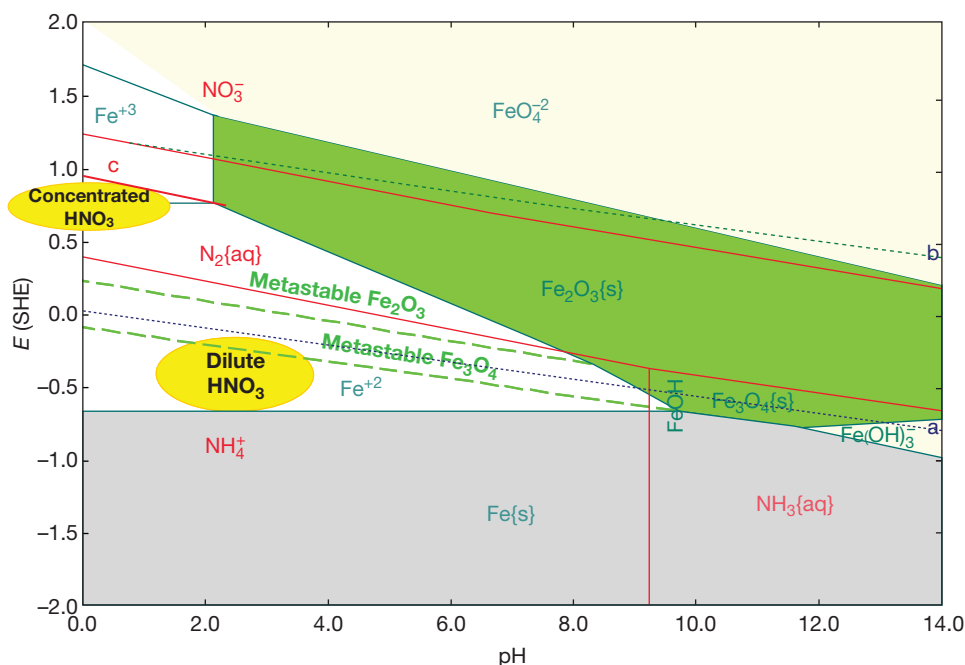
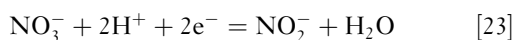


Figure 4 Metastability on the E –pH diagram and the interpretation of the Faraday paradox of iron corrosion in dilute and concentrated nitric acid. The stability fields of the oxides (Fe_3O_4 and Fe_2O_3) are extended into the metastable region (long dashed lines). An E –pH diagram for nitrogen is superimposed on the diagram for Fe. The line 'c' is a metastable equilibrium line for the reduction of HNO_3 to HNO_2 . The ovals marked as 'concentrated HNO_3 ' and 'dilute HNO_3 ' indicate the mixed potential ranges that are expected for iron in concentrated and dilute HNO_3 , respectively.

the common reaction of reduction of H^+ ions. The equilibrium potential for this reaction is given by the dotted line marked as 'a' in the diagram. The anodic process is the oxidation of Fe, for which the equilibrium potential is given by the equilibrium line between Fe(s) and Fe^{2+} in the diagram. Thus, the corrosion potential will establish itself between the 'a' line and the upper limit of the stability field of elemental iron. This corrosion potential range is approximately shown by the lower ellipsoid in **Figure 4**. In this region, the stable iron species is Fe^{2+} and, therefore, the stability diagram predicts the dissolution of iron with the formation of Fe^{2+} ions. Unlike dilute nitric acid, concentrated HNO_3 is a strong oxidizing agent. The main reduction reaction in this case is



The equilibrium potential for this reaction is shown by a line marked as 'c' in **Figure 4**. It should be noted that the nitrite ions (NO_2^-) are metastable and, therefore, a stability field of nitrites does not appear on an E -pH diagram of nitrogen. Nevertheless, the equilibrium potential for reaction eqn [21] can be easily calculated as described above. It lies within the stability field of elemental nitrogen $N_2(aq)$. The corrosion potential will then establish itself at a much higher potential, relatively close to the dominant cathodic line 'c.' The likely location of the corrosion potential is outlined in **Figure 4** by an ellipsoid marked 'concentrated HNO_3 .' However, the stable species in this region are the Fe^{2+} and Fe^{3+} ions. Thus, the stability diagram does not explain the Faraday paradox as long as only stable species are considered. As indicated by Macdonald,⁹⁷ the E -pH diagram becomes consistent with experimental observation when the existence of metastable phases is allowed for. The dashed lines in **Figure 4** show the metastable extensions of the Fe^{2+}/Fe_3O_4 and Fe_3O_4/Fe_2O_3 equilibrium lines into the acidic range. Thus, it is clear that the corrosion potential of iron in concentrated HNO_3 is likely to establish itself in a potential range in which metastable iron oxides are stable. In contrast, the metastable solids are not expected to form at the low potentials that correspond to dilute HNO_3 environments (i.e., below the Fe^{2+} /metastable Fe_3O_4 boundary). If the surface is scratched, the large supply of H^+ ions near the scratch will create conditions under which the potential will be below the 'a' line and short-term hydrogen evolution will follow. However, this will lead to a rapid depletion of the H^+ ions, and the potential will shift to higher values, at which metastable phases can lead to passivation.

The formation of metastable solid phases is fairly common. The metastability of chromium oxide phases is important for the passivity of Fe-Ni-Cr alloys in acidic solutions. Although the E -pH diagrams indicate that chromium oxides/hydroxides cease to be stable in relatively weakly acidic solutions, the practical passivity range extends to a more acidic range for numerous alloys. Also, the metastability of iron sulfide phases plays an important role in the behavior of corrosion products in H_2S containing environments. Anderko and Shuler⁷⁵ used stability diagrams to evaluate the natural sequence of formation of various iron sulfide phases (e.g., amorphous FeS, mackinawite, pyrrhotite, greigite, marcasite, or pyrite). The sequence of formation of such phases could be predicted on the basis of the simple but reasonably accurate rule that the order of formation of solids is the inverse of the order of their thermodynamic stability. Stability diagrams are then used to predict the conditions under which various metastable phases are likely to form.

Thermodynamics provides a convenient starting point in the simulation of aqueous corrosion. Although it is inherently incapable of predicting the rates of interfacial phenomena, it is useful for predicting the final state toward which the system should evolve if it is to reach equilibrium. Furthermore, the computation of the final, thermodynamic equilibrium state can be refined by taking into account the metastable phases. In addition to determining the equilibrium state in metal-environment systems, electrolyte thermodynamics provides information on the properties of the environment. Such information, including speciation in the liquid phase, concentrations and activities of individual species, and phase equilibria, is necessary for constructing kinetic models of corrosion.

2.38.3 Modeling the Kinetics of Aqueous Corrosion

Aqueous corrosion is intrinsically an electrochemical process that involves charge transfer at a metal-solution interface. Because aqueous corrosion is a heterogeneous process, it involves the following fundamental steps:

1. reactions in the bulk aqueous environment,
2. mass transport of reactants to the surface,
3. charge transfer reactions at the metal surface,
4. mass transport of reaction products from the surface, and
5. reactions of the products in the bulk environment.

Reactions in the bulk environment (1 and 5) can be considered, with some important exceptions, to be equilibrium. As long as they are treated as equilibrium phenomena, they remain within the domain of electrolyte thermodynamics. On the other hand, the charge transfer reactions at the surface (3), and their coupling with mass transport (2 and 4) require the tools of electrochemical kinetics. In this section, we review the fundamentals of modeling approaches to electrochemical kinetics.

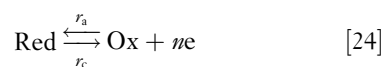
The objective of modeling the kinetics of aqueous corrosion is to relate the rate of electrochemical corrosion to external conditions (e.g., environment composition, temperature, and pressure), flow conditions, and the chemistry and metallurgical characteristics of the corroding interface. The two main quantities that can be obtained from electrochemical modeling are the corrosion rate (v_{corr} often expressed as the corrosion current density i_{corr}) and corrosion potential (E_{corr}). For practical applications, the calculation of the corrosion rate is of primary interest for simulating general corrosion and the rate of dissolution in occluded environments such as pits or crevices. The value of the corrosion potential (E_{corr}) is also of interest because there is often a relationship between the value of the corrosion potential and the type of corrosion damage that occurs. In general, if the corrosion potential is above a certain critical potential (E_{crit}), a specific form of corrosion that is associated with E_{crit} can occur, typically at a rate that is determined by the difference $E_{\text{corr}} - E_{\text{crit}}$. This general observation applies to localized corrosion including pitting, crevice corrosion, intergranular stress corrosion cracking, and so on. An internally consistent model for general corrosion should simultaneously provide reasonable values of the corrosion rate and corrosion potential. Thus, the computation of the corrosion potential is of interest not so much for modeling general corrosion but for predicting other forms of corrosion.

2.38.3.1 Kinetics of Charge-Transfer Reactions

The theory of charge-transfer reactions is well developed and has been reviewed in detail by a number of authors including Vetter,⁹⁸ Bockris and Reddy,⁹⁹ Kaesche,¹⁰⁰ Bockris and Khan,¹⁰¹ and Gileadi.¹⁰² Here, we summarize the key relationships that form the basis of modeling.

Considering a simple reaction of transfer of n electrons between two species, a reduced form 'Red'

and an oxidized form 'Ox':



the current density associated with this reaction is, according to Faraday's law, equal to the difference between the anodic rate v_a and the cathodic rate v_c , multiplied by nF :

$$i = nF(v_a - v_c) \quad [25]$$

According to the theory of electrochemical kinetics,⁹⁸ the rates of the anodic and cathodic reactions are related to the potential and the concentrations of the reacting species at the phase boundary, that is

$$i_a = nFv_a = nFk_a c_{r,s}^{x,r} \exp\left(\frac{\alpha_a nFE}{RT}\right) \quad [26]$$

$$i_c = -nFv_c = -nFk_c c_{o,s}^{x,o} \exp\left(-\frac{\alpha_c nFE}{RT}\right) \quad [27]$$

where k_a and k_c are the anodic and cathodic rate constants, α_a and α_c are the anodic and cathodic electrochemical transfer coefficients, $c_{r,s}$ and $c_{o,s}$ are the concentrations of the reduced (r) and oxidized (o) forms at the surface, respectively, and x,r and x,o are the reaction orders with respect to the reduced and oxidized species. For a given individual redox process, the anodic and cathodic electrochemical transfer coefficients are interrelated as $\alpha_c = 1 - \alpha_a$. The total current density for reaction eqn [24] is then

$$i = nFk_a c_{r,s}^{x,r} \exp\left(\frac{\alpha_a nFE}{RT}\right) - nFk_c c_{o,s}^{x,o} \exp\left(-\frac{\alpha_c nFE}{RT}\right) \quad [28]$$

At the equilibrium (reversible) potential E_0 , the current density i is equal to zero. In the absence of a net current, the concentrations of the species at the surface are equal to their bulk concentrations (i.e., $c_{r,s} = c_{r,b}$ and $c_{o,s} = c_{o,b}$). Then, the current density of the anodic process is equal to that of the anodic process and is defined as the exchange current density i_0 , that is,

$$i_0 = nFk_a c_{r,b}^{x,r} \exp\left(\frac{\alpha_a nFE_0}{RT}\right) = nFk_c c_{o,b}^{x,o} \exp\left(-\frac{\alpha_c nFE_0}{RT}\right) \quad [29]$$

Using eqn [29], the equation for the current density [28] can be expressed in terms of the exchange current density and the overvoltage $\eta = E - E_0$:

$$i = i_0 \left(\frac{c_{r,s}}{c_{r,b}}\right)^{x,r} \exp\left(\frac{\alpha_a nF(E - E_0)}{RT}\right) - i_0 \left(\frac{c_{o,s}}{c_{o,b}}\right)^{x,o} \exp\left(-\frac{\alpha_c nF(E - E_0)}{RT}\right) \quad [30]$$

The ratios $c_{r,s}/c_{r,b}$ and $c_{o,s}/c_{o,b}$ depend on the transport of reactants and products to and from the corroding interface. If the mass transport is slow compared to charge transfer, the surface concentrations become different from those in the bulk. Conversely, if charge transfer is slow relative to mass transfer, the reaction is under charge transfer control and the ratios are equal to one not only at the equilibrium potential. In such a case, eqn [30] takes a particularly simple form and is usually referred to as the Butler–Volmer equation for charge-transfer reactions:

$$i = i_0 \exp\left(\frac{\alpha_a nF(E - E_0)}{RT}\right) - i_0 \exp\left(-\frac{\alpha_c nF(E - E_0)}{RT}\right) \quad [31]$$

The electrochemical transfer coefficient α depends on the mechanism of the charge transfer reaction. For some reactions, its value can be deduced from mechanistic considerations. However, in many cases, it needs to be determined empirically. It can be determined in the form of empirical Tafel coefficients defined as the slope of a plot of potential against the logarithm of current density, that is

$$\beta_a = \frac{dE}{d \ln i_a}; \quad \beta_c = \frac{dE}{d \ln i_c} \quad [32]$$

which yields

$$\beta_a = \frac{RT}{\alpha_a nF}; \quad \beta_c = \frac{RT}{\alpha_c nF} \quad [33]$$

or, in a more traditional decimal logarithm form:

$$b_a = \frac{2.303RT}{\alpha_a nF}; \quad b_c = \frac{2.303RT}{\alpha_c nF} \quad [34]$$

Then, the Tafel coefficients b_a or b_c can be used in eqns [28] or [30] instead of the electrochemical transfer coefficient.

The above formalism includes both the cathodic and anodic process for a particular redox couple. However, in practical corrosion modeling, it is usually entirely sufficient to include only either a cathodic or an anodic partial current for a given redox process. Specifically, the cathodic partial process can be neglected for metal-ion reactions because the deposition of metal ions (i.e., the reverse of metal dissolution) is typically not of practical significance in corrosion. Similarly, the anodic partial process can be usually neglected for oxidizing agents because it is only their reduction that is of interest for corrosion. There are some exceptions to this rule, for example, in the case of relatively noble metals whose ions can be reduced under realistic conditions. Nevertheless, in the remainder of this review, we will separately consider partial anodic and cathodic processes for corrosion-related reactions.

As mentioned above, the concentrations of reactants and products at the surface depend on the mass transport to and from the corroding interface. In general, three mechanisms contribute to mass transport, that is, diffusion, migration, and convection. In many practical applications, migration can be neglected. This is the case for the transport of neutral molecules in any environment and, also, for the transport of charged species in environments that contain appreciable amounts of background electrolytic components (e.g., as supporting electrolyte). Migration becomes important in ionic systems in which there is no supporting electrolyte. We will return to the treatment of migration later in this review. If migration is neglected, the treatment of mass transfer by diffusion and convection can be simplified by using the concept of the Nernst diffusion layer. According to this concept, the environment near the corroding surface can be divided into two regions. In the inner region, called the Nernst diffusion layer, convection is negligible and diffusion is the only mechanism of transport. In the outer region, concentrations are considered to be uniform and equal to those in the bulk solution. Thus, the concentration changes linearly from the surface concentration to the bulk concentration over a distance δ , which is the thickness of the diffusion layer. In such a model, the flux of a species i in the vicinity of a corroding interface is given by Fick's law

$$\mathcal{F}_i = -D_i \left(\frac{\partial c_i}{\partial z} \right)_{z=0} \quad [35]$$

where D_i is the diffusion coefficient of species i and z in the direction perpendicular to the surface. Integration of eqn [35] over the thickness of the diffusion layer gives:

$$\mathcal{F}_i = -D_i \frac{c_{i,b} - c_{i,s}}{\delta_i} \quad [36]$$

It should be noted that the diffusion layer thickness δ is not a general physical property of the system. Rather, it is a convenient mathematical construct that makes it possible to separate the effects of diffusion and convection. It depends on the flow conditions, properties of the environment, and the diffusion coefficient of individual species. Thus, it may be different for various species. Methods for calculating δ will be outlined later in this review. Equation [36] can be applied to both the reactants that enter into electrochemical reactions at the interface and to corrosion products that leave the interface. Then, it can be combined with Faraday's law to obtain the current

density. For an oxidant o , eqn [36] yields an expression for a cathodic partial current density:

$$i_c = nF\mathcal{J}_o = -nFD_o \frac{c_{o,b} - c_{o,s}}{\delta_o} \quad [37]$$

According to eqn [37], the current density reaches a maximum, limiting value when the surface concentration $c_{o,s}$ decreases to zero. This condition defines the limiting current density, that is

$$i_{c,L} = -\frac{nFD_o c_{o,b}}{\delta_o} \quad [38]$$

For a corrosion product (e.g., Me ions), an analogous equation can be written for an anodic current density

$$i_a = nF\mathcal{J}_{Me} = -nFD_{Me} \frac{c_{Me,b} - c_{Me,s}}{\delta_{Me}} \quad [39]$$

In eqn [39], the surface concentration is typically limited by the solubility of corrosion products. Thus, a limiting anodic current density can be reached when the surface concentration of metal ions corresponds to the metal solubility, that is

$$i_{a,L} = -nFD_{Me} \frac{c_{Me,b} - c_{Me,sat}}{\delta_{Me}} \quad [40]$$

Combination of eqns [26]–[28] for charge-transfer processes and the simplified mass-transport equations (eqns [37] and [39]) yields a general formalism for electrochemical processes that are influenced by both charge transfer and mass transport. For example, for a cathodic process, the current density obtained from eqn [37] is equal to that obtained from eqn [27]. Thus, the surface concentration of the diffusing species can be obtained from eqn [37] and substituted into eqn [27]. The resulting equation can be solved analytically for i_c for some values of the reaction order x_o . If the reaction order is equal to one (i.e., $x_o = 1$ in eqn [27]), a particularly simple relationship is obtained for i_c , that is

$$\frac{1}{i_c} = \frac{1}{i_{c,ct}} + \frac{1}{i_{c,L}} \quad [41]$$

where $i_{c,L}$ is the limiting current density (eqn [38]) and $i_{c,ct}$ is the charge-transfer contribution to the current density. The latter quantity is given by eqn [27] with the bulk concentration $c_{o,b}$ replacing the surface concentration, that is

$$i_c = -nFk_c c_{o,b}^{x_o} \exp\left(-\frac{\alpha_c nFE}{RT}\right) \quad \text{with } x_o = 1 \quad [42]$$

An analytical formula can also be obtained when $x_o = 0.5$.¹⁰³ For an arbitrary value of the reaction

order, the current density can be computed numerically by solving a single equation.

It should be noted that eqns [26] and [27] are particularly simple forms for reactions of the type [24], in which no species other than *Red* and *Ox* participate. In general, the preexponential part of eqns [26] and [27] depends on the mechanism of a particular electrochemical reaction. In general, the preexponential terms of eqns [26] and [27] can be generalized using the surface coverage factors, θ_i , for reactive species that participate in electrochemical processes, that is,

$$i_a = nFk_a \theta_1^{x_1} \theta_2^{x_2} \dots \theta_m^{x_m} \exp\left(\frac{\alpha_a nFE}{RT}\right) \quad [43]$$

$$i_c = -nFk_c \theta_1^{x_1} \theta_2^{x_2} \dots \theta_m^{x_m} \exp\left(-\frac{\alpha_c nFE}{RT}\right) \quad [44]$$

The surface coverage factors, θ_i , are further related to the concentrations (or, more precisely, activities) of individual species at the metal surface through appropriate adsorption isotherms. In general, analysis of reaction mechanisms on the basis of experimental data leads to a substantial simplification of eqns [43] and [44]. In many cases, activities of species can be directly used in the kinetic expressions rather than the surface coverage fractions.

The above formalism makes it possible to set up a model of electrochemical kinetics on a corroding metal surface by considering the following steps:

1. determining all possible partial cathodic and anodic processes that may occur in a given metal-environment combination;
2. writing equations for the partial cathodic or anodic current densities associated with charge transfer reactions (eqns [43] and [44] or simplifications thereof); and
3. writing equations for the mass transport of the species that participate in the charge-transfer reactions (eqns [37] and [39]). In some simple, but realistic cases a combination of the charge-transfer and mass-transport equations results in analytical formulas such as eqn [41] for partial electrochemical processes.

Once the equations for the partial anodic and cathodic processes are established, the behavior of a corroding surface can be modeled on the basis of the Wagner–Traud¹⁰⁴ theory of metallic corrosion, often referred to as the mixed potential theory. According to the mixed potential theory, the sum of all partial anodic currents is equal to the sum of all cathodic

currents. Further, it is assumed that the electrical potential of the metal at an anodic site is equal to that at a cathodic site. These assumptions follow from the requirement that charge accumulation within a metal cannot occur and, therefore, the electrons produced as a result of oxidation processes must be consumed in the reduction processes. Therefore, in a freely corroding system, we have

$$\sum_j A_a i_{a,j} + \sum_j A_c i_{c,j} = 0 \text{ at } E = E_{\text{corr}} \quad [45]$$

where A_a and A_c are the areas over which the anodic and cathodic reactions occur, respectively. The first sum in eqn [45] enumerates all anodic partial reactions and the second sum pertains to all cathodic reactions. Equation [45] is written using the sign conventions introduced earlier, in which the cathodic processes are written with a negative sign.

Equation [45] can be solved to obtain the corrosion potential, E_{corr} . Then, the corrosion current density and, equivalently, the corrosion rate, can be computed from the anodic current density for metal dissolution at the corrosion potential, that is

$$i_{\text{corr}} = i_{a,\text{Me}}(E_{\text{corr}}) \quad [46]$$

At potentials that deviate from the corrosion potential, the left-hand side of eqn [45] represents the predicted current. Such a computed current versus potential relationship can be compared with experimentally determined polarization behavior.

In the case of general corrosion, $A_a = A_c$ and the solution of eqns [45] and [46] yields the corrosion potential and general corrosion rate. For localized corrosion, there is usually a great disparity between the areas on which the anodic and cathodic processes operate.

2.38.3.2 Modeling Adsorption Phenomena

Before discussing partial electrochemical reactions, it is necessary to outline the treatment of adsorption because the presence of adsorbed species is frequently assumed to derive expressions for electrochemical processes.

Adsorption of neutral molecules and ions on metals has been reviewed in detail by Gileadi,¹⁰⁵ Damaskin *et al.*,¹⁰⁶ and Habib and Bockris.¹⁰⁷ In general, adsorption leads to the reduction of the surface area that is accessible to electrochemical reactions. In such cases, adsorption results in a reduction in the rate of both anodic and cathodic processes. Thus, the rates of electrochemical reactions become modified

by the factor $(1 - \sum \theta_j)$, in which θ_j is a coverage fraction by species j . At the same time, adsorption may result in the formation of surface complexes that have different dissolution characteristics. An example of such a dual effect is provided by halide ions on Fe-group metal surfaces corroding in the active state. At relatively low or moderate halide concentrations, adsorption of halides leads to a reduction in electrochemical reaction rates. However, at higher halide concentrations, the adsorbed halide ions interfere with the mechanism of anodic dissolution of iron, which may lead to an increase in the corrosion rate.

A general formalism for modeling the effect of adsorption on electrochemical reactions is provided by the Frumkin isotherm. The Frumkin formalism takes into account the interactions between the species adsorbed on the surface. It results from the requirement that the rate of adsorption is equal to the rate of desorption in the stationary state,¹⁰⁵ that is

$$v_{\text{ads},i} = v_{\text{des},i} \quad [47]$$

where the subscript i denotes any adsorbable species. The rate of adsorption is given by

$$v_{\text{ads},i} = k_{\text{ads},i} \left(1 - \sum_j \theta_j \right) a_i \exp \left(-\beta \sum_j A_{ij} \theta_j \right) \quad [48]$$

where $k_{\text{ads},i}$ is an adsorption rate constant, θ_i is a fraction of the surface covered by species i , a_i is the activity of species i in the solution, β is a transfer coefficient, and A_{ij} is a surface interaction coefficient between species i and j . The first term in parentheses on the right-hand side of eqn [48] represents the available surface, and the second term represents the effect of pairwise interactions between adsorbed species. The rate of desorption is given by

$$v_{\text{des},i} = k_{\text{des},i} \theta_i \exp \left((1 - \beta) \sum_j A_{ij} \theta_j \right) \quad [49]$$

where $k_{\text{des},i}$ is the desorption rate constant. Combination of eqns [48] and [49] yields the Frumkin isotherm, that is

$$K_{\text{ads},i} a_i = \frac{k_{\text{ads},i}}{k_{\text{des},i}} a_i = \frac{\theta_i}{1 - \sum_j \theta_j} \exp \left(\sum_j A_{ij} \theta_j \right) \quad [50]$$

where $K_{\text{ads},i}$ is an adsorption equilibrium constant. Equation [50] can be simplified if it is assumed that the species are independently adsorbed. Then, the interactions between the species become zero, and eqn [50] takes the form of the well-known Langmuir isotherm:

$$K_{\text{ads},i}a_i = \frac{\theta_i}{1 - \sum_j \theta_j} \quad [51]$$

The Langmuir isotherm is extensively used in electrochemical kinetics. The Frumkin isotherm has been used in some studies when more accurate modeling of adsorption is warranted by experimental data, for example, in the case of corrosion in very concentrated brines (Anderko and Young¹⁰⁸).

It should be noted that detailed modeling of adsorption requires taking into account the effect of potential on adsorption. Equations [50] and [51] are strictly valid only when adsorption is not significantly influenced by metal dissolution. An approach to include the effect of dissolution and, hence, potential on adsorption has been developed by Heusler and Cartledge¹⁰⁹ who proposed an additional process in which a metal atom from an uncovered area ($1 - \sum_j \theta_j$) reacts with an adsorbed ion from the covered area θ_i to dissolve as ferrous ion. The adsorbed ion is then postulated to leave the surface during the reaction, thus contributing to the desorption process. Accordingly, eqn [49] is rewritten by adding an additional term, that is

$$v_{\text{des},i} = k_{\text{d},i}\theta_i \exp\left((1 - \beta) \sum_j A_{ij}\theta_j\right) + i_{\text{des},i} \quad [52]$$

where the desorption current $i_{\text{des},i}$ is given by

$$i_{\text{des},i} = k_{\text{r},i}\theta_i \left(1 - \sum_j \theta_j\right) a_X \exp\left(\frac{\beta FE}{RT}\right) \quad [53]$$

where a_X is the activity of possible additional species (e.g., OH^-) that participate in the dissolution. In eqn [53], the desorption current is potential-dependent because it involves the dissolution of the metal. Equation [53] can be combined with eqns [48] and [52] to form a system of n equations for a solution with n adsorbable species. This system can be solved numerically for the coverage fractions θ_i of each adsorbed species. Because of the potential dependence, the model predicts that the adsorption coverage rapidly decreases above a certain potential range.

It should be noted that a detailed treatment of adsorption is not always necessary for modeling aqueous corrosion. In particular, the potential dependence of adsorption can be often neglected. In most cases, simplified approaches are warranted. Specifically, for low surface coverage, the fraction θ_i can be assumed to be proportional to the activity of the species i as shown by eqn [51]. Thus, eqns [43] and

[44] can often be simplified by using activities of species rather than their surface coverages.

2.38.3.3 Partial Electrochemical Reactions

The behavior of a corroding system results from the interplay of at least two and, frequently, many partial electrochemical reactions. Such reactions include:

1. anodic dissolution of pure metals and alloys in both the active and passive state;
2. reduction of protons, which is usually the primary cathodic reaction in acid corrosion;
3. reduction of water molecules, which is frequently the main cathodic reaction in deaerated neutral and alkaline solutions;
4. reduction of dissolved species that can act as proton donors such as undissociated carboxylic acids, carbonic acid, hydrogen sulfide, and numerous ions that contain protons (e.g., bicarbonates, bisulfides, etc.);
5. reduction of oxygen, which is a common cathodic process in aerated solutions;
6. reduction of metal ions at high oxidation states such as Fe(III) or Cu(II), which can be reduced to a lower oxidation state;
7. reduction of oxyanions such as nitrites, nitrates, or hypochlorites in which a nonmetallic element is reduced to a lower oxidation state;
8. oxidation of water to oxygen, which occurs at high potentials and, therefore, is rarely important in freely corroding systems; and
9. oxidation of metals to higher oxidation states, for example, Cr(III) to Cr(VI), which may occur in the transpassive dissolution region of stainless steels and nickel base alloys.

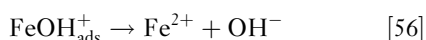
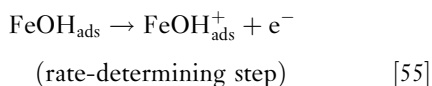
In this section, we present illustrative examples of how these reactions can be modeled in practice.

2.38.3.3.1 Anodic reactions

The dissolution of several pure metals such as iron, copper, or nickel has been extensively investigated. Thus, it is possible to construct practical equations for the partial anodic dissolution processes on the basis of mechanistic information. For most alloys, detailed mechanistic information is not available and, therefore, it is necessary to establish kinetic expressions on a more empirical basis.

For iron dissolution, various multistep reaction mechanisms have been proposed. They have been reviewed in detail by Lorenz and Heusler,¹¹⁰ Drazic,¹¹¹ and Keddarn.¹¹² From the point of view of

modeling, particularly important parameters are the electrochemical transfer coefficient and reaction orders with respect to the ions that participate in anodic dissolution. Although there are substantial differences between the various proposed mechanisms, the dependence of the iron dissolution rate in acidic solutions on the activity of hydroxide ions is generally accepted. The mechanism proposed by Bockris *et al.*,¹¹³ that is



predicts that the reaction order with respect to the OH^- ion is one because of the intermediate step of OH^- adsorption. The validity of this prediction has been verified for acidic solutions. Other mechanisms yield reaction orders between one and two. Additionally, the current density for iron dissolution has been found to depend on the activity of water (Smart and Bockris¹¹⁴). The mechanism of Bockris *et al.*¹¹³ also predicts that the anodic transfer coefficient is $\alpha_{\text{Fe}} = 1.5$, which is consistent with experimentally observed Tafel slopes of 30–40 mV. Thus, the current density for Fe dissolution in acidic solutions can be expressed as

$$i_{\text{Fe,OH}} = i_{\text{Fe,OH}}^* a_{\text{OH}} a_{\text{H}_2\text{O}}^c \exp\left(\frac{\alpha_{\text{Fe}} F(E - E_{0,\text{Fe}})}{RT}\right) \quad [57]$$

where $i_{\text{Fe,OH}}^*$ is a temperature-dependent coefficient, the subscript Fe,OH indicates that the dissolution reaction is mediated by OH^- ions, and c is an empirically determined reaction order with respect to the activity of water. According to Smart and Bockris¹¹⁴ $c = 1.6$. The effect of the activity of water on the current density becomes significant for concentrated solutions, for which the activity of water is usually significantly lower than 1.

Although the reaction order with respect to the OH^- ions is valid for acidic solutions, it has been found that iron dissolution proceeds with little influence of pH for solutions with pH above ~ 4 . Bockris *et al.*¹¹³ explained this phenomenon by assuming a certain nonzero reaction order with respect to Fe^{2+} and by considering the hydrolysis of the Fe^{2+} ions that result from the dissolution. Alternatively, the change in the reaction order with respect to OH^- ions can be reproduced by assuming that the exchange current density is proportional to the surface coverage

by OH^- ions. This assumption is consistent with the reaction mechanism (see eqns [54]–[56]). Thus, eqn [57] can be generalized as¹⁰⁸:

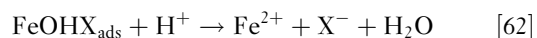
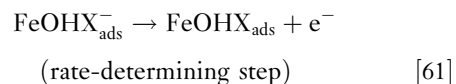
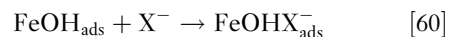
$$i_{\text{Fe,OH}} = i_{\text{Fe,OH}}^* \theta_{\text{OH}} a_{\text{H}_2\text{O}}^c \exp\left(\frac{\alpha_{\text{Fe}} F(E - E_{0,\text{Fe}})}{RT}\right) \quad [58]$$

Assuming that θ_{OH} follows the Langmuir adsorption model, eqn [58] can be rewritten as

$$i_{\text{Fe,OH}} = i_{\text{Fe,OH}}^* \frac{a_{\text{OH}}}{1 + K_{\text{OH}} a_{\text{OH}}} a_{\text{H}_2\text{O}}^c \exp\left(\frac{\alpha_{\text{Fe}} F(E - E_{0,\text{Fe}})}{RT}\right) \quad [59]$$

Equation [59] reduces to eqn [57] for low activities of OH^- , that is, for acidic solutions. For higher concentrations of hydroxide ions, the reaction order with respect to OH^- becomes zero. This is consistent with the lack of a dependence of the Fe oxidation reaction on pH in CO_2 corrosion of mild steel, which occurs at pH values above ~ 4 (Nešić *et al.*,¹¹⁵ Nordsveen *et al.*¹¹⁶).

The effect of halide ions on the dissolution of iron and carbon steel is of particular interest. Adsorbed halide ions may accelerate the anodic dissolution, especially in concentrated halide solutions. A number of reaction mechanisms have been proposed to explain this phenomenon. In particular, Chin and Nobe¹¹⁷ and Kuo and Nobe¹¹⁸ developed a mechanism that postulates a reaction route that is parallel to eqns [52]–[54]. An essentially identical mechanism has also been proposed by Drazic and Drazic.¹¹⁹ According to this mechanism, a halide-containing surface complex is responsible for the dissolution. Thus, eqn [54] is followed by the following parallel route:



The mechanism eqns [60]–[62] results in a dissolution current density that depends on the activities of both halide and hydroxide ions. In acidic solutions, an equation analogous to eqn [57] can be written as

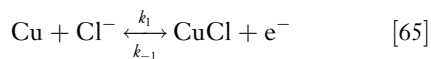
$$i_{\text{Fe,X}} = i_{\text{Fe,X}}^* a_{\text{X}^-}^s a_{\text{OH}^-}^t \exp\left(\frac{\alpha_{\text{Fe}} F(E - E_{0,\text{Fe}})}{RT}\right) \quad [63]$$

where the subscript X indicates the halide ions that mediate the reaction. For chloride systems, $s = 0.4$ and $t = 0.6$ when concentrations are used instead of

activities.¹¹⁸ Since the mechanism described by eqns [60]–[62] is assumed to be parallel to the mechanism under halide-free conditions, the total current density of anodic dissolution can be assumed to be a sum of the contributions of two mechanisms. Also, eqn [63] can be generalized to neutral solutions in analogy with eqn [59]. Additionally, the desorption current density (eqn [53]) contributes to the total current, although it becomes important only at relatively high potentials, and its numerical significance is usually limited. Thus, the expression for the total active Fe dissolution current in halide solutions becomes¹⁰⁸

$$i_{\text{Fe}} = i_{\text{Fe,OH}} + i_{\text{Fe,X}} + i_{\text{des,i}} \quad [64]$$

As with iron, anodic dissolution of copper has also been extensively investigated. Kear *et al.*¹²⁰ reviewed the mechanisms and associated expressions for the current density of anodic dissolution of copper in the active state in chloride environments. Copper dissolution is generally thought to proceed through the formation of cuprous chloride complexes and to be under mixed, charge-transfer and transport, control close to the corrosion potential. Several authors (Lee and Nobe,¹²¹ Deslouis *et al.*,¹²² King *et al.*¹²³) assumed the following mechanism:



The expression for the anodic current density derived from eqns [65] and [66] is

$$\frac{i_{\text{Cu}}}{nF} = \frac{k_1 k_2}{k_{-1}} a_{\text{Cl}}^2 \exp\left(\frac{F(E - E_{0,\text{Cu}})}{RT}\right) - k_{-2} a_{\text{CuCl}_2^-} \quad [67]$$

Since the reaction rate depends on the activity of the reaction products (CuCl_2^-) at the surface (see the second term on the right-hand side of eqn [67]), the reaction is partially controlled by the mass transport of the CuCl_2^- ions, and the anodic current density is simultaneously equal to

$$\frac{i_{\text{Cu}}}{nF} = D_{\text{CuCl}_2^-} \frac{a_{\text{CuCl}_2^-}}{\delta_{\text{CuCl}_2^-}} \quad [68]$$

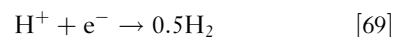
Equation [68] is a special case of eqn [39] when the bulk concentration of CuCl_2^- is negligible.

Much less mechanistic information is available for the anodic dissolution of alloys in the active state. In the case of stainless steels and nickel-base alloys, this is due to the fact that dissolution of these metals in

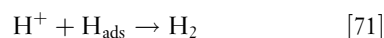
the passive state is more important than in the active state. For these alloys, active dissolution is of importance only in acidic solutions. In this case, expressions for anodic dissolution need to be established on an empirical basis. For stainless steels and nickel-base alloys, a positive reaction order between one and two with respect to hydroxide ions is observed. While such values are similar to those observed for Fe, the exchange current densities are very different and need to be determined separately for individual alloys.

2.38.3.3.2 Cathodic reactions

Among the numerous possible partial cathodic processes, the reduction of protons, water molecules, and dissolved oxygen is ubiquitous in aqueous corrosion. Reduction of protons is an important cathodic process in acidic solutions. The overall reaction is given by

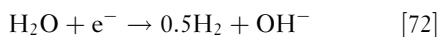


The mechanisms of this reaction have been reviewed by Vetter⁹⁸ and Kaesche.¹⁰⁰ Proton reduction proceeds in two steps according to two alternative mechanisms. The Volmer–Heyrovsky mechanism applies to most metals, whereas the Volmer–Tafel mechanism may be observed on certain noble metals. The Volmer–Heyrovsky mechanism can be represented as a sequence of two elementary reactions, that is



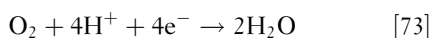
It is generally accepted that the H^+ reduction reaction may proceed under activation or mass transfer control. The cathodic process of H^+ reduction can be modeled assuming that the reaction order with respect to the protons is equal to one. Then, eqns [41] and [42] can be directly used for modeling. In addition to its dependence on the activity of protons, there is empirical evidence that the H^+ reduction depends on the activity of water. According to Smart *et al.*,¹²⁴ the reaction order with respect to water activity is 2.2 on iron. The electrochemical transfer coefficient can be assumed to be equal to ~ 0.5 for carbon steels and many corrosion-resistant alloys, which corresponds to a Tafel slope of 118 mV at 25 °C.

As the pH of a solution increases, the importance of the proton reduction reaction rapidly decreases. In neutral and alkaline solutions, the reduction of water molecules becomes predominant unless stronger oxidizing agents (e.g., oxygen) are present in the system. The water reduction is given by

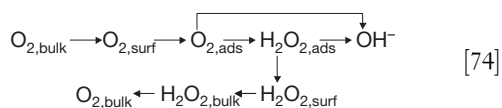


and is thermodynamically equivalent to the reduction of protons. However, its kinetic characteristics are different. Unlike the reduction of protons, the water reduction reaction typically does not exhibit a limiting current density because there are no diffusion limitations for the transport of H_2O molecules to the surface. This remains true as long as the system is predominantly aqueous. The water reduction process can be modeled by assuming the same reaction order with respect to H_2O as that for proton reduction. Also, practically the same value of the electrochemical transfer coefficient can be assumed.

Reduction of oxygen, that is



is the predominant cathodic reaction in aerated aqueous solutions unless the solution contains stronger oxidizing agents such as ferric, cupric, or hypochlorite ions. The mechanism of oxygen reduction is substantially more complex than the mechanisms of H^+ or H_2O reduction. Oxygen reduction on iron and carbon steel has been reviewed by Jovancicevic and Bockris,¹²⁵ Zecevic *et al.*,¹²⁶ and Jovancicevic.¹²⁷ On stainless steels, it has been analyzed by Le Bozec *et al.*,¹²⁸ Kapusta,¹²⁹ and in papers cited therein. On copper, it has been studied by King *et al.*¹³⁰ In general, it has been established that the reaction may proceed either through a four-electron pathway, which leads to the reduction of O_2 to H_2O , or through a two-electron pathway, which leads to the formation of H_2O_2 as an intermediate. An overall reaction scheme may be represented as



where the subscripts 'surf' and 'ads' denote the oxygen in the diffusion layer close to the surface and oxygen adsorbed on the surface, respectively. The absorbed intermediate H_2O_2 can be either further reduced to OH^- or desorbed and dissolved in the solution or converted back to oxygen through decomposition or reoxidation. The actual reaction pathway is influenced by many factors such as the surface treatment of the electrode.¹²⁸ However, the four-electron reduction path from O_2 to OH^- seems to predominate.¹²⁹ Oxygen reduction may be under charge transfer or mass transfer control, due to the diffusion of dissolved oxygen molecules. For passive metals, the process is usually under charge transfer control because the limiting

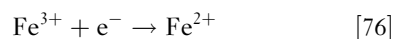
current density for oxygen reduction is usually greater than the passive current density at typical dissolved oxygen concentrations.

For modeling purposes, the key parameters are the electrochemical transfer coefficient and the reaction orders with respect to dissolved oxygen and protons. These parameters determine the dependence of the reduction reaction on dissolved oxygen concentration (or, equivalently, the partial pressure of oxygen) and on pH. Once these parameters are known, the oxygen reduction process can be modeled on a semi-empirical basis. The current density for oxygen reduction can be written as:

$$i_{\text{O}_2} = i_{\text{O}_2}^* a_{\text{O}_2,s}^q a_{\text{H}^+,s}^r \exp\left[\frac{-\alpha_{\text{O}_2} F(E - E_{0,\text{O}_2})}{RT}\right] \quad [75]$$

Equation [75] needs to be coupled with eqn [37] with $n=4$ for mass-transfer limitations. The reaction orders q and r in eqn [75] are, in general, specific to the metal surface although they are expected to be similar within families of alloys. For stainless steels, there seems to be a consensus that the reaction order with respect to dissolved oxygen is 0.5 (Kapusta,¹²⁹ Sridhar *et al.*¹³¹), whereas the order with respect to protons ranges from 0.5 to 1 (or, equivalently, the order with respect to hydroxide ions varies from -0.5 to -1). For passive iron or carbon steel, the reaction order with respect to O_2 has been reported as 0.5 (Calvo and Schiffrin¹³²) or 1 (Jovancicevic and Bockris,¹²⁵ Jovancicevic¹²⁷). For copper, a value of 1 has been reported (King *et al.*¹³⁰).

Another important cathodic reaction is the reduction of transition metal ions such as Fe^{3+} and Cu^{2+} to lower oxidation states, for example



This process can be modeled as a first-order reaction with respect to the activity of ferric ions by taking into account the mass transport limitations (eqn [37]).

All the cathodic reactions discussed above may proceed under mass transfer limitations due to the diffusion of reactants to the corroding surface. However, cathodic limiting current densities may also arise because of limitations due to homogeneous reactions in the solution. A prominent example of such a reaction is the reduction of carbonic acid, which is the key cathodic process in CO_2 corrosion of carbon steel. This reaction accounts for the substantially higher corrosivity of CO_2 solutions than mineral acid solutions at the same pH. Carbonic acid results from the hydration of dissolved CO_2 , that is



Reaction eqn [77] is followed by the reduction of H_2CO_3 on the surface, that is



which is thermodynamically equivalent to the reduction of protons, but is characterized by different kinetics. The H_2CO_3 reduction is under activation or chemical reaction control, and can be modeled using eqn [41]. The charge transfer current is expressed as (Nešić *et al.*¹¹⁵):

$$i_{\text{H}_2\text{CO}_3} = i_{\text{H}_2\text{CO}_3}^* a_{\text{H}_2\text{CO}_3} a_{\text{H}^+}^{-0.5} \exp\left[\frac{-\alpha_{\text{H}_2\text{CO}_3} F(E - E_{0,\text{H}})}{RT}\right] \quad [79]$$

where the transfer coefficient can be assumed to be equal to that for H_2O reduction. The limiting current density can be calculated from an equation developed by Nešić *et al.*¹¹⁵ on the basis of a formula derived by Vetter⁹⁸ for processes with a rate-determining homogeneous reaction in the solution. Here, the rate-determining reaction is the hydration of CO_2 and the limiting current density is:

$$i_{\text{H}_2\text{CO}_3,\text{L}} = Fa_{\text{H}_2\text{CO}_3} \left(D_{\text{H}_2\text{CO}_3} K_{\text{H}_2\text{CO}_3} k_{\text{H}_2\text{CO}_3}^f \right)^{1/2} \quad [80]$$

where $D_{\text{H}_2\text{CO}_3}$, $K_{\text{H}_2\text{CO}_3}$, and $k_{\text{H}_2\text{CO}_3}^f$ are the diffusion coefficient of H_2CO_3 , equilibrium constant for the hydration of CO_2 , and forward reaction constant for the hydration reaction, respectively.

2.38.3.3.3 Temperature dependence

The rates of the majority of partial anodic and cathodic processes are strongly dependent on temperature. This temperature dependence can be modeled by assuming that the concentration-independent part of the exchange current density (here denoted by i^*) is expressed as

$$i^*(T) = i^*(T_{\text{ref}}) \exp\left[-\frac{\Delta H^\ddagger}{R} \left(\frac{1}{T} - \frac{1}{T_{\text{ref}}}\right)\right] \quad [81]$$

Equation [81] is equivalent to assuming a constant enthalpy of activation ΔH^\ddagger for each partial process.

2.38.3.4 Modeling Mass Transport Using Mass Transfer Coefficients

To calculate the mass-transport effects on electrochemical kinetics according to eqns [37]–[40], it is necessary to predict the diffusion layer thickness δ_i

or, equivalently, the limiting current density. Theoretical formulas for these quantities cannot be obtained for arbitrary flow conditions and, therefore, empirical approaches are necessary for most practical applications.

In the case of a rotating disk electrode, a theoretical solution has been derived by Levich.¹³³ It is noteworthy that Levich's solution preceded experimental results. The thickness of the diffusion layer on a rotating disk electrode is

$$\delta_i = 1.61 D_i^{1/3} \nu^{1/6} \omega^{-1/2} \quad [82]$$

where D_i is the diffusion coefficient of the reacting species, ω is the rotation rate, and ν is the kinematic viscosity, which is the ratio of the dynamic viscosity and density, that is

$$\nu = \eta/\rho \quad [83]$$

In view of the relationships between the thickness of the diffusion layer and the limiting current density (eqns [38] and [40]), a physically equivalent predictive expression can be written for the limiting current density. For example, the limiting current density of a cathodic reaction (eqn [38]) then becomes:

$$i_{\text{c,L}} = -0.6205 n F c_{0,\text{b}} D_o^{2/3} \nu^{-1/6} \omega^{1/2} \quad [84]$$

For many other flow geometries, mass transport can be calculated using empirical correlations expressed in terms of the mass transfer coefficient k_m . In general, the mass transfer coefficient is defined as

$$k_m = \frac{\text{Reaction rate}}{\text{Concentration driving force}} \quad [85]$$

For an electrochemical reaction, the reaction rate is expressed using the current density, and eqn [36] for a mass transport-limited reaction can be rewritten in terms of the mass transfer coefficient k_m as

$$\mathcal{F}_i = \frac{i_i}{n_i F} = -D_i \frac{c_{i,\text{b}} - c_{i,\text{s}}}{\delta_i} = -k_{m,i} (c_{i,\text{b}} - c_{i,\text{s}}) \quad [86]$$

This indicates a relationship between δ_i and $k_{m,i}$ that is

$$k_{m,i} = \frac{D_i}{\delta_i} \quad [87]$$

Mass transport rates can be expressed using dimensionless groups, for which empirical correlations can be developed for a number of flow patterns. The mass transfer coefficient k_m enters into the Sherwood number Sh , which is defined as

$$Sh = \frac{k_m d}{D} \quad [88]$$

where d is a characteristic dimension (e.g., a pipe or rotating disk diameter); D , a diffusion coefficient; and the subscript i has been dropped for convenience as it is understood that eqn [88] is written for individual reacting species. The Sherwood number can be correlated with the Reynolds (Re) and Schmidt (Sc) numbers, which are defined as

$$Re = \frac{Vd}{\nu} \quad [89]$$

$$Sc = \frac{\nu}{D} \quad [90]$$

where V is the linear velocity. It can be shown by dimensional analysis that Sb is a function of Re and Sc . This function typically has the form^{134,135}

$$Sb = \text{Const} \times Re^x \times Sc^y \quad [91]$$

where x is usually between 0.3 and 1 and y is about 1/3. For example, the theoretically derived results for the rotating disk can be recast in terms of the mass transfer coefficient as

$$Sb = 0.6205 Re^{0.5} Sc^{0.33} \quad [92]$$

Empirical expressions for other flow geometries have been reviewed by Poulson^{134,135} for single-phase flow conditions. Equations of the type eqn [91] exist for the rotating cylinder, impinging jet, nozzle or orifice, and pipe flow. For the rotating cylinder, the correlation of Eisenberg *et al.*¹³⁶ is widely used

$$Sb = 0.0791 Re^{0.70} Sc^{0.356} \quad [93]$$

For single-phase flow in a straight pipe, several correlations have been developed. Among these equations, Berger and Hau's¹³⁷ correlation has found use in a number of corrosion modeling studies:

$$Sb = 0.0165 Re^{0.86} Sc^{0.33} \quad [94]$$

The earlier pipe flow formulas have been reviewed by Poulson,¹³⁴ and the use of more recent equations has been discussed by Lin *et al.*¹³⁸ Equations of this kind are not as well developed for multiphase flow. Correlations are available for stratified flow (Wang and Nešić¹³⁹), but a comprehensive treatment is not available for various regimes of multiphase flow. Therefore, a convenient alternative is to base the computation of mass transfer coefficients on the well-known analogy between heat and mass transfer.

The analogies between the transport of mass, momentum, and heat can be understood by considering the similarity between their respective mathematical formulations, namely, Fick's law of diffusion, Newton's law of viscosity, and Fourier's law of heat conduction.

Thus, once a relationship has been established for a given phenomenon in terms of dimensionless numbers, it can further serve for the calculation of another phenomenon that takes place under the same geometric and physical conditions but with different velocities, dimensions, and physical properties of the system. In particular, the correlations established for heat transfer can be used for mass transfer calculations. The analogy between the heat, mass, and momentum transfer has been stated in a dimensionless form by Chilton and Colburn¹⁴⁰ as

$$\frac{Sb}{Re Sc^{1/3}} = \frac{Nu}{Re Pr^{1/3}} = \frac{f}{2} \quad [95]$$

where the Nusselt number, Nu , and the Prandtl number, Pr , are the heat transfer equivalents of the Sherwood and Schmidt numbers in mass transfer, respectively, and f is a friction factor. Correlations for the friction factor are available as a function of pipe roughness, its diameter, and the Reynolds number (Frank¹⁴¹). The exponent 1/3 in eqn [95] can be replaced with a generalized exponent n . The Nusselt and Prandtl numbers are defined as

$$Nu = \frac{bd}{\lambda} \quad [96]$$

$$Pr = \frac{\nu}{\alpha} \quad [97]$$

where b is the convection heat transfer coefficient; λ , the thermal conductivity; and α , the thermal diffusivity ($\alpha = \lambda/\rho C_p$).

This relationship makes it possible to determine the mass transfer coefficient in two-phase flow systems for which experimental heat transfer correlations are available. Heat transfer correlations take the form

$$Nu = \text{Const} \times Re^x Pr^y \quad [98]$$

They have been reviewed by Kim *et al.*¹⁴² and Adsani *et al.*^{143,144} for annular, slug, and bubbly flow in horizontal and vertical tubes. Also, Adsani *et al.*^{143,144} developed a correlation for calculating the two-phase Nusselt number, which is a generalization of the Chilton-Colburn¹⁴⁰ heat transfer expression (i.e., the second equality of eqn [95]):

$$Nu_{\text{two-phase}} = C_1 f_L^{C_2} \left(\frac{V_L d}{\nu} \right)^{C_3} Pr_L^{1/3} \quad [99]$$

where the liquid-phase friction factor f_L and velocity V_L are calculated using flow models for annular, slug, and bubbly flow, and C_1 , C_2 , and C_3 are fitting constants. Subsequently, the Sherwood number and the

mass transfer coefficient can be obtained from the first equality in eqn [95].

As shown in the above equations, the computation of the mass transfer coefficient requires the diffusion coefficients, viscosity, and density. Density is a thermodynamic property and, as such, can be calculated from any comprehensive thermodynamic model for electrolyte systems. For example, Wang *et al.*⁵⁴ describe how to calculate densities in a way that is consistent with other thermodynamic properties. The computation of viscosities and diffusion coefficients requires separate models, which are beyond the scope of this chapter. Viscosity and diffusivity models have been reviewed and critically evaluated by Corti *et al.*¹⁴⁵ with particular emphasis on systems at elevated temperatures.

2.38.3.4.1 Example of electrochemical modeling of general corrosion

To illustrate the application of the principles described earlier, Figure 5 shows the computation of the corrosion rate and potential of type 316 stainless steel in aqueous solutions of HF. These calculations have been made using the model of Anderko *et al.*^{108,146} as implemented in the Corrosion Analyzer software.⁶¹ The upper diagram shows the partial cathodic and anodic processes in a 2 m HF solution. Three cathodic processes are taken into account in this system: reduction of protons (H^+), reduction of undissociated HF molecules, and reduction of water molecules. These partial processes are marked in Figure 5(a) as (1), (2), and (3), respectively. The H^+ reduction reaction is modeled using eqns [41] and [42] as described earlier. The HF reduction process is calculated using the same equations, but with a different exchange current density. Both the H^+ and HF reduction processes show partial current densities because of mass transport limitations for the transport of H^+ and HF to the surface. Because of the low degree of dissociation of HF, the reduction of HF (line two in Figure 5(a)) plays a much more important role than the reduction of H^+ ions (line 1). The partial anodic curve for the oxidation of 316 SS is labeled as (4). It is assumed that the alloy components dissolve congruently, and the dependence of the partial anodic current density on the acidity of the solution is analogous to that observed for Fe (see eqn [59]), but with a different exchange current density. The superposition of the partial cathodic and anodic processes yields a predicted polarization curve, which is shown by a thick line in Figure 5(a). The location of the mixed potential is calculated

according to eqn [45] with $A_a = A_c$ and marked with a triangle. The complete model reproduces the experimental corrosion rates (Figure 5(b)) and corrosion potentials (Figure 5(c)) as a function of HF concentration and temperature.

2.38.3.5 Detailed Modeling of Mass Transport

The treatment of mass transport by the use of mass transfer coefficients is computationally efficient and is capable of reproducing steady-state corrosion behavior with good accuracy. However, it is subject to some limitations including:

1. it is suitable for calculating only steady-state behavior and, therefore, it is not appropriate for modeling time-dependent corrosion,
2. it neglects migration which introduces errors especially for dilute systems without a background electrolyte, and
3. it is not convenient for modeling transport in systems with geometrical constraints, especially when the cathodic and anodic areas are spatially separated; thus, it is not well suited for modeling the propagation of localized corrosion.

These limitations can be eliminated by a more comprehensive (but much more computationally demanding) treatment of transport phenomena. This treatment is based on the conservation laws for each species in the solution (Newman¹⁵⁰):

$$\frac{\partial c_k}{\partial t} = -\nabla \mathcal{J}_k + R_k \quad k = 1, \dots, K \quad [100]$$

where C_k is the concentration of species k , t is the time, \mathcal{J}_k is the flux of species k , ∇ is the vector differential operator (which reduces to $\partial/\partial x$ in a one-dimensional case), and R_k is the rate of production (source) or depletion (sink) of this species as a result of chemical reactions. In the vast majority of practical applications, the dilute solution theory is used to calculate the flux of the species, that is

$$\mathcal{J}_k = -D_k \nabla c_k - z_k F u_k c_k \nabla \varphi + c_k v \quad [101]$$

where u_k is the mobility of species k , φ is the electrostatic potential in the solution, v is the fluid velocity, and the other symbols were defined previously. In eqn [101], the first term on the right-hand side represents the contributions of diffusion, the second term describes migration, and the third term is a contribution of convection. In the migration term, the mobility can be calculated from the diffusivity using the Nernst–Einstein equation:

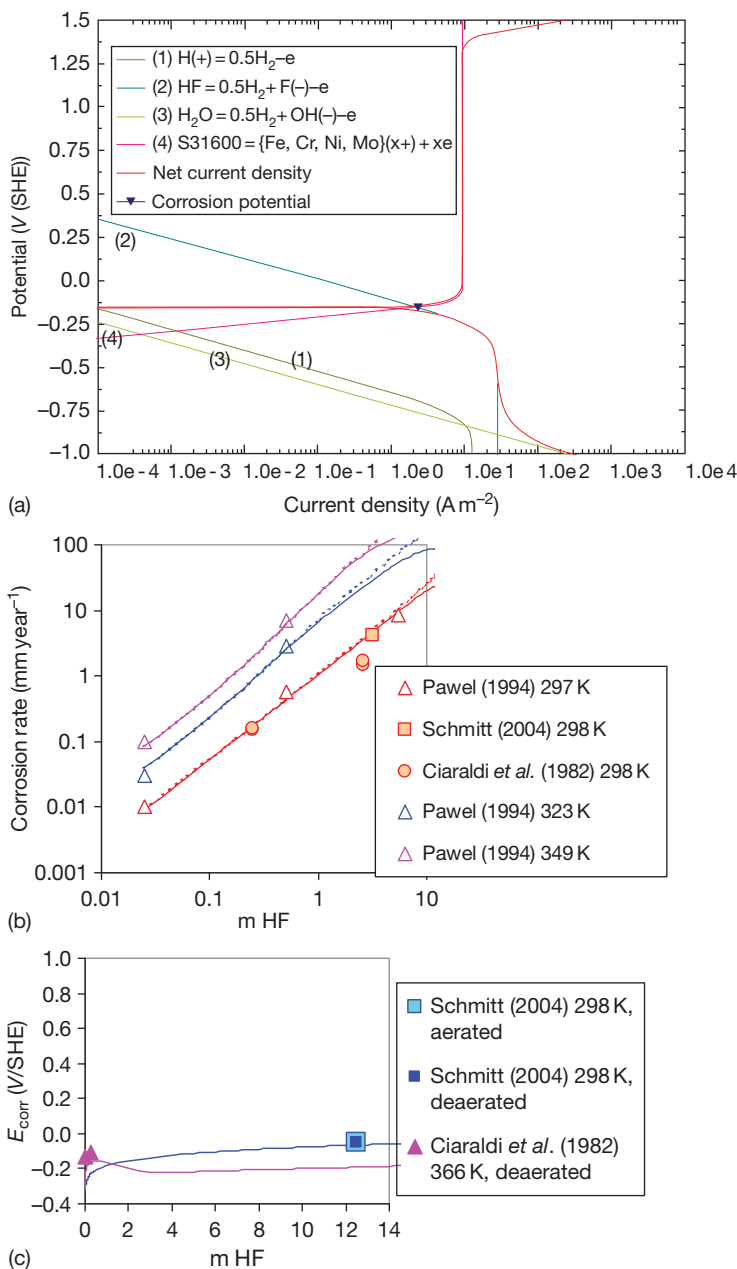


Figure 5 Application of an electrochemical model of general corrosion^{108,146} to type 316L stainless steel in aqueous HF solutions. The upper diagram (a) shows the partial cathodic and anodic processes in a 2 m HF solution. The middle (b) and lower (c) diagrams compare the calculated and experimental¹⁴⁷⁻¹⁴⁹ corrosion rates and potentials, respectively.

$$u_k = \frac{D_k}{RT} \quad [102]$$

$$\nabla^2 \varphi = -\frac{F}{\varepsilon} \sum_k z_k c_k \quad [103]$$

which is exact for species at infinite dilution and provides a good approximation at finite concentrations. An additional condition for determining the potential in eqn [101] is given by the Poisson equation:

where ε is the dielectric permittivity of the solution. It can be shown¹⁵⁰ that, due to the large value of the ratio F/ε , even a very small separation of charges (i.e., $\sum z_k c_k \neq 0$) results in a large potential gradient,

which in turn prevents any appreciable separation of charge. Therefore, eqn [103] is very often replaced in practice by the simple electroneutrality condition, that is

$$\sum z_k c_k = 0 \quad [104]$$

which is one of the basic equations for computing equilibrium properties of electrolytes.

It should be noted that eqn [101] is rigorous only for dilute solutions. For concentrated solutions, its more general counterpart is¹⁵⁰

$$\mathcal{F}_k = c_k v_k \quad [105]$$

where the velocities v_k of species k are determined by the multicomponent diffusion equations:

$$c_k \nabla \mu_k = RT \sum_j \frac{c_k c_j}{c_{\text{tot}} D_{kj}} (v_j - v_k) \quad [106]$$

where D_{kj} are the mutual diffusion coefficients, and c_{tot} is the total concentration of all components. The application of eqns [105] and [106] is very difficult due to the lack of a general methodology for computing D_{kj} and computational complexity. Therefore, eqns [105] and [106] have found few applications in practical models. However, a practical simplified form can be obtained for moderately dilute solutions for which the concentrations of solute species are smaller than the concentration of the solvent. Then, eqns [105] and [106] simplify to

$$\mathcal{F}_k = -\frac{D_k}{RT} c_k \nabla \mu_k + c_k v \quad [107]$$

Considering that $\mu_k = \mu_k^0 + RT \ln c_k \gamma_k + z_k F \varphi$, the flux equation becomes¹⁵⁰

$$\mathcal{F}_k = -D_k \nabla c_k - z_k F u_k c_k \nabla \varphi + c_k v - D_k c_k \nabla \ln \gamma_k \quad [108]$$

which is only moderately more complex than the dilute-solution eqn [101], but benefits from the information on solution nonideality that is embedded in the activity coefficient and can be calculated from an electrolyte thermodynamic model.

In the convective term of eqn [101] or [108], the instantaneous fluid velocity (v) can be calculated, in principle, by the methods of computational fluid dynamics. However, such calculations involve a large computational effort and are, in practice, limited with respect to flow geometries and conditions. For turbulent flow, a practical approach relies on introducing turbulent diffusion. Accordingly, instantaneous velocity is divided into steady and turbulent components. The steady component is parallel to the surface and does not contribute to transport to and from the surface. Then, the convection term in eqn [101] or [108],

$c_k v$, is approximated by a turbulent diffusivity term, $-D_t \nabla c_k$, which can be lumped with the molecular diffusion term thus defining an effective diffusion coefficient (Davis,¹⁵¹ Nordsveen *et al.*¹¹⁶)

$$D_k^{\text{eff}} = D_k + D_t \quad [109]$$

where D_t can be obtained from empirical correlations with fluid properties.^{151,152} For example, Davis's¹⁵¹ correlation has been used in the CO₂ corrosion model of Nordsveen *et al.*¹¹⁶:

$$D_t = 0.18 \left(\frac{z}{\delta}\right)^3 \frac{\eta}{\rho} \quad [110]$$

where z represents the distance from the surface (either a metal surface or a surface covered with corrosion products), η is the viscosity, ρ is the density, and δ is the thickness of the laminar boundary layer, which can be calculated for a pipe with a diameter d as

$$\delta = 25 Re^{-7/8} d \quad [111]$$

It is noteworthy that this formalism can be shown to be physically equivalent to the treatment of turbulent flow through mass transfer coefficients as described in the previous section. Specifically, Wang and Nešić¹³⁹ showed a relationship between the mass transfer coefficient and D_t :

$$\frac{1}{k_{m,i}} = \int_0^\delta \frac{dz}{D_i + D_t} \quad [112]$$

The computation of the rates of production or depletion R_k is necessary in order to apply eqn [100]. A general matrix formalism for calculating the R_k terms in a system with multiple reactions has been developed by Nordsveen *et al.*¹¹⁶ The main limitation here is the fact that rate data are available only for a very limited number of reactions such as precipitation of common scales (CaCO₃, FeCO₃) and selected homogeneous reactions (e.g., hydration of H₂CO₃). For the vast majority of reactions, only equilibrium equations are available and, in fact, there is no physical need for kinetic expressions for most homogeneous reactions because they are fast relative to mass transport. Therefore, arbitrary rate expressions may be assumed as long as they are constrained by the equilibrium constant (i.e., the ratio of the forward and reverse rate constants is equal to the equilibrium constant), give appropriately fast reaction rates and change direction as the equilibrium point is crossed. A convenient expression for the production or depletion rate for species k can be defined in terms of the departure of the ionic product from equilibrium (Walton¹⁵³):

$$R_k = \sum_{m=1}^M \left[-r_m v_{km} \ln \left(\frac{\prod c_k^{v_{km}}}{K_m} \right) \right] \quad [113]$$

where r_m is an adjustable numerical rate parameter for reaction m , K_m is the equilibrium constant for reaction m , and v_{km} is the stoichiometric coefficient for species k in the m th reaction. Alternatively, the transport equations can be first solved separately from the chemical effects and, then, at the end of each sufficiently small time step, thermodynamic equilibrium calculations can be performed in each elementary volume.

To solve the system of transport eqns [100] and [101] or [108], boundary conditions are required. In the bulk solution, the equilibrium concentrations are the natural boundary conditions. For each species involved in electrochemical reactions, the flux at the metal surface is determined from

$$\mathcal{F}_k = -\frac{i_k}{n_k F} \quad [114]$$

where the current density i_k is calculated from appropriate expressions for cathodic and anodic partial processes as a function of concentrations at the metal surface. This provides a link to the mechanistic or empirical electrochemical expressions described above. For the species that are not involved in the reactions, the flux at the interface is zero. It should be noted that the application of this formalism of mass transport can become quite computationally involved, especially for systems with numerous species, because it requires solving a system of differential equations (eqns [100] and [101] or [108]) with constraints (eqns [103] or [104] and chemical terms).

2.38.3.5.1 Effect of the presence of porous media

The above transport equations need to be modified when mass transport occurs through porous media such as corrosion products, calcareous deposits, soil or sand, and various man-made environments, including concrete and ceramics. Such a generalization can be formulated in terms of two characteristic quantities, porosity and tortuosity. Porosity (ε) is the volumetric void fraction of the medium, whereas tortuosity (τ) is defined as the ratio of the distance that an ion or molecule travels around solid particles to the direct path. For practical applications, tortuosity can be correlated with porosity thus leaving porosity as the only parameter to affect transport equations. The generalization of transport equations to porous media has been

discussed by Newman¹⁵⁰ and Bear.¹⁵⁴ A detailed corrosion model that includes the transport in porous corrosion products has been developed for CO₂ corrosion by Nordsveen *et al.*¹¹⁶ and Nešić and Lee.¹⁵⁵

2.38.3.6 Active–Passive Transition and Dissolution in the Passive State

The expressions for anodic partial current densities discussed above (eqns [54]–[68]) are limited to the dissolution in the active state. However, dissolution in the passive state and the transition between the active and passive state are equally important for modeling aqueous corrosion. In fact, passivity is the key to our metal-based civilization (Macdonald⁹⁷) and has been extensively investigated since the pioneering work of Faraday and Schönbein in the 1830s. Theories of passivity have been reviewed by many investigators (Frankenthal and Kruger,¹⁵⁶ Froment,¹⁵⁷ Marcus and Oudar,¹⁵⁸ Natishan *et al.*,¹⁵⁹ Macdonald^{97,160}) and are beyond the scope of this chapter. In this section, we focus solely on practical models for calculating the anodic current density in the passive and active–passive transition regions as a function of solution chemistry.

Passivity manifests itself by a sharp drop in the anodic current density at a certain critical potential as the metal is polarized in a negative-to-positive potential direction. For calculation purposes, empirically determined anodic polarization curves can be reproduced using a suitable fitting function. For example, such a function has been developed by Macdonald.¹⁶¹ Then, empirical fitting functions can be used within the framework of the mixed potential theory as described above.

A convenient way to introduce the active–passive transition into a computational model is to consider a current that leads to the formation of a passive layer in addition to the current that leads to active dissolution (Ebersbach *et al.*,¹⁶² Anderko and Young¹⁰⁸). For this purpose, a certain fraction of the surface θ_p can be assumed to be covered by a passive layer. The change of the passive layer coverage fraction with time can be expressed as

$$\left(\frac{\partial \theta_p}{\partial t} \right)_{E, a_i} = c i_{MeO} (1 - \theta_p) - K \theta_p \quad [115]$$

where i_{MeO} is the current density that contributes to the formation of a passive layer. The second term on the right-hand side of eqn [115] represents the rate of dissolution of the passive layer, which is

proportional to the coverage fraction. Solution of this equation in the steady-state limit yields an expression for the anodic dissolution current:

$$i_{\text{Me,TOT}} = \frac{i_{\text{Me}} + i_{\text{MeO}}}{1 + (ci_{\text{MeO}}/K)} = \frac{i_{\text{Me}} + i_{\text{MeO}}}{1 + (i_{\text{MeO}}/i_p)} \quad [116]$$

where i_{Me} is the dissolution current density in the active state and the ratio $i_p = c/K$ constitutes the passive current density. The current i_{Me} is calculated using the active dissolution models described above. The current i_{MeO} is expressed using the usual expression for process under activation control, that is

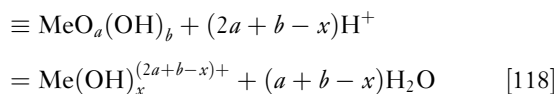
$$i_2 = i_2^0 \exp\left(\frac{\alpha_2 F(E - E_F)}{RT}\right) \quad [117]$$

in which the parameters can be adjusted to reproduce the observable characteristics of the active-passive transition including the critical current density (i_{crit}) and Flade potential (E_F).¹⁴⁶ Equation [116] can be then used for the anodic process of metal dissolution within the framework of the mixed-potential theory (eqns [45] and [46]).

An example of mixed-potential calculations for a passive metal is shown in **Figure 6**. This figure illustrates the computation of the corrosion potential of alloy 600 in a dilute LiOH solution as a function of dissolved oxygen concentration. As in **Figure 5**, the upper and middle diagrams of **Figure 6** show the predicted partial E versus i curves for the anodic and cathodic processes. The upper diagram (**Figure 6(a)**) shows the predictions for a very low O_2 concentration (0.013 ppm), whereas the concentration in the middle diagram is somewhat higher (0.096 ppm). In a weakly alkaline solution, the alloy is passive as indicated by the vertical portion of the anodic curve (line labeled as (3)). Two main cathodic processes are taken into account in this system, that is, the reduction of H_2O (line (1)) and the reduction of O_2 (line (2)). At the lower O_2 concentration, the limiting current density is lower than the passive current density, and the main cathodic process is the reduction of H_2O (i.e., the mixed potential lies at the intersection of the lines (1) and (3) in **Figure 6(a)**). As the O_2 concentration increases, the O_2 reduction reaction becomes predominant and determines the mixed potential, which then lies at the intersection of lines (2) and (3). This behavior explains the experimentally determined s-shaped dependence of E_{corr} on O_2 concentration as shown in **Figure 6(c)**. The s-shape is due to the transition from H_2O reduction to O_2 reduction as the dominant cathodic process. The transition

depends on flow conditions because the O_2 reduction is partially under mass transport control.

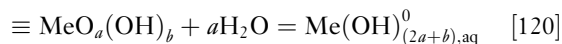
Passive dissolution and active-passive transition strongly depend on solution chemistry. In the absence of specific active ions, the dissolution of oxide films depends primarily on the pH of the solution. Appropriate kinetic expressions can be constructed by considering dissolution reactions between the passive oxide/hydroxide surface layers and solution species (Anderko *et al.*,¹⁴⁶ Sridhar *et al.*^{131,164}) In acidic solutions, the key reaction involves the protons from the solution:



where the symbol '≡' denotes surface species. The corresponding kinetic equation is

$$i_{\text{p,H}^+} = k_{\text{H}^+} a_{\text{H}^+,s}^q \quad [119]$$

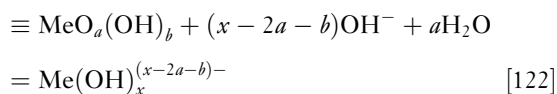
where $a_{\text{H}^+,s}$ denotes the surface concentration of hydrogen ions and q is a reaction order, which is not necessarily related to the stoichiometric coefficient in the dissolution reaction. In neutral solutions, the predominant dissolution reaction can be written as



where the predominant species on the right-hand side of eqn [120] is a neutral complex as indicated by the superscript 0. The corresponding kinetic equation is

$$i_{\text{p,H}_2\text{O}} = k_{\text{H}_2\text{O}} a_{\text{H}_2\text{O},s}^r \quad [121]$$

where the reaction order with respect to water indicates that dissolution may be affected by water activity. Similarly, the predominant reaction in alkaline solutions is



with a corresponding kinetic equation given by

$$i_{\text{p,OH}^-} = k_{\text{OH}^-} a_{\text{OH}^-,s}^c \quad [123]$$

The total passive current density as a function of pH is given by

$$i_p = i_{\text{p,H}^+} + i_{\text{p,H}_2\text{O}} + i_{\text{p,OH}^-} \quad [124]$$

It should be noted that the passive dissolution may be influenced by mass transport. For example, aluminum dissolution in alkaline solutions is known to be partly under mass transport control due to the transport of

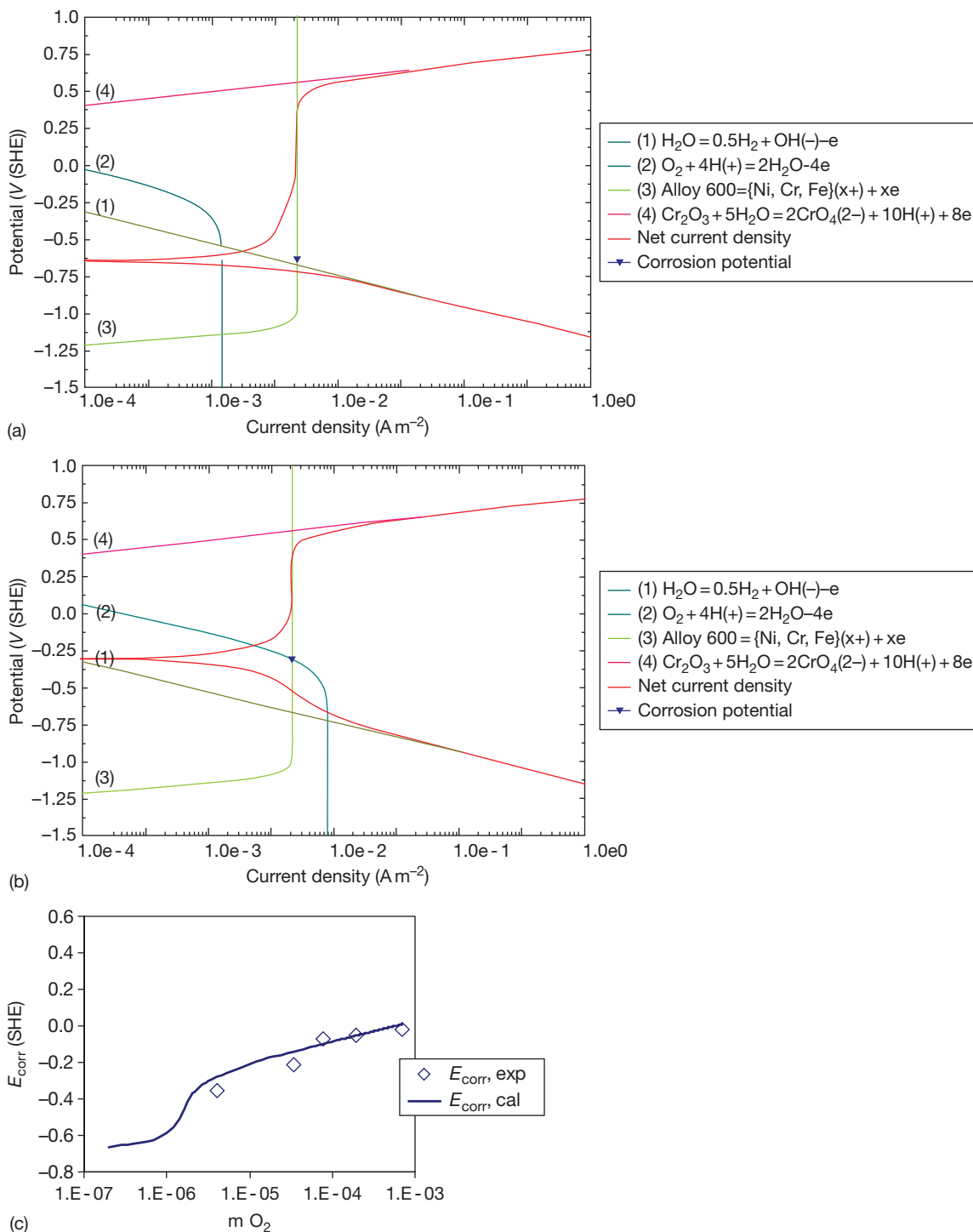


Figure 6 Modeling of the corrosion potential of alloy 600 in a 0.1 M LiOH solution at 200 °C as a function of dissolved oxygen concentration. The upper and middle diagrams (a and b) show the calculated partial electrochemical reactions and predicted polarization curve for solutions containing $4 \times 10^{-7} \text{ m}$ (0.013 ppm) and $3 \times 10^{-6} \text{ m}$ (0.096 ppm) O_2 , respectively. The lower diagram (c) compares the calculated corrosion potential with experimental data¹⁶³ at 200 °C as a function of dissolved oxygen molality.

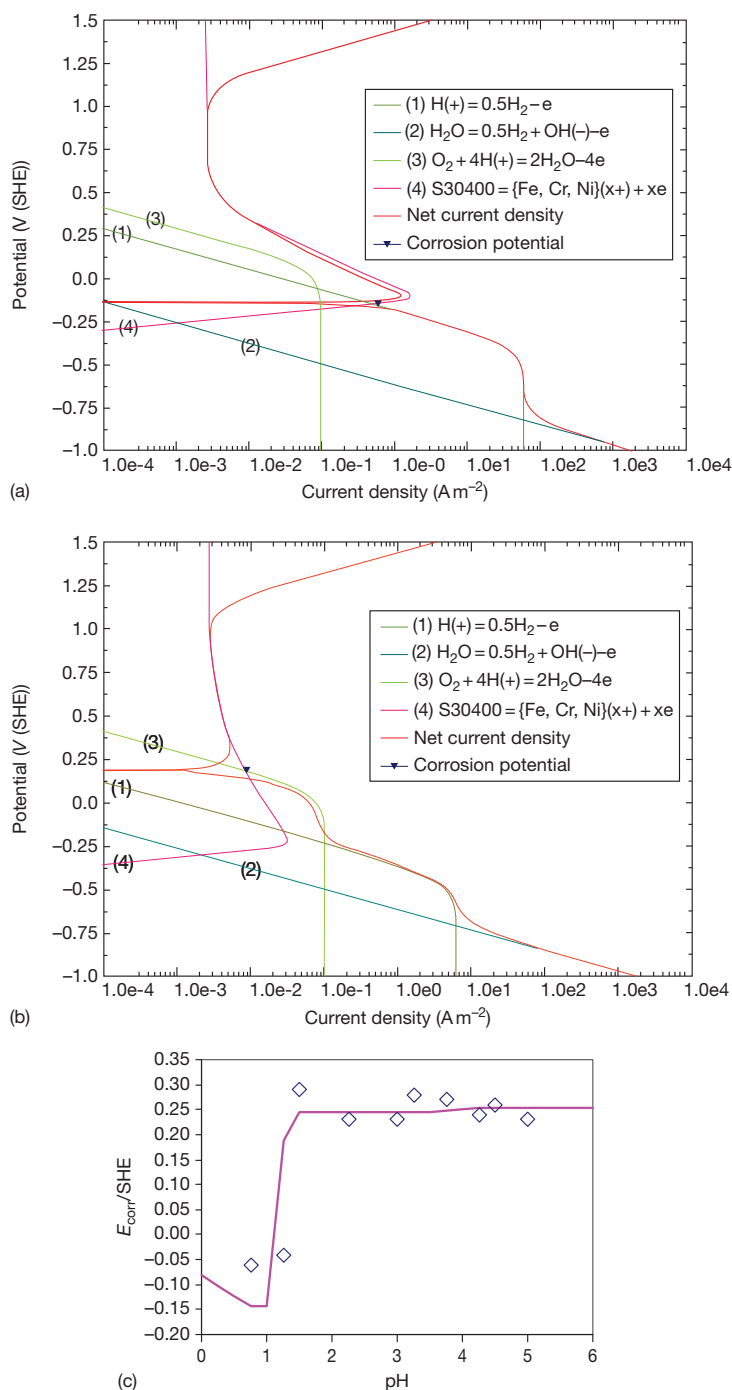


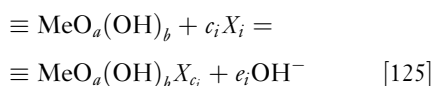
Figure 7 Electrochemical modeling of the depassivation pH and corrosion potential of type 304 stainless steel in aerated 0.1 M Na₂SO₄ + H₂SO₄ solutions. The upper (a) and middle (b) diagrams show the calculated partial electrochemical processes and predicted polarization curve for pH = 0.8 and 1.8, respectively. The lower diagram (c) compares the calculated corrosion potentials with experimental data.¹⁶⁵

OH⁻ ions from the bulk to the interface. Then, the contributions to the passive current density (eqn [124]) should be coupled with mass-transfer equations such as eqn [36].¹³¹

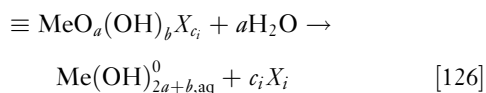
Figure 7 illustrates the electrochemical modeling of the pH dependence of the active-passive transition of type 304 stainless steel. The upper and middle diagrams in **Figure 7** show the partial electrochemical

processes in Na_2SO_4 solutions with $\text{pH}=0.8$ and 1.8 , respectively. The anodic curve (line 4) was modeled using a model based on eqns [116] and [117]. The main cathodic process is the reduction of O_2 . Because of the pH effect on the active–passive transition, the mixed potential moves from the active dissolution region for $\text{pH}=0.8$ to the passive region for $\text{pH}=1.8$. This explains the dependence of the experimentally determined corrosion potential on pH (Figure 7(c)). The pH value at which an abrupt change of E_{corr} occurs can be identified with the depassivation pH .

In addition to pH effects, some active ions may influence the magnitude of the passive current density. The effect of active species on the dissolution in the passive state can be modeled by considering surface reactions between the metal oxide film and solution species (Blesa *et al.*,¹⁶⁶ Anderko *et al.*¹⁴⁶):



where X_i is the i th reactive species in the solution, and the subscripts a , b , c_i and e_i represent the reaction stoichiometry. In general, eqn [125] may be written for any active, aggressive, or inhibitive species i in the solution ($i=1, \dots, n$). It is reasonable to assume that eqn [125] is in quasi-equilibrium. The surface species that forms as a result of reaction eqn [125] may undergo irreversible dissolution reactions such as:



in which dissolved metal species are formed in analogy to those described by eqns [118], [120], and [122]. Mathematical analysis of reactions eqns [125] and [126]^{108,146} yields a relationship between the passive current density and activities of reactive species:

$$i_p = i_p^0(\text{pH}) \frac{1 + \sum_i l_i (a_{X_i}^{c_i} / a_{\text{OH}^-}^{e_i})}{1 + \sum_i K_i (a_{X_i}^{c_i} / a_{\text{OH}^-}^{e_i})} \quad [127]$$

where $i_p^0(\text{pH})$ is given by eqn [124], l_i is the forward rate of reaction eqn [126], and K_i is the equilibrium constant of reaction eqn [125].

Figure 8 illustrates the effect of active ions on the rate of general corrosion using alloy 22 in mixed $\text{HNO}_3 + \text{HF}$ solutions as an example. The upper diagram (Figure 8(a)) shows the predicted partial electrochemical processes in a 20% HNO_3 solution and the middle diagram (Figure 8(b)) shows how

these processes change when a moderate amount of HF (1.57%) is added. A 20 wt.% HNO_3 solution is an oxidizing medium, and, therefore, reduction of NO_3^- ions in an acidic environment is the main cathodic process. This results in a high corrosion potential as shown in Figure 8(a). The corrosion rate is controlled by the dissolution rate of the oxide film. When HF is added, the dissolution rate of the oxide substantially increases even though a moderate amount of HF has practically no effect on the acidity of the system. This effect is reproduced by eqn [127] and manifests itself by the increased passive current density in Figure 8(b). The predicted effects can be compared with the observed corrosion rates in 20% HNO_3 solution as a function of HF concentration (Figure 8(c)).

2.38.3.7 Scaling Effects

In addition to passive dissolution and active–passive transition, modeling of surface scale formation is of great practical importance. Scales form as a result of deposition of corrosion products (e.g., iron carbonate or sulfide) or other solids that reach supersaturation near metal interfaces (e.g., calcareous deposits). Scales can be distinguished from passive films in that they do not give rise to the classical active–passive transition such as that shown in Figure 7. Rather, they reduce the rate of dissolution by providing a barrier to the diffusion of species to and from the surface and by partially blocking the interface, thus reducing the overall rate of electrochemical reactions. In general, there may be multiple mechanisms of scale formation depending on the chemistry of the precipitating solids.

One mechanism of scale formation can be quantified in terms of the competition between the rate of scale formation, which results in the precipitation of a corrosion product, and the rate of corrosion under the scale, which leads to the ‘undermining’ of the scale. When the rate of precipitation exceeds the rate of corrosion, dense protective films are formed. Conversely, when the corrosion rate is greater than the precipitation rate, the scale still forms, but the precipitation rate is not fast enough to fill the growing voids. Then, the scale becomes unprotective even though it may be thick. Nešić and Lee¹⁵⁵ developed a model to represent this phenomenon for FeCO_3 scale formation. In Nešić and Lee’s¹⁵⁵ model, the local change in the volumetric concentration of the scale-forming solid is given by a redefined eqn [100]:

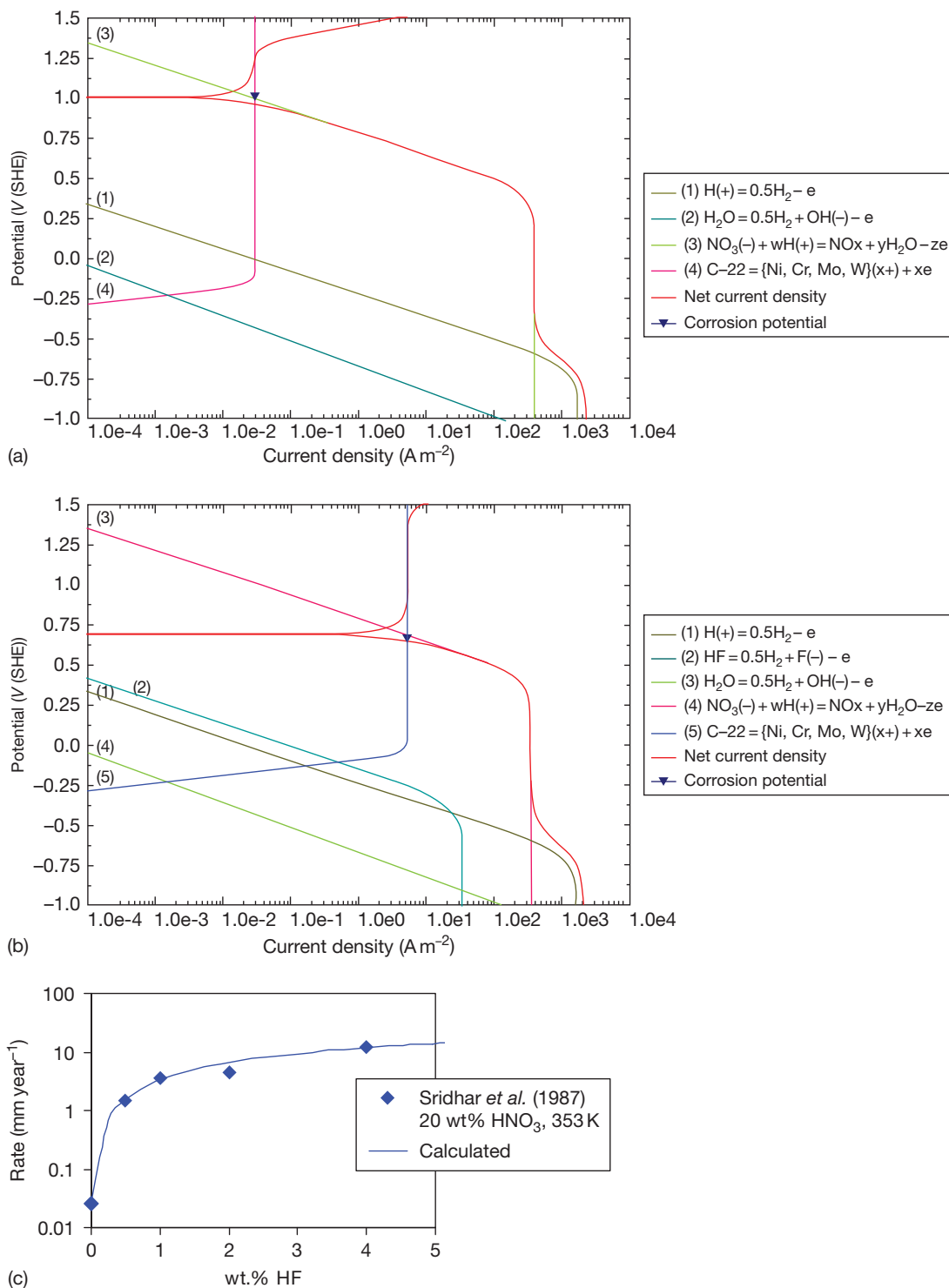


Figure 8 Electrochemical modeling of the effect of HF concentration on the corrosion rate of alloy 22 in HNO₃ + HF solutions. The upper (a) and middle (b) diagrams show the partial electrochemical processes in 20% HNO₃ solutions without HF and with 1.57% HF, respectively. The lower diagram compares the calculated results with experimental data¹⁶⁷ as a function of HF concentration.

$$\frac{\partial c_{\text{solid}}}{\partial t} = R_{\text{solid}} - CR \frac{\partial c_{\text{solid}}}{\partial z} \quad [128]$$

where the first term on the right-hand side represents the rate of the scale formation and the second term is the scale undermining rate. In eqn [128], CR is the corrosion rate and z is a direction perpendicular to the surface. The rate of formation of the scale is, in general, a product of the scale particles' surface area-to-volume ratio A/V , a function of temperature, the thermodynamic solubility product K_{sp} , and an empirical function of supersaturation S :

$$R_{\text{solid}} = \frac{A}{V} f(T) K_{\text{sp}} f(S) \quad [129]$$

where supersaturation is defined as

$$S = \frac{\prod a_i^{v_i}}{K_{\text{sp}}} = \frac{\prod c_i^{v_i}}{K_{\text{sp}}} \quad [130]$$

While the $f(T)$ and $f(S)$ functions can be, in principle, derived from precipitation kinetics data that are independent of corrosion, Sun and Nešić¹⁶⁸ have determined that much more reliable precipitation rates can be obtained from corrosion weight loss and gain measurements than from kinetic measurements that start from dissolved metal ions. The A/V ratio depends on the porosity of the scale on the metal surface. Nešić and Lee¹⁵⁵ developed an empirical function of porosity that is consistent with the experimental data for FeCO_3 scale formation.

A different model is necessary for scales whose formation does not follow the kinetics of precipitation processes. For example, FeS scales form very fast in highly undersaturated solutions, in which they would be thermodynamically unstable in the bulk, and their formation appears not to be influenced by solution supersaturation. Thus, the effect of FeS scales can be modeled by assuming a solid-state reaction at the metal surface that is mediated by the adsorption of H_2S (Anderko and Young,¹⁶⁹ Nešić *et al.*¹⁷⁰) The formation of FeS scales is further complicated by the existence of an outer layer that results from the growth, cracking, and delamination of the FeS film. A model that accounts for these phenomena was developed by Sun and Nešić.¹⁷¹

2.38.3.8 Modeling Threshold Conditions for Localized Corrosion

Modeling of the evolution of localized corrosion has been the subject of extensive research during the past three decades, and a number of important models have been developed for the initiation, stabilization,

propagation, and stifling of individual pits, crevices, and cracks and for the statistical behavior of their ensembles in corroding structures. However, this topic is outside the scope of this chapter and will be reviewed in the chapter 'Predictive Modeling of Corrosion' in this volume.

In this chapter, we focus solely on models that predict the conditions for the occurrence of localized corrosion without going into the treatment of the evolution of localized corrosion events in time and space. Such models are designed to find the threshold criteria for localized corrosion. In general, localized corrosion occurs when the corrosion potential of an alloy in a given environment exceeds a critical potential. The meaning, experimental determination, and interpretation of the key potentials that characterize localized corrosion have been reviewed by Szklarska-Smialowska.¹⁷² While this general concept is well accepted, what constitutes a critical potential continues to be debated. The selection of the critical potential depends on the particular phenomenon that is to be modeled.

The applicability of the critical potential concept to modeling localized corrosion is qualitatively illustrated in Figure 9. In this figure, the arrows indicate the conditions at which localized corrosion is expected. For a given alloy, the critical potential decreases with an increase in the concentration of aggressive species (e.g., halide ions) as shown in Figure 9(a). The shape of the E_{crit} curve corresponds to that of the repassivation potential curve, but the qualitative pattern is more general. Unlike the critical potential, the corrosion potential is usually not a strong function of aggressive ion concentration unless significant localized corrosion occurs. The critical aggressive species concentration for localized corrosion is observed when E_{corr} exceeds E_{crit} . Similarly, for a given aggressive chemical environment, a critical temperature exists (see Figure 9(b)). The critical potential is also strongly affected by the presence of inhibitors. As shown in Figure 9(c), this gives rise to a critical inhibitor concentration. In many environments, the presence of oxidants may increase E_{corr} so that localized corrosion may occur beyond a critical concentration of redox species (Figure 9(d)). The actual conditions in a system may be a combination of the four idealized cases shown in Figure 9. Thus, the key is to predict both the corrosion potential and the repassivation potential. The corrosion potential can be obtained from a general-corrosion, mixed-potential model for passive metals as described above. For the critical potential, separate models are necessary.

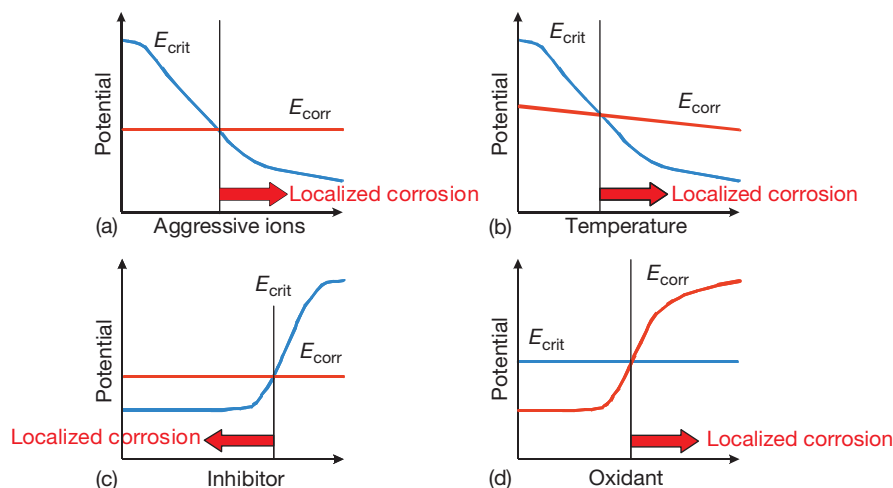


Figure 9 A general conceptual scheme of the use of the corrosion potential (E_{corr}) and critical potential (E_{crit}) to predict the effect of aggressive ions, temperature, inhibitors, and oxidizing redox species on localized corrosion. The arrows marked 'localized corrosion' denote the potential ranges in which localized corrosion can be expected.

In this chapter, we briefly review the computation and applicability of the passivity breakdown potential and the repassivation potential.

2.38.3.8.1 Breakdown of passivity

To predict the initiation of localized corrosion, it is necessary to calculate the critical passivity breakdown potential. Several theories have been developed to relate the breakdown potential to the concentration of aggressive species in the solution (Heusler and Fischer,¹⁷³ Strehblow and Titzte,¹⁷⁴ Lin *et al.*,¹⁷⁵ Okada,¹⁷⁶ McCafferty,¹⁷⁷ Haruna and Macdonald,¹⁷⁸ Macdonald,⁹⁷ Yang and Macdonald,¹⁷⁹ and papers cited therein). A common theoretical result, confirmed by experimental data, is the linear dependence of the passivity breakdown potential on the logarithm of the concentration of aggressive ions. While this observation is generally accepted, its generalization to systems with multiple aggressive and inhibitive ions is not immediately obvious.

A particularly comprehensive treatment of passivity breakdown is provided by the point defect model of Macdonald and coworkers (Lin *et al.*,¹⁷⁵ Haruna and Macdonald,¹⁷⁸ Macdonald,⁹⁷ Yang and Macdonald¹⁷⁹). According to the point defect model, passivity breakdown results from the condensation of cation or metal vacancies at the interface between the metal and the passive barrier layer. The vacancies are envisaged to be generated at the barrier layer–solution interface in an autocatalytic, anion-induced process. For systems containing only aggressive (halide) ions X^- , the critical breakdown potential is expressed as

$$E_b = \frac{4.606RT}{\chi\alpha F} \log \left[\frac{\mathcal{J}_m}{\hat{a}Du^{-\chi/2}} \right] - \frac{2.303RT}{\alpha F} \log a_X \quad [131]$$

where \mathcal{J}_m is the rate of annihilation of cation vacancies at the metal/barrier layer interface, \hat{a} and u are thermodynamic parameters related to the absorption of an aggressive ion into an oxygen vacancy, D is the cation vacancy diffusivity, and α is the polarizability of the film–solution interface. Yang and Macdonald¹⁷⁹ extended eqn [131] to systems containing both aggressive ions X^- and inhibitive ions Y^{z-} :

$$E_b = E_b^0 - \frac{\beta}{\alpha} \text{pH} - \frac{2.303}{\alpha\alpha_0 F} \log \frac{a_{X^-}}{a_{Y^{z-}}} \quad [132]$$

where the constant E_b^0 is a function of adsorption and elementary reaction rate parameters that is derived from a competitive adsorption model for the X^- and Y^{z-} species, β is the dependence of the potential drop across the barrier layer–solution interface on pH, and α_0 is a transfer coefficient. The predictions of the point defect model have been found to be in agreement with experimental phenomena including the linear dependence of the breakdown potential on the concentrations of aggressive and inhibitive ions, the dependence of the induction time on potential and chloride concentration, dependence of the breakdown potential on the scan rate and the inhibition of pitting by Mo and W in the alloy. It should be noted that the breakdown potential is a distributed quantity that can be described with a normal distribution function. The distribution in E_b has been reproduced by assuming that the cation diffusivity is normally distributed.⁹⁷

While the logarithmic dependence of the breakdown potential on the aggressive species concentration is predicted by most passivity breakdown models, the induction time provides a more stringent criterion for testing alternative models. Accordingly, Milošev *et al.*¹⁸⁰ tested the validity of the point defect model, the two-dimensional nucleation model of Heusler and Fischer,¹⁷³ and the halide nuclei model of Okada¹⁷⁶ for the pitting of copper. The point defect model was found to yield the best agreement with experimental data.

2.38.3.8.2 Repassivation potential and its use to predict localized corrosion

While the breakdown potential is the critical parameter for the initiation of pitting, the repassivation potential (E_{rp}) has been used for predicting the long-term occurrence of pitting and crevice corrosion. The repassivation potential (also called protection potential) is the potential at which a stably growing pit or crevice corrosion will cease to grow. Thus, localized corrosion cannot occur at potentials below E_{rp} . The use of E_{rp} for engineering predictions can be justified by the fact that only the fate of stable pits or crevice corrosion is important for predicting the possibility of failure, and metastable pits do not adversely affect the performance of engineering structures. It has been shown by Dunn *et al.*^{181,182} that E_{rp} is practically independent of the amount of charge passed in a localized corrosion process as long as it is above a certain minimum amount of charge. As a result, the repassivation potential is relatively insensitive to prior pit depth and surface finish. As a corollary, it has been shown that the repassivation potential for pitting (i.e., measured on an open sample) and the repassivation potential for crevice corrosion (i.e., measured on a creviced sample) coincide at high pit depths. This has demonstrated the utility of the repassivation potential for engineering design as it provides a reproducible and inherently conservative threshold for the occurrence of localized corrosion. Thus, the prediction of long-term occurrence of localized corrosion can be separated into two independent parts, that is, the calculation of the repassivation and the corrosion potentials. The separation of localized corrosion modeling into these two steps is valid as long as the initial stages of stable localized corrosion are considered because the corrosion potential is not affected at this stage by the progress of the localized corrosion process and the interaction between pits can be ignored. The separation remains valid as long as significant pit or crevice corrosion growth does not occur and the area of an actively

corroding pit does not become significant compared to the overall area.

A model for calculating the repassivation potential has been developed by Anderko *et al.*¹⁸³ by considering the electrochemistry of a metal M that undergoes dissolution underneath a layer of concentrated metal halide solution MX. The concentrated solution may or may not be saturated with respect to a hydrous solid metal halide. In the process of repassivation, a thin layer of oxide forms at the interface between the metal and the hydrous metal halide. The model assumes that, at a given instant, the oxide layer covers a certain fraction of the metal surface. This fraction increases as repassivation is approached. Further, the model includes the effects of multiple aggressive and nonaggressive or inhibitive species, which are taken into account through a competitive adsorption scheme. The aggressive species form metal complexes, which dissolve in the active state. On the other hand, the inhibitive species and water contribute to the formation of oxides, which induce passivity. The model assumes that the measurable potential drop across the interface can be expressed as a sum of four contributions, that is

$$E = \Delta\Phi_{M/MX} + \Delta\Phi_{MX} + \Delta\Phi_{MX/S} + \Delta\Phi_S \quad [133]$$

where $\Delta\Phi_{M/MX}$ is the potential difference at the interface between the metal and metal halide, which may be influenced by the partial coverage by the metal oxide, $\Delta\Phi_{MX}$ is the potential drop across the hydrous halide layer, $\Delta\Phi_{MX/S}$ is the potential difference across the metal halide–solution interface, and $\Delta\Phi_S$ is the potential drop across the boundary layer within the solution. Expressions for the potential drops can be derived using the methods of nonequilibrium thermodynamics.¹⁸⁴ In general, these expressions are complex and can be solved only numerically. However, a closed-form equation has been found in the limit of repassivation, that is, when the current density reaches a predetermined low value i_{rp} (typically $i_{rp} = 10^{-2} \text{ A m}^{-2}$) and the fluxes of metal ions become small and comparable to those for passive dissolution. Then, eqn [133] can be used to arrive at a closed-form expression for the repassivation potential. This closed-form expression, which can be solved numerically to calculate E_{rp} is given by:

$$\begin{aligned} 1 + \sum_k \left[\left(\frac{i_{rp}}{i_p} - 1 \right) \frac{l_k''}{i_{rp}} \theta_k^{n_k} \exp\left(\frac{\zeta_k F E_{rp}}{RT}\right) \right. \\ \left. = \sum_j \frac{k_j''}{i_{rp}} \theta_j^{n_j} \exp\left(\frac{\alpha_j F E_{rp}}{RT}\right) \right] \quad [134] \end{aligned}$$

where i_p is the passive current density, T is the temperature, R is the gas constant, and F is the Faraday constant. The partial coverage fraction of a species j is related to the activity of this species in the bulk solution by

$$\theta_j = \frac{K_{\text{ads},j} a_j}{1 + \sum_k K_{\text{ads},k} a_k} \quad [135]$$

where

$$K_{\text{ads},j} = \exp\left(-\frac{\Delta G_{\text{ads},j}}{RT}\right) \quad [136]$$

and $\Delta G_{\text{ads},j}$ is the Gibbs energy of adsorption. The parameters k'_j and l''_k in eqn [134] are rate constants for surface reactions mediated by the adsorption of aggressive and inhibitive species, respectively. The inhibitive species include water, as it is necessary for oxide formation. The parameter n_j is the reaction order with respect to species j , and α_j and ξ_k are the electrochemical transfer coefficients for reactions mediated by aggressive and inhibitive species, respectively. Some parameters ($\Delta G_{\text{ads},i}$, α_j , and n_k) can be assigned default values. The remaining parameters need to be regressed from a limited amount of experimental E_{rp} measurements. Since E_{rp} data are most abundant for chloride solutions, the rate constant for the chloride ions (k'_{Cl}), reaction order with respect to chlorides (n_{Cl}), rate constant for water ($l''_{\text{H}_2\text{O}}$), and electrochemical transfer coefficient for water ($\xi_{\text{H}_2\text{O}}$) are determined based on the data for chloride solutions. The determination of parameters is greatly simplified by the fact that the parameters for Fe–Ni–Cr–Mo–W–N alloys can be correlated with alloy composition,^{185,186} thus enhancing the predictive value of the model. The k'_j and, if necessary, n_j parameters are determined for other aggressive species j (e.g., bromide ions) using E_{rp} data for either pure or mixed

solutions containing such ions. Finally, the l''_k parameters for inhibitive ions k are determined on the basis of data for mixed solutions containing chlorides and inhibitors. Data for mixed systems are necessary because E_{rp} is undefined in solutions containing only inhibitors.

The repassivation potential model has a limiting character, that is, it accurately represents the state of the system in the repassivation potential limit. In addition to the value of the repassivation potential, the model predicts the correct slope of the current density versus potential relationship as the potential deviates from E_{rp} .¹⁸³ The current density predicted by the model as a function of potential is given by

$$i = \frac{\sum_j k'_j \theta_j^{n_j} \exp\left(\frac{\alpha_j FE}{RT}\right) + \sum_j l''_j \theta_j^{n_j} \exp\left(\frac{\xi_j FE}{RT}\right)}{1 + \frac{1}{i_p} \sum_j l''_j \theta_j^{n_j} \exp\left(\frac{\xi_j FE}{RT}\right)} \quad [137]$$

Equation [137] reduces to eqn [134] for $E = E_{\text{rp}}$ and $i = i_p$. Since eqn [137] is a limiting law, its accuracy gradually deteriorates as the potential increasingly deviates from E_{rp} . Equation [137] cannot be regarded as a model for the propagation rate of an actively growing pit or crevice because it does not take into account the factors such as the ohmic potential drop, transport limitations, and so on. However, the current density predicted using eqn [137] for $E > E_{\text{rp}}$ is useful because it provides an estimate of the maximum propagation rate of an isolated pit as a function of potential. Such an upper estimate is convenient because it relies only on parameters that are calibrated using repassivation potential data.

Figure 10 shows the application of the repassivation potential model to alloy CuNi 7030 in chloride

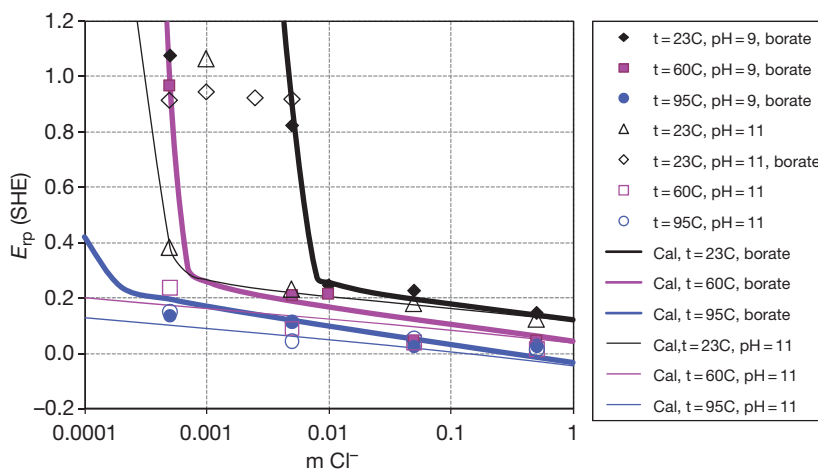


Figure 10 Modeling the repassivation potential of alloy CuNi 7030 (UNS C71500).²¹⁷ as a function of chloride activity at various temperatures.

solutions at three temperatures. As shown in the figure, the slope of the repassivation potential changes as a function of chloride activity. A steeper slope is observed at low chloride concentrations. This is a general phenomenon for alloys and becomes more pronounced for more corrosion-resistant alloys.¹⁸³ The transition between the low-slope and high-slope segments of the curves strongly depends on the alloy and temperature.

A particularly useful application of the repassivation potential model is for investigating the competing effects of aggressive and inhibitive species. For example, **Figure 11** shows the inhibitive effect of nitrate ions on localized corrosion of alloy 22 in concentrated chloride solutions. The E_{rp} versus NO_3^- concentration curves have a characteristic shape with two distinct slopes. As the concentration of the NO_3^- ions is increased, the slope of the E_{rp} versus NO_3^- concentration curve initially slowly increases with a low slope. At a certain concentration of NO_3^- , the slope of the E_{rp} curve rapidly increases and the repassivation potential attains a high value. At NO_3^- concentrations that lie beyond the high-slope portion of the E_{rp} versus NO_3^- curve, localized corrosion becomes impossible even in systems with a high corrosion potential. Thus, there is a fairly narrow range of inhibitor concentrations over which the E_{rp} curve transitions from a low-slope region (in which localized corrosion is possible depending on the value of the corrosion potential) to a high-slope region that constitutes the upper limit of inhibitor concentrations for localized corrosion. The exact location of the transition region depends on the temperature and chloride concentration and can be accurately reproduced using the repassivation potential model.

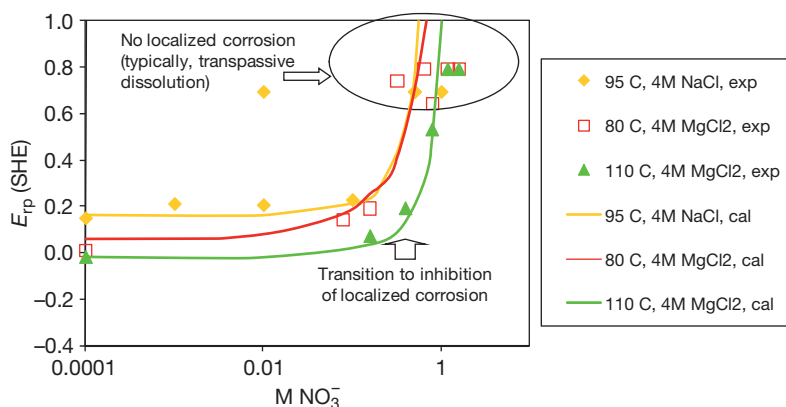


Figure 11 Modeling the effect of nitrate ions on the repassivation potential of alloy 22 in concentrated chloride solutions. The experimental data are from Dunn *et al.*¹⁸⁷

Figure 12 illustrates an application of the corrosion potential and repassivation potential models to predict the critical crevice temperature. At temperatures below critical crevice temperature (CCT), the calculated corrosion potential (E_{corr}) should lie below the repassivation potential, whereas it should exceed E_{rp} above CCT. Thus, the intersection of the E_{corr} and E_{rp} curves versus temperature provides an estimate of CCT. **Figure 12** shows the results of such calculations for alloy C-276 in 6% FeCl_3 solutions.¹⁸⁸ The repassivation potential shows an initially steep decrease followed by a moderate decrease at higher temperatures. On the other hand, the corrosion potential shows a much weaker temperature dependence. The intersection points of the E_{corr} and E_{rp} curves can be compared with experimental critical crevice temperatures (Hibner¹⁸⁹).

It should be noted that while the approach based on computing E_{corr} and E_{rp} can predict the long-term occurrence and maximum propagation rate of localized corrosion, it gives no spatial or temporal information. For predicting the spatial and temporal evolution of localized corrosion, models are required that include a detailed treatment of mass transport and take into account the geometric constraints of crevices, pits, and so on. Such models are outside the scope of this chapter.

2.38.3.9 Selected Practical Applications of Aqueous Corrosion Modeling

In this section, we briefly outline selected models that have been developed for practical applications on the basis of the principles discussed above.

Extensive efforts have been devoted to the modeling of aqueous corrosion in oil and gas environments.

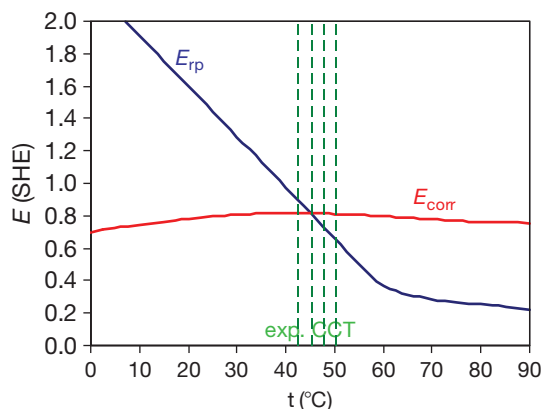


Figure 12 Prediction of the critical crevice temperature (CCT) for various alloys in a 6% FeCl_3 solution using corrosion potential and repassivation potential models.¹⁸⁸ The vertical lines show the location of the experimental CCT values.¹⁸⁹ The intersection of the calculated corrosion potential and repassivation potential lines shows the predicted critical crevice temperature.

This is due to the great practical importance of corrosion in oil and gas production and transmission, and to the fact that the number of key corrosive components in such environments is relatively limited (primarily to CO_2 , H_2S , acetic acid, and O_2), thus making the modeling task manageable despite the inherent complexity of corrosion mechanisms and their dependence of flow conditions. Corrosion modeling in this area has been reviewed by Nešić *et al.*,¹⁹⁰ Nyborg,¹⁹¹ and Papavisanam *et al.*^{192–194} The $\text{CO}_2/\text{H}_2\text{S}$ models range from expert systems based on laboratory and field data to mechanistic models that recognize the partial electrochemical processes in an explicit way. Among the electrochemical models, the treatment of flow effects using mass transfer coefficients has found wide applicability for both single-phase and two-phase flow (Nešić *et al.*,¹¹⁵ Dayalan *et al.*,¹⁹⁵ Anderko and Young,¹⁶⁹ Pots and Kapusta,¹⁹⁶ Deng *et al.*¹⁹⁷). While the methodology for modeling CO_2 corrosion is well established, the modeling of H_2S effects is still in a state of flux and is a subject of significant research efforts (Anderko and Young,¹⁶⁹ Nešić *et al.*,¹⁷⁰ Sun and Nešić¹⁷¹). A CO_2 corrosion model based on a detailed treatment of transport (eqns [100]–[103]) has been developed by Nordsveen *et al.*,¹¹⁶ Nešić *et al.*,¹⁹⁸ and Nešić and Lee.¹⁶⁶ This model has been further extended to $\text{CO}_2/\text{H}_2\text{S}$ corrosion by considering mechanistic aspects of FeS scale formation (Nešić *et al.*,¹⁷⁰ Sun and Nešić¹⁷¹). The model has been integrated with a multiphase flow model, which made it possible to predict the effect of water entrainment and water wetting in oil–water

systems (Nešić *et al.*¹⁷⁰). Also, a stochastic algorithm for predicting localized corrosion due to partially protective FeCO_3 scales has been integrated with this model (Nešić *et al.*¹⁹⁹).

Another area in which electrochemical models have found wide applicability is the prediction of the corrosion potential in dilute aqueous solutions that exist in power generation industries. In particular, mixed-potential models have been developed for stainless steels in water as a function of oxygen and hydrogen content (Macdonald,¹⁶¹ Lin *et al.*,¹³⁸ Kim¹⁰³). Such models are useful for calculating E_{corr} in boiling water reactors and related environments. E_{corr} is then further used for localized corrosion modeling. In such systems, modeling of the initiation and evolution of crevice corrosion, stress corrosion cracking, and corrosion fatigue is of primary importance. For this purpose, several electrochemical models that are suitable for alloys in high temperature and low-conductivity water have been developed (see Betts and Boulton,²⁰⁰ Turnbull,^{201–203} Engelhardt *et al.*^{204,205} and references therein).

Corrosion in halide-containing natural and industrial environments such as seawater, deliquescent liquids, or production brines is another important application for modeling. For example, King *et al.*¹²³ developed a model for calculating the corrosion potential of copper in aerated chloride solutions. Anderko and Young¹⁰⁸ modeled general corrosion of steel in concentrated bromide brines used in absorption cooling. Sridhar *et al.*¹³¹ developed a model that predicts both the general corrosion and the occurrence of localized corrosion for stainless steels and aluminum in seawater. A mixed-potential model has been developed to predict the behavior of nuclear fuel in steel containers (Shoosmith *et al.*²⁰⁶). Models for the initiation, stabilization, and propagation of pitting, crevice corrosion, and cracking in halide systems have been developed by a number of authors (Turnbull and Ferris,²⁰⁷ Turnbull,^{203,208} Betts and Boulton,²⁰⁰ Engelhardt *et al.*,^{209,210} Cui *et al.*,²¹¹ and references therein).

Modeling corrosion in the process industries is a potentially fruitful area but is subject to great difficulties because of the complex and variable nature of the chemical environments. In principle, acid systems are amenable to modeling because of their well-defined chemistry. In particular, corrosion in acids has been modeled by Sridhar and Anderko²¹² in the moderate concentration range. Rahmani and Strutt²¹³ developed a model for very concentrated sulfuric acid solutions, in which corrosion can be assumed to

be exclusively under mass transport control. Veawab and Arronwilas²¹⁴ developed a model for the general corrosion in amine-CO₂ systems. Models are also available for the corrosivity in wet porous media (Huet *et al.*²¹⁵). Anderko *et al.*²¹⁶ applied the localized corrosion model based on calculating the repassivation and corrosion potentials to predict the occurrence of pitting and estimate the worst-case propagation rates of localized corrosion in a process environment.

2.38.4 Concluding Remarks

Over the past three decades, tremendous progress has been achieved in the development of computational models of aqueous corrosion. A number of practically important models have been developed for applications as diverse as oil and gas production and transmission, nuclear and fossil power generation, seawater service, and various chemical processes.

Thermodynamic models of electrolyte systems have reached a level of sophistication that extended their applicability range from dilute aqueous solutions to multiphase, multicomponent systems ranging from infinite dilution to solid saturation or pure solute limits. Although they were originally developed mostly for applications other than corrosion (especially chemical processing and geology), they are increasingly used to predict the solution chemistry of corrosive environments and to understand the effect of phase behavior on corrosion. Electrochemical models of corroding interfaces have been developed to predict the kinetics of anodic and cathodic reactions that are responsible for corrosion and to relate them to bulk solution chemistry and flow conditions. Semiempirical and mechanistic models of passivity have been developed to predict the behavior of passive metals and the breakdown of passivity. Also, models are available to predict the threshold conditions for localized corrosion.

The main focus of the models reviewed in this chapter is on relating the chemistry of the environment to electrochemical corrosion phenomena on metal surfaces. However, this is often only the first stage of corrosion modeling. Beyond this stage, the models discussed here serve as a basis for simulating the spatial and temporal evolution of localized and general corrosion damage in various engineering structures subject to localized and general corrosion. This level of modeling will be discussed in other chapters of this volume.

Acknowledgments

The work reported in this paper has been supported by the Department of Energy (award number DE-FC36-04GO14043) and cosponsored by Chevron-Texaco, DuPont, Haynes International, Mitsubishi Chemical, Shell, and Toyo Engineering.

References

1. Pourbaix, M. *Atlas of Electrochemical Equilibria in Aqueous Solutions*; Pergamon Press: New York, NY, 1966.
2. Pitzer, K. S. *Thermodynamics*, 3rd ed.; McGraw-Hill: New York, NY, 1995.
3. Anderko, A.; Wang, P.; Rafal, M. *Fluid Phase Equil.* **2002**, *194–197*, 123–142.
4. Zemaitis, J. F., Jr.; Clark, D. M.; Rafal, M.; Scrivner, N. C. *Handbook of Aqueous Electrolyte Thermodynamics*; DIPPR, AIChE: New York, NY, 1986.
5. Renon, H. *Fluid Phase Equil.* **1986**, *30*, 181–195.
6. Pitzer, K. S. Ed. *Activity Coefficients in Electrolyte Solutions*, 2nd ed.; CRC Press: Boca Raton, FL, 1991.
7. Rafal, M.; Berthold, J. W.; Scrivner, N. C.; Grise, S. L. In *Models for Thermodynamic and Phase Equilibria Calculations*; Sandler, S. I., Ed.; Marcel Dekker: New York, NY, 1994; pp 601–670.
8. Loehe, J. R.; Donohue, M. D. *AIChE J.* **1997**, *43*, 180–195.
9. Chase, M. W.; Davies, C. A.; Downey, J. R.; Frurip, D. J.; McDonald, D. A.; Syverud, A. N. *JANAF Thermochemical Tables*, 3rd ed., supplement no. 1, *J. Phys. Chem. Ref. Data* **1985**, *14*, 1–1856.
10. Barin, I.; Platzki, G. *Thermochemical Data of Pure Substances*, 3rd ed.; Wiley-VCH: Verlag, 1997.
11. Cox, J. D.; Wagman, D. D.; Medvedev, V. A. *CODATA Key Values for Thermodynamics*; Hemisphere Publishing: New York, 1989.
12. Glushko, V. P.; Medvedev, V. A.; Bergman, G. A.; Vasil'ev, B. P.; Kolesov, V. P.; Gurvich, L. V.; Yungman, V. S.; Khodakovskii, I. L.; Resnitskii, L. A.; Smirnova, N. L.; *et al.* *Thermal Constants of Compounds*; Academy of Sciences: Moscow, USSR, 1965–1981.
13. Gurvich, L. V.; Veyts, I. V.; Alcock, C. B.; Iorish, V. S. *Thermodynamic Properties of Individual Substances*; Hemisphere Publishing: New York, 1988–1998; Vols 1–5.
14. Kelly, K. K. Contribution to the Data on Theoretical Metallurgy XIII. High Temperature Heat Content, Heat Capacity and Entropy Data for the Elements and Inorganic Components, Bull. 584, Bureau of Mines, US Dept. of Interior, 1960.
15. Robie, R. A.; Hemingway, B. S.; Fisher, J. R. *US Geol. Survey Bull* **1978**, 1452.
16. Shock, E. L.; Helgeson, H. C. *Geochim. Cosmochim. Acta* **1988**, *52*, 2009–2036; *Geochim. Cosmochim. Acta* **1990**, *54*, 915–943.
17. Shock, E. L.; Helgeson, H. C.; Sverjensky, D. A. *Geochim. Cosmochim. Acta* **1989**, *53*, 2157–2183.
18. Shock, E. L.; Sassani, D. C.; Willis, M.; Sverjensky, D. A. *Geochim. Cosmochim. Acta* **1997**, *61*, 907–950.
19. Stull, D. R.; Westrum, E. F., Jr.; Sinke, G. L. *The Chemical Thermodynamics of Organic Compounds*; R. F. Krieger: Malabara, FL, 1987.

20. Wagman, D. D.; Evans, W. H.; Parker, V. B.; Shum, R. H.; Halow, I.; Bailey, S. M.; Churney, K. L.; Nuttal, R. L. *J. Phys. Chem. Ref. Data* **1982**, *11*(2), 1–392.
21. Criss, C.; Cobble, J. *J. Am. Chem. Soc.* **1964**, *86*, 5385–5390; *J. Am. Chem. Soc.* **1964**, *86*, 5390–5393.
22. Helgeson, H. C.; Kirkham, D. H.; Flowers, G. C. *Am. J. Sci.* **1974**, *274*, 1089–1198; *Am. J. Sci.* **1974**, *274*, 1199–1261; *Am. J. Sci.* **1976**, *276*, 97–240; *Am. J. Sci.* **1981**, *281*, 1241–1516.
23. Tanger, J. C., IV; Helgeson, H. C. *Am. J. Sci.* **1988**, *288*, 19–98.
24. Sverjensky, D. A.; Shock, E. L.; Helgeson, H. C. *Geochim. Cosmochim. Acta* **1997**, *61*, 1359–1412.
25. Johnson, J. W.; Oelkers, E. H.; Helgeson, H. C. *Comput. Geosci.* **1992**, *18*, 899–947.
26. Sedlbauer, J.; O'Connell, J. P.; Wood, R. H. *Chem. Geol.* **2000**, *163*, 43–63.
27. Sedlbauer, J.; Majer, V. *Eur. J. Mineral.* **2000**, *12*, 1109–1122.
28. Kolker, A.; de Pablo, J. J. *Ind. Eng. Chem. Res.* **1996**, *35*, 228–233; *Ind. Eng. Chem. Res.* **1996**, *35*, 234–240.
29. Pitzer, K. S. *J. Phys. Chem.* **1973**, *77*, 268–277.
30. Debye, P.; Hückel, E. *Physik. Z.* **1923**, *24*, 185–206; *Physik. Z.* **1923**, *24*, 305–325; *Physik. Z.* **1924**, *25*, 97–107.
31. Wu, R.-S.; Lee, L. L. *Fluid Phase Equil.* **1992**, *78*, 1–24.
32. Papaiconomou, N.; Simonin, J.-P.; Bernard, O.; Kunz, W. P. *Phys. Chem. Chem. Phys.* **2002**, *4*, 4435–4443.
33. Guggenheim, E. A. *Philos. Mag* **1935**, *19*, 588–643.
34. Guggenheim, E. A.; Turgeon, J. C. *Trans. Faraday Soc.* **1955**, *51*, 747–761.
35. Helgeson, H. C. *Am. J. Sci.* **1969**, *267*, 729.
36. Bromley, L. A. *AIChE J.* **1973**, *19*, 313–320.
37. Zemaitis, J. F., Jr. *ACS Symp. Series* **1980**, *133*, 227–246.
38. Meissner, H. P. *ACS Symp. Series* **1980**, *133*, 495–511.
39. Pitzer, K. S.; Simonson, J. M. *J. Phys. Chem.* **1986**, *90*, 3005–3009.
40. Clegg, S. L.; Pitzer, K. S. *J. Phys. Chem.* **1992**, *96*, 3513–3520.
41. Chen, C.-C.; Britt, H. I.; Boston, J. F.; Evans, L. B. *AIChE J.* **1982**, *28*, 588–596.
42. Liu, Y.; Watanasiri, S. *Fluid Phase Equil.* **1996**, *116*, 193–200.
43. Abovsky, V.; Liu, Y.; Watanasiri, S. *Fluid Phase Equil.* **1998**, *150*, 277–286.
44. Chen, C.-C.; Mathias, P. M.; Orbey, H. *AIChE J.* **1999**, *45*, 1576–1586.
45. Chen, C.-C.; Song, Y. *AIChE J.* **2004**, *50*, 1928–1941.
46. Sander, B.; Fredenslund, A.; Rasmussen, P. *Chem. Eng. Sci.* **1986**, *41*, 1171–1183.
47. Macedo, E. A.; Skovborg, P.; Rasmussen, P. *Chem. Eng. Sci.* **1990**, *45*, 875–882.
48. Kikic, I.; Fermeglia, M.; Rasmussen, P. *Chem. Eng. Sci.* **1991**, *46*, 2775–2780.
49. Dahl, S.; Macedo, E. A. *Ind. Eng. Chem. Res.* **1992**, *31*, 1195–1201.
50. Iliuta, M. C.; Thomsen, K.; Rasmussen, P. *Chem. Eng. Sci.* **2000**, *55*, 2673–2686.
51. Li, J.; Polka, H.-M.; Gmehling, J. *Fluid Phase Equil.* **1994**, *94*, 89–114.
52. Yan, W.; Topphoff, M.; Rose, C.; Gmehling, J. *Fluid Phase Equil.* **1999**, *162*, 97–113.
53. Zerres, H.; Prausnitz, J. M. *AIChE J.* **1994**, *40*, 676–691.
54. Wang, P.; Anderko, A.; Young, R. D. *Fluid Phase Equil.* **2002**, *203*, 141–176.
55. Wang, P.; Anderko, A.; Springer, R. D.; Young, R. D. *J. Molec. Liq.* **2006**, *125*, 37–44.
56. Prausnitz, J. M.; Lichtenthaler, R. N.; Gomes de Azevedo, E. *Molecular Thermodynamics of Fluid Phase Equilibria*; Prentice-Hall: Englewood Cliffs, NJ, 1998.
57. Malanowski, S.; Anderko, A. *Modeling Phase Equilibria: Thermodynamic Background and Practical Tools*; Wiley: New York, 1992.
58. Chen, C. M.; Aral, K. *Corrosion* **1982**, *38*, 183–190.
59. Chen, C. M.; Aral, K.; Theus, G. J. *Computer Calculated Potential-pH Diagrams to 300 °C*, EPRI NP 3137; Electric Power Research Institute: Palo Alto, CA, 1983; Vols. 1–2.
60. Partridge, E.; Hall, R. *Trans. Am. Soc. Mech. Eng* **1939**, *61*, 597.
61. OLI Systems Inc. Corrosion Analyzer software version 2.0, www.olisystems.com, 2007.
62. Anderko, A.; Sanders, S. J.; Young, R. D. *Corrosion* **1997**, *53*, 43–53.
63. Macdonald, D. D.; Cragolino, G. A. In *The ASME Handbook on Water Technology for Thermal Power Systems*; Cohen, P., Ed.; American Society of Mechanical Engineers: New York, 1989; Chapter 9.
64. Beverskog, B.; Puigdomenech, I. *Corros. Sci.* **1996**, *38*, 2121–2135.
65. Beverskog, B.; Puigdomenech, I. *J. Electrochem. Soc.* **1997**, *144*, 3476–3483.
66. Beverskog, B.; Puigdomenech, I. *Corros. Sci.* **1997**, *39*, 43–57.
67. Beverskog, B.; Puigdomenech, I. *Corros. Sci.* **1997**, *39*, 969–980.
68. Beverskog, B.; Puigdomenech, I. *Corros. Sci.* **1997**, *39*, 107–114.
69. Beverskog, B.; Puigdomenech, I. *Corrosion* **1999**, *55*, 1077–1087.
70. Biernat, R. J.; Robbins, R. G. *Electrochim. Acta* **1972**, *17*, 1261–1283.
71. Froning, M. H.; Shanley, M. E.; Verink, E. D., Jr. *Corros. Sci.* **1976**, *16*, 371–376.
72. Macdonald, D. D.; Syrett, B. C. *Corrosion* **1979**, *35*, 471–474.
73. Macdonald, D. D.; Syrett, B. C.; Wing, S. S. *Corrosion* **1979**, *35*, 1–11.
74. Macdonald, D. D.; Syrett, B. C.; Wing, S. S. *Corrosion* **1979**, *35*, 367–378.
75. Anderko, A.; Shuler, P. J. *Comput. Geosci.* **1997**, *23*, 647–658.
76. Pourbaix, M. In *Localized Corrosion*; Staehle, R. W., Brown, B. F., Kruger, J., Agarwal, A., Eds.; NACE: Houston, TX, 1974; pp 12–33.
77. Kesavan, S.; Mozhi, T. A.; Wilde, B. E. *Corrosion* **1989**, *45*, 213–214.
78. Muñoz-Portero, M. J.; Garcia-Anton, J.; Guiñón, J. L.; Perez-Herranz, V. *Corrosion* **2004**, *60*, 749–756.
79. Bianchi, G.; Longhi, P. *Corros. Sci.* **1973**, *13*, 853–864.
80. Silverman, D. C. *Corrosion* **1982**, *38*, 541–549.
81. Silverman, D. C. *Corrosion* **1988**, *44*, 606–610.
82. Kubal, M.; Panacek, F. *Br. Corros. J.* **1995**, *30*, 309–311.
83. Silverman, D. C.; Silverman, A. L. *Corrosion/2007*; NACE International: Houston, TX, 2007; Paper no. 07616.
84. Cubicciotti, D. J. *Nucl. Mat.* **1989**, *167*, 241–248.
85. Cubicciotti, D. J. *Nuclear Mat.* **1993**, *201*, 176–183.
86. Yang, L. X.; Yang, X. Z.; Pourbaix, A. *Corrosion/2007*; NACE International: Houston, TX, 2007; Paper no. 01084.
87. Anderko, A.; Wang, P.; Young, R. D.; Riemer, D. P.; McKenzie, P.; Lencka, M. M.; Babu, S. S.; Angelini, P. Prediction of Corrosion of Alloys in Mixed-Solvent Environments, Final report, DE-FC07-00CH11019, DOE OIT, 2003, www.osti.gov/servlets/purl/811533-wUOQwz/native/.
88. Lupis, C. H. *Chemical Thermodynamics of Materials*; North Holland: New York, 1983.

89. Saunders, N.; Miodownik, A. P. *CALPHAD – Calculation of Phase Diagrams – A Comprehensive Guide*; Pergamon/Elsevier Science: New York, 1998.
90. Hertzman, S. *Metall. Trans. A* **1987**, *18A*, 1753–1766; *Metall. Trans. A*, **1987**, *18A*, 1767–1778.
91. Hertzman, S.; Jarl, M. *Metall. Trans. A* **1987**, *18A*, 1745–1752.
92. Andersson, J.-O.; Lange, N. *Metall. Trans. A* **1988**, *19A*, 1385–1394.
93. Sridhar, N.; Dunn, D. S.; Anderko, A.; Lencka, M. M.; Schutt, H. U. *Corrosion* **2001**, *57*, 221–235.
94. Lencka, M. M.; Nielsen, E.; Anderko, A.; Riman, R. E. *Chem. Mater.* **1997**, *9*, 1116–1125.
95. Sridhar, N.; Dunn, D. S.; Anderko, A. In *Environmentally Assisted Cracking: Predictive Methods for Risk Assessment and Evaluation of Materials, Equipment and Structures*; ASTM STP 1401; Kane, R. D., Ed.; American Society for Testing and Materials: West Conshohocken, PA, 2000; p 241.
96. Mohr, D. W.; McNeil, M. B. *J. Nucl. Mater.* **1992**, *190*, 329–342.
97. Macdonald, D. D. *Pure Appl. Chem.* **1999**, *71*, 951–978.
98. Vetter, K. J. *Electrochemical Kinetics*; Academic Press: New York, London, 1967.
99. Bockris, J. O'M.; Reddy, A. K. N. *Modern Electrochemistry*; Plenum Press: New York, 1970.
100. Kaesche, H. *Metallic Corrosion*; NACE International: Houston, TX, 1985.
101. Bockris, J. O'M.; Khan, S. U. M. *Surface Electrochemistry: A Molecular Level Approach*; Plenum Press: New York, London, 1993.
102. Gileadi, E. *Electrode Kinetics*; VCH Publishers: New York, 1993.
103. Kim, Y. J. *Corrosion* **2002**, *58*, 208–215.
104. Wagner, C.; Traud, W. Z. *Elektrochem* **1938**, *44*, 391–402.
105. Gileadi, E. Ed. *Electrosorption*; Plenum Press: New York, 1967.
106. Damaskin, B. B.; Petrii, O. A.; Batrakov, V. V. *Adsorption of Organic Compounds on Electrodes*; Plenum Press: New York, 1971.
107. Habib, M. A.; Bockris, J. O'M. In *Comprehensive Treatise of Electrochemistry*; Bockris, J. O'M., Conway, B. E., Yeager, E., Eds.; Plenum Press: New York, 1980; Vol. 1.
108. Anderko, A.; Young, R. D. *Corrosion* **2000**, *56*, 543–555.
109. Heusler, K. E.; Cartledge, G. E. *J. Electrochem. Soc.* **1961**, *108*, 732–740.
110. Lorenz, W.; Heusler, K. In *Corrosion Mechanisms*; Mansfeld, F., Ed.; Marcel Dekker: New York, 1987.
111. Drazic, D. M. In *Modern Aspects of Electrochemistry*; Conway, B. E., Bockris, J. O'M., White, R. E., Eds.; Plenum Press: New York, 1989; Vol. 19, pp 69–192.
112. Keddam, M. In *Corrosion Mechanisms in Theory and Practice*; Marcus, P., Oudar, J., Eds.; Marcel Dekker: New York, 1995.
113. Bockris, J. O'M.; Drazic, D.; Despic, A. R. *Electrochim. Acta* **1961**, *4*, 325–361.
114. Smart, N. G.; Bockris, J. O'M. *Corrosion* **1992**, *48*, 277–280.
115. Nešić, S.; Postlethwaite, J.; Olsen, S. *Corrosion* **1996**, *52*, 280–294.
116. Nordsveen, M.; Nešić, S.; Nyborg, R.; Stangeland, A. *Corrosion* **2003**, *59*, 443–456.
117. Chin, R. J.; Nobe, K. J. *Electrochem. Soc.* **1972**, *119*, 1457–1461.
118. Kuo, H. C.; Nobe, K. J. *Electrochem. Soc.* **1978**, *125*, 853–860.
119. Drazic, V. J.; Drazic, D. M. *J. Serb. Chem. Soc.* **1992**, *57*, 917–926.
120. Kear, G.; Barker, B. D.; Walsh, F. C. *Corros. Sci.* **2004**, *46*, 109–135.
121. Lee, H. P.; Nobe, K. J. *Electrochem. Soc.* **1986**, *133*, 2035–2043.
122. Deslouis, C.; Tribollet, B.; Mengoli, G.; Musiani, M. M. J. *Appl. Electrochem* **1988**, *18*, 374–383.
123. King, F.; Litke, C. D.; Quinn, M. J.; LeNeveu, D. M. *Corros. Sci.* **1995**, *37*, 833–851.
124. Smart, N. G.; Gamboa-Aldeco, M.; Bockris, J. O'M. *Corros. Sci.* **1993**, *34*, 759–777.
125. Jovancevic, V.; Bockris, J. O'M. *J. Electrochem. Soc.* **1986**, *133*, 1797–1807.
126. Zecevic, S.; Drazic, D.; Gojkovic, S. *Electrochim. Acta* **1991**, *36*, 5–14.
127. Jovancevic, V. In *Electrochemistry in Transition*; Murphy, O., Ed.; Plenum Press: New York, 1992; p 127.
128. Le Bozec, N.; Champere, C.; L'Her, M.; Laouenan, A.; Costa, D.; Marcus, P. *Corros. Sci.* **2001**, *43*, 765–786.
129. Kapusta, S. D. *Corrosion/2004*; NACE International: Houston, TX, 2004; Paper no. 04655.
130. King, F.; Quinn, M. J.; Litke, C. D. *J. Electroanal. Chem* **1995**, *385*, 45–55.
131. Sridhar, N.; Brossia, C. S.; Dunn, D. S.; Anderko, A. *Corrosion* **2004**, *60*, 915–936.
132. Calvo, E. J.; Schiffrin, D. J. *J. Electroanal. Chem* **1988**, *243*, 171–185.
133. Levich, V. G. *Physicochemical Hydrodynamics*; Prentice-Hall: Englewood Cliffs, NJ, 1962; p 700.
134. Poulson, B. *Corros. Sci.* **1983**, *23*, 391–430.
135. Poulson, B. *Corros. Sci.* **1993**, *35*, 655–665.
136. Eisenberg, M.; Tobias, C. W.; Wilke, C. R. *J. Electrochem. Soc.* **1954**, *101*, 306–319.
137. Berger, F. P.; Hau, K.-F. F. L. *Int. J. Heat Mass Trans.* **1977**, *20*, 1185–1194.
138. Lin, C. C.; Kim, Y.-J.; Niedrach, L. W.; Ramp, K. S. *Corrosion* **1996**, *52*, 618–625.
139. Wang, S.; Nešić, S. *Corrosion/2003*; NACE International: Houston, TX, 2003; Paper no. 03631.
140. Chilton, T. H.; Colburn, E. I. *Ind. Eng. Chem* **1934**, *26*, 1183–1187.
141. Frank, M. W. *Viscous Fluid Flow*, 2nd ed.; McGraw-Hill: New York, 1991.
142. Kim, D.; Sofya, Y.; Ghajar, A. J.; Dougherty, R. L. ASME Proceedings, National Heat Transfer Conference **1997**; Vol. 34, pp 119–130.
143. Adsani, E.; Shirazi, S. A.; Shadley, J. R.; Rybicki, E. R. *Corrosion/2002*; NACE International: Houston, TX, 2002; Paper no. 02492.
144. Adsani, E.; Shirazi, S. A.; Shadley, J. R.; Rybicki, E. R. *Corrosion/2006*; NACE International: Houston, TX, 2006; Paper no. 06573.
145. Corti, H.; Trevani, L.; Anderko, A. In *Aqueous Systems at Elevated Temperatures and Pressures; Physical Chemistry in Water, Steam and Hydrothermal Solutions*; Palmer, D. A., Fernandez-Prini, R., Harvey, A. H., Eds.; Academic Press, 2004; Chapter 10, p 752.
146. Anderko, A.; McKenzie, P.; Young, R. D. *Corrosion* **2001**, *57*, 202–213.
147. Ciaraldi, S. W.; Berry, M. R.; Johnson, J. M. *Corrosion/82*; NACE International: Houston, TX, 1982; Paper no. 98.
148. Pawel, S. J. *Corrosion* **1994**, *50*, 963–971.
149. Schmitt, G.; Losacker, S.; Renner, M. H. W.; Horn, E. M. *Corrosion/2004*; NACE International: Houston, TX, 2004; Paper no. 04229.
150. Newman, J.; Thomas-Alyea, K. E. *Electrochemical Systems*, 3rd ed.; Prentice Hall: Englewood Cliffs, NJ, 2004.
151. Davis, J. T. *Turbulence Phenomena*; Academic Press: London, 1972.

152. Lin, C. S.; Moulton, R. W.; Putnam, G. L. *Ind. Eng. Chem* **1953**, *45*, 636–640.
153. Walton, J. C. *Corros. Sci.* **1990**, *30*, 915–928.
154. Bear, J. *Dynamics of Fluids in Porous Media*; Dover Publications: New York, NY, 1972.
155. Nešić, S.; Lee, K.-L. *J. Corrosion* **2003**, *59*, 616–628.
156. Frankenthal, R. P.; Kruger, J. Eds. *Passivity of Metals*; The Electrochemical Society: Princeton, NJ, 1978.
157. Froment, M. Ed. *Passivity of Metals and Semiconductors*; Elsevier: Amsterdam, 1983.
158. Marcus, P.; Oudar, J. Eds. *Corrosion Mechanisms in Theory and Practice*; Marcel Dekker: New York, 1995.
159. Natishan, P. M. Ed. *Passivity and its Breakdown*; The Electrochemical Society: Princeton, NJ, 1998; Vol. PV97-26.
160. Macdonald, D. D. *J. Electrochem. Soc* **2006**, *15*, B213–B224.
161. Macdonald, D. D. *Corrosion* **1992**, *48*, 194–205.
162. Ebersbach, U.; Schwabe, K.; Ritter, K. *Electrochim. Acta* **1967**, *12*, 927–938.
163. Park, H. Y.; Tsuruta, T.; Macdonald, D. D. EPRI Project RP 1166-1 report Electric Power Research Institute: Palo Alto, CA, 1980.
164. Sridhar, N.; Brossia, C. S.; Dunn, D. S.; Buckingham, J. P.; Anderko, A. *Corrosion/2002*; NACE International: Houston, TX, 2002; Paper no. 2204.
165. Leckie, H. P. *Corrosion* **1968**, *24*, 70–74.
166. Blesa, M. A.; Morando, P. J.; Regazzoni, A. E. *Chemical Dissolution of Metal Oxides*; CRC Press: Boca Raton, FL, 1994.
167. Sridhar, N.; Wu, J. B. C.; Corey, S. M. *Mater. Perform.* **1987**, *26*(10), 17–23.
168. Sun, W.; Nešić, S. *Corrosion/2006*; NACE International: Houston, TX, 2006; Paper no. 06365.
169. Anderko, A.; Young, R. D. *Corrosion/99*; NACE International: Houston, TX, 1999; Paper no. 31.
170. Nešić, S.; Cai, J.; Lee, K.-L. *J. Corrosion/2005*; NACE International: Houston, TX, 2005; Paper no. 05556.
171. Sun, W.; Nešić, S. *Corrosion/2007*; NACE International: Houston, TX, 2007; Paper no. 07655.
172. Szklarska-Smialowska, Z. *Pitting and Crevice Corrosion*; NACE International: Houston, TX, 2005.
173. Heusler, K. E.; Fischer, L. *Werkst. Korros* **1976**, *27*, 551–556; *Werkst. Korros.* **27**, 788–791.
174. Strehblow, H. H.; Titze, B. *Corros. Sci.* **1977**, *17*, 461–472.
175. Lin, L. F.; Chao, C. Y.; Macdonald, D. D. *J. Electrochem. Soc* **1981**, *128*, 1194–1198.
176. Okada, T. *J. Electrochem. Soc* **1984**, *131*, 241–247.
177. McCafferty, E. J. *Electrochem. Soc* **1990**, *137*, 3731–3737.
178. Haruna, T.; Macdonald, D. D. *J. Electrochem. Soc* **1997**, *144*, 1574–1581.
179. Yang, S.; Macdonald, D. D. *Electrochim. Acta* **2007**, *52*, 1871–1879.
180. Milošev, I.; Metikoš-Huković, Drogowska, M.; Ménard, H.; Brossard, L. *J. Electrochem. Soc.* **1992**, *139*, 2409–2418.
181. Dunn, D. S.; Sridhar, N.; Cragnolino, G. A. *Corrosion* **1996**, *52*, 1583–1612.
182. Dunn, D. S.; Cragnolino, G. A.; Sridhar, N. *Corrosion* **1996**, *56*, 90–104.
183. Anderko, A.; Sridhar, N.; Dunn, D. S. *Corros. Sci.* **2004**, *46*, 1583–1612.
184. Okada, T. *J. Electrochem. Soc.* **1984**, *131*, 1026–1032.
185. Anderko, A.; Sridhar, N.; Brossia, C. S.; Dunn, D. S. *Corrosion/2004*; NACE International: Houston, TX, 2004; Paper no. 04061.
186. Anderko, A.; Sridhar, N.; Tormoen, G.; Brossia, C. S. *Corrosion/2006*; NACE International: Houston, TX, 2006; Paper no. 06215.
187. Dunn, D. S.; Pensado, O.; Pan, Y.-M.; Pabalan, R. T.; Yang, L.; He, X.; Chiang, K. T. Report CNWRA 2005-02 Southwest Research Institute: San Antonio, TX, 2005.
188. Anderko, A.; Sridhar, N.; Brossia, C. S. *Corrosion/2005*; NACE International: Houston, TX, 2005; Paper no. 05053.
189. Hibner, E. L. *Corrosion/86*; NACE International: Houston, TX, 1986; Paper no. 181.
190. Nešić, S.; Postlethwaite, J.; Vrhovac, M. *Corros. Rev* **1997**, *15*, 211–240.
191. Nyborg, R. *Corrosion/2002*; NACE International: Houston, TX, 2002; Paper no. 02233.
192. Papavinasam, S.; Revie, R. W.; Doiron, A. *Corrosion/2005*; NACE International: Houston, TX, 2005; Paper no. 05643.
193. Papavinasam, S.; Revie, R. W.; Doiron, A. *Corrosion/2005*; NACE International: Houston, TX, 2005; Paper no. 05644.
194. Papavinasam, S.; Revie, R. W.; Friesen, W. I.; Doiron, A.; Paneerselvam, T. *Corros. Rev.* **2006**, *24*, 173–230.
195. Dayalan, E.; de Moraes, F. D.; Shadley, J. R.; Shirazi, S. A.; Rybicki, E. F. *Corrosion/98*; NACE International: Houston, TX, 1998; Paper no. 51.
196. Pots, B. F. M.; Kapusta, S. D. *Corrosion/2005*; NACE International: Houston, TX, 2005; Paper no. 05550.
197. Deng, C.; Sand, K.; Teevens, P. J. *Corrosion/2006*; NACE International: Houston, TX, 2006; Paper no. 06565.
198. Nešić, S.; Nordsveen, M.; Nyborg, R.; Stangeland, A. *Corrosion* **2003**, *59*, 489–497.
199. Nešić, S.; Xiao, Y.; Pots, B. F. M. *Corrosion/2004*; NACE International: Houston, TX, 2004; Paper no. 04628.
200. Betts, A. J.; Boulton, L. H. *Br. Corros. J.* **1993**, *28*, 2121–2135.
201. Turnbull, A. *Corros. Sci.* **1993**, *34*, 921–960.
202. Turnbull, A. *Corros. Sci.* **1997**, *39*, 789–805.
203. Turnbull, A. *Corrosion* **2001**, *57*, 175–189.
204. Engelhardt, G.; Macdonald, D. D.; Millett, P. J. *Corros. Sci.* **1999**, *41*, 2165–2190.
205. Engelhardt, G.; Macdonald, D. D.; Urquidi-Macdonald, M. *Corros. Sci.* **1999**, *41*, 2267–2302.
206. Shoesmith, D. W.; Kolar, M.; King, F. *Corrosion* **2003**, *59*, 802–816.
207. Turnbull, A.; Ferris, D. H. *Corros. Sci.* **1987**, *27*, 1323–1350.
208. Turnbull, A. *Br. Corros. J.* **1993**, *28*, 297–308.
209. Engelhardt, G.; Urquidi-Macdonald, M.; Macdonald, D. D. *Corros. Sci.* **1997**, *39*, 419–441.
210. Engelhardt, G.; Urquidi-Macdonald, M.; Macdonald, D. D. *Corros. Sci.* **2004**, *46*, 1159–1187.
211. Cui, F.; Presuel-Moreno, F.; Kelly, R. G. *Corros. Sci.* **2005**, *47*, 2987–3005.
212. Sridhar, N.; Anderko, A. *Corrosion/2001*; NACE International: Houston, TX, 2001; Paper no. 1348.
213. Rahmani, M.; Strutt, J. E. *Hydrodynamic Modeling of Corrosion of Carbon Steels and Cast Irons in Sulfuric Acid*, Materials Technology Institute; NACE International: Houston, TX, 1992.
214. Veawab, A.; Aroonwilas, A. *Corros. Sci.* **2002**, *44*, 967–987.
215. Huet, B.; L'hostis, V.; Santarini, G.; Feron, D.; Idrissi, H. *Corros. Sci.* **2007**, *49*, 1918–1932.
216. Anderko, A.; Sridhar, N.; Yang, L. T.; Grise, S. L.; Saldanha, B. J.; Dorsey, M. H. *Corros. Eng. Sci. Technol* **2005**, *40*, 33–42.
217. Jakab, M. A.; Sridhar, N.; Anderko, A. *Corrosion/2007*; NACE International: Houston, TX, 2007; Paper no. 07243.